Tools for quantitative MR imaging and spectroscopy for the improvement of therapy evaluation in oncology

Quincy van Houtum

Colophon

Tools for quantitative MR imaging and spectroscopy to improve therapy evaluation in oncology
PhD Thesis, Utrecht University, the Netherlands

ISBN: 978-94-6375-950-2
Print: Ridderprint | www.ridderprint.nl;

Tools for quantitative MR imaging and spectroscopy for the improvement of therapy evaluation in oncology

Methodes voor kwantitatieve MR-beeldvorming en spectroscopie ter verbetering van therapie evaluatie in oncologie

(met een samenvatting in het Nederlands)

Proefschrift

ter verkrijging van de graad van doctor aan de Universiteit Utrecht op gezag van de rector magnificus, prof. dr. H.R.B.M Kummeling, ingevolge het besluit van het college voor promoties in het openbaar te verdedigen op maandag 6 juli 2020 des middags te 2.30 uur

door

Quincy van Houtum

geboren op 13 december 1988 te Tilburg

Promotoren: Prof. dr. D.W.J. Klomp
Prof. dr. P.R. Luijten

Copromotor: Dr. W.J.M. van der Kemp

Table of Contents

Chapter 1

General Introduction

General Introduction

Therapy assessment in oncology

In oncology the need for good therapy assessment is high. Patients often receive chemotherapy, radiotherapy or a combination of both which in turn is a burden for the patient, especially if the therapy is ineffective. Much time is lost before this ineffectiveness is measurable with today's clinical standards and minimizes the efficacy or even possible use of a different therapy strategy such as resection surgery or using other chemotherapeutics. In addition to a decrease of the patient's quality of life, curative care may also degrade to palliative care.

This need for improved monitoring is clearly present in the treatment of rectal carcinomas, liver metastasis and lung carcinomas as discrimination of non-responders and responders is difficult. General practice for locally advanced rectal carcinomas is neoadjuvant chemotherapy, often followed by total mesorectal excision (TEM) due to lack of sensitivity with conventional clinical MRI (3T and below) to determine if the patients have a clinical complete response (CCr) to therapy. However, histological examination of the resected specimens shows no residual tumor cells in almost 20% of all rectal carcinoma cases. This raises the question if the current strategy is the best choice. New strategies already include a so-called wait and see approach, monitoring the patient carefully after chemotherapy without excision of the rectum, improving quality of life for many patients [1–4]. In all three tumor cases mentioned both CT and MR images are analyzed by a radiologist who focuses on the morphological changes of the tumor e.g. the shape, homogeneity and more to evaluate therapy response. However, these changes are only visible after 2 months or more of chemoradiation therapy or immunotherapy. Earlier detection of non-response would allow the oncologist to change to a different treatment, increasing patient recovery chances and decreasing cost of expensive drugs used. Although physiological changes always precede morphological changes, the focus of the current clinical standard still depends highly on the latter. Therefore, monitoring tumor physiology to evaluate therapy efficacy is paramount to improve individual patient care. While tumor morphology can be monitored by magnetic resonance imaging (MRI), tumor physiology can be monitored by magnetic resonance spectroscopy (MRS).

MRI and MRS

MR imaging and spectroscopy are non-invasive techniques that use a powerful magnetic field to acquire images or molecular details from within the human body. Nuclei with a non-zero spin such as hydrogen (^{1}H) and phosphorus (^{31}P) act as magnetic dipoles e.g. small magnets and align with the main magnetic field (B_0), precessing around the direction of B_0. Inhomogeneities of the B_0 field of the MR system result in multiple image and spectral artefacts reducing image quality and are caused by anatomical motion such as breathing and the cardiac cycle, system instability and differences in magnetic susceptibility of the different tissues in the body [5,6]. Shimming improves B_0 homogeneity by applying an offset to the standard imaging gradient system or by using shim coils, counteracting the B_0 inhomogeneities[7]. The magnetic alignment (i.e. the magnetization) is in equilibrium and can be influenced by transferring energy via transmit (Tx) of radio frequency (RF) pulses at the frequency of precession i.e. the Larmor frequency of a specific nucleus, using RF coils. After the pulse, the precessing magnetization of the nuclei return to equilibrium creating a time-varying magnetic flux through the receiver (Rx) coil which induces a current, the MR signal. In combination with magnetic gradient systems the MR signal can be spatially encoded to allow mapping and converting the signal intensities to create an image. Furthermore, a nucleus is affected by the position in a molecule as it experiences different electron shielding from neighboring atoms. MR spectroscopy exploits this difference as it causes a small change of the nuclear resonance frequency, enabling detection of different molecules and even the different nuclei in a molecule. In addition, it allows for the quantification of concentrations, acidity of the environment and more. The acquired MRS signal is not shown as an image, but rather as a spectral representation of the signal with different signal peaks for the different species.

Additional discrimination between the nuclear species with MRS or different tissue contrasts in MRI can be achieved due to the difference in return rate of the perturbed magnetization back to equilibrium. It is altered by interactions of the nucleus with its surrounding spins and atomic neighborhood and can be characterized by the longitudinal relaxation time or rate (T_1) describing the speed at which the magnetization returns aligned to the main magnetic field. Along with T_1, a mechanism described by the transverse relaxation time constant (T_2) is present. On a macroscopic level the nuclei exchange energy causing both the longitudinal but also the transverse relaxation. Additionally, small differences in the main field strength present by susceptibility differences in the macroscopic environment cause dephasing (T_2') of the previously coherent nuclear spins. Both mechanisms are comprised by T_2^*, the observed transverse relaxation time. These properties allow images with contrasts based on differences in the longitudinal or transverse relaxation rates but also on the chemical shifts of the Larmor frequencies and more.

Therapy evaluation with MRS

Assessing therapy response of tumors requires a viable biomarker indicative for tumor tissue and effectiveness to therapy. Current understanding shows an altered choline metabolism, playing an important part in lipid metabolism, is suited for therapy evaluation as it can be monitored using ^{1}H MRS at clinical field strengths (≤3 tesla). The total choline content (tCho), containing multiple choline metabolites such as free choline, glycerophosphocholine and phosphocholine, is elevated compared to healthy tissue and a decrease of this concentration implies effective therapy [8–10]. In addition, phosphorus (^{31}P) MRS allows the acquisition of specific energy- and phospholipid- metabolites *in vivo* [11]. The cell energy metabolism can be assessed by monitoring inorganic phosphate (Pi), phosphocreatine (PCr) and adenosine triphosphate (ATP, with α-, ß- and γ- resonances). The ratios of these metabolites are already used as diagnostic biomarkers as alteration are indicative for systemic diseases such as diabetes [12–14]. ^{31}P MRS is also able to detect cell membrane precursors, the phosphomonoester (PME) and cell membrane degradation products, the phosphodiesters (PDE). In consonance with tCho as a biomarker in ^{1}H MRS, increase of the PME to PDE ratios suggest proliferation and is correlated with tumor tissue[15–18]. A decrease in this ratios during therapy is marker of therapy response and takes place well before morphological changes can be observed [11,19,20].

However, ^{1}H/^{31}P MRS at clinical field strengths requires large volumes to acquire significant signal-to-noise (SNR) for evaluation due to the low abundance of ^{31}P compared to ^{1}H and suffers from low spectral resolution. Metabolic ^{1}H signals can also be obscured by high abundant lipid and water signals creating overlapping peaks making it very difficult to identify and quantify metabolites. Studies already show clinical MRS lacks sensitivity for diagnostic use in addition to the long acquisition times not suited for the clinic[17,21].

7T MRI and MRS

Ultra-high field magnetic resonance imaging, 7 tesla and higher, has the potential to improve therapy evaluation in oncology. The increased magnetic field strength improves the signal to noise ratio (SNR) and contrast to noise ratio (CNR) of the MR signals and images compared to clinical MRI and MRS. It allows for image acquisition with a higher imaging resolution within a shorter time compared to clinical high-field MRI (3T), improving discrimination of the different tissue types spatially and by contrast. Moreover, the increased SNR and spectral resolution at 7T allows discrimination of individual PME metabolites namely phosphocholine (PC) and phosphoethanolamine (PE), but also individual PDE metabolites glycerophosphocholine (GPC) and glycerophosphoethanolamine (GPE). The ratios of the individual phospholipid metabolites (PC to GPC, PE to GPE) have also been correlated with tumor tissue and are already used *in vivo* as a biomarker for therapy

evaluation in research [22]. In addition to discrimination of extracellular and mitochondrial species of inorganic phosphate (Pi), it is also possible to measure the pH of tissue as the resonance frequency of Pi changes with the acidity of the environment [23,24].

Unfortunately, translation of 7T MR imaging to the clinic is still cumbersome due to multiple challenges at ultra-high field (≥7 tesla). As with clinical MRI, tissue boundaries and anatomical motion cause artefacts with increasing complexity at higher field strengths. It can result in signal loss and therefore decrease in SNR, frequency shifts, decreased spectral resolution due to line broadening and more. In addition, use of an array of ^{1}H dipole antennas is required to create homogenous transmit fields (B_1^+) as the RF wavelength is shorter (≤11cm) than the dimensions in the human body e.g. the tissue boundaries, causing destructive RF interferences [25–27].

However, the Larmor frequency of ^{31}P at 7T is almost identical to the frequency of ^{1}H at 3T, creating opportunities to use the well-established 3 tesla RF engineering for application in 7T ^{31}P MR spectroscopy. For instance, surface coils use high energetic adiabatic RF pulses to create a spatially homogenous flip angle and are limited to superficial applications due the specific absorption rate (SAR), a safety measure for the total RF energy deposition in the human body during acquisition. Advances in ^{1}H MRI at 3T already demonstrate that a birdcage coil gives a homogeneous B_1^+ field that allows for the use of block pulses to achieve a spatially homogenous flip angle, reducing the overall SAR and allowing for more RF pulses per unit of time with an additional increased homogeneity over a larger field of view [28,29]. To improve SNR over the larger volumes of interest the number of Rx coils increases together with the dimensionality of the data. Furthermore, with the larger field of view, the data sets also increase in size and are difficult to analyze with current software, especially with investigative hardware. This increase in complexity and changes in the size of the datasets requires the development of new processing tools.

Thesis Aim

The overall goal of this thesis is to demonstrate a variety of tools to improve therapy assessment in oncology using quantitative MR imaging and spectroscopy at ultra-high field.

Thesis Outline

Multiple tools to improve therapy assessment are presented in this thesis. It covers the quantification of MR parameters of different tissue types and metabolites *ex vivo* and *in vivo*, correction methods for inhomogeneities of the main magnetic field, hardware advances to allow fast metabolic imaging in the body and software tools to enable data analysis of these new data formats.

In **Chapter 2**, the changes of MR parameters in porcine rectal specimens are investigated during formaldehyde fixation as it influences the longitudinal and transverse relaxation times of tissue. Results were translated and used to design an imaging protocol for quantification of MR parameters in *ex vivo* specimen of rectal carcinoma patients without fixation effects, aiming to quantify a discriminative MR parameter for tumor tissue and improving the necessary future validation with pathology.

In **Chapter 3**, the use of local shim coil array at high field MRI to improve the B0 field homogeneity in larger volumes in the body than currently possible with the static scanner shim gradients is simulated. Simulations are performed using Biot-Savart law to investigate if small loops driven by a small current can increase the degrees of freedom in image-based shimming of the B_0 field.

In **Chapter 4**, the SAR limitation for metabolic imaging in 7T ^{31}P MRI are minimized using a whole-body birdcage coil. Fast 31P MR spectroscopic imaging in the liver is demonstrated. In addition, the feasibility of 31P MR multi-echo spectroscopic imaging is investigated *in vivo* in the gluteus maximus.

In **Chapter 5** a software tool for the analysis of the large and new ^{31}P MRSI data is presented. The additional receiver coils in combination with new data from prototype hardware is not easily analyzed in current available research tools. Therefore, a graphical user interface is developed in MATLAB.

In **Chapter 6**, the advances of chapter 3 and 4 are demonstrated in a clinical setting by ^{31}P spectroscopic imaging of four lung carcinoma patients. ^{31}P MRSI at 7T is investigated as a promising non-invasive method for monitoring personalized therapy response in lung tumors**.**

In **Chapter 7** the tools to improve therapy response monitoring and evaluation presented in this thesis are summarized and discussed.

References

1. Maas M, Beets-Tan RGH, Lambregts DMJ, Lammering G, Nelemans PJ, Engelen SME, van Dam RM, et al. Wait-and-see policy for clinical complete responders after chemoradiation for rectal cancer. *J Clin Oncol*. 2011;29(35):4633-4640. doi:10.1200/JCO.2011.37.7176
2. Sammour T, Price BA, Krause KJ, Chang GJ. Nonoperative Management or 'Watch and Wait' for Rectal Cancer with Complete Clinical Response After Neoadjuvant Chemoradiotherapy: A Critical Appraisal. *Ann Surg Oncol*. 2017;24(7):1904-1915. doi:10.1245/s10434-017-5841-3
3. Walker AS, Zwintscher NP, Johnson EK, Maykel JA, Stojadinovic A, Nissan A, Avital I, et al. Future Directions for Monitoring Treatment Response in Colorectal Cancer. *Journal of Cancer*. 2014;5(1):44-57. doi:10.7150/jca.7809
4. Sauer R, Becker H, Hohenberger W, Rödel C, Wittekind C, Fietkau R, Martus P, et al. Preoperative versus postoperative chemoradiotherapy for rectal cancer. *New England Journal of Medicine*. 2004;351(17):1731–1740.
5. Truong T-K, Chakeres DW, Beversdorf DQ, Scharre DW, Schmalbrock P. Effects of static and radiofrequency magnetic field inhomogeneity in ultra-high field magnetic resonance imaging. *Magnetic Resonance Imaging*. 2006;24(2):103-112. doi:10.1016/j.mri.2005.09.013
6. Juchem C, de Graaf RA. B0 magnetic field homogeneity and shimming for in vivo magnetic resonance spectroscopy. *Analytical Biochemistry*. 2017;529:17-29. doi:10.1016/j.ab.2016.06.003
7. Salomir R, Senneville BD de, Moonen CT. A fast calculation method for magnetic field inhomogeneity due to an arbitrary distribution of bulk susceptibility. *Concepts in Magnetic Resonance Part B: Magnetic Resonance Engineering*. 2003;19B(1):26-34. doi:10.1002/cmr.b.10083
8. Glunde K, Jie C, Bhujwalla ZM. Molecular Causes of the Aberrant Choline Phospholipid Metabolism in Breast Cancer. *Cancer Res*. 2004;64(12):4270-4276. doi:10.1158/0008-5472.CAN-03-3829
9. Shin HJ, Baek H-M, Cha JH, Kim HH. Evaluation of Breast Cancer Using Proton MR Spectroscopy: Total Choline Peak Integral and Signal-to-Noise Ratio as Prognostic Indicators. *American Journal of Roentgenology*. 2012;198(5):W488-W497. doi:10.2214/AJR.11.7292
10. Glunde K, Ackerstaff E, Mori N, Jacobs MA, Bhujwalla ZM. Choline Phospholipid Metabolism in Cancer: Consequences for Molecular Pharmaceutical Interventions. *Mol Pharmaceutics*. 2006;3(5):496-506. doi:10.1021/mp060067e
11. Semmler W, Gademann G, Bachert-Baumann P, Zabel HJ, Lorenz WJ, van Kaick G. Monitoring human tumor response to therapy by means of P-31 MR spectroscopy. *Radiology*. 1988;166(2):533-539. doi:10.1148/radiology.166.2.3336731
12. Hwang J-H, Choi CS. Use of in vivo magnetic resonance spectroscopy for studying metabolic diseases. *Exp Mol Med*. 2015;47(2):e139. doi:10.1038/emm.2014.101
13. Hwang J-H, Stein DT, Barzilai N, Cui M-H, Tonelli J, Kishore P, Hawkins M. Increased intrahepatic triglyceride is associated with peripheral insulin resistance: in vivo MR imaging and spectroscopy studies. *American Journal of Physiology-Endocrinology and Metabolism*. 2007;293(6):E1663-E1669. doi:10.1152/ajpendo.00590.2006
14. Rider OJ, Francis JM, Ali MK, Holloway C, Pegg T, Robson MD, Tyler D, et al. Effects of Catecholamine Stress on Diastolic Function and Myocardial Energetics in Obesity. *Circulation*. 2012;125(12):1511-1519. doi:10.1161/CIRCULATIONAHA.111.069518
15. Negendank W. Studies of human tumors by MRS: A review. *NMR in Biomedicine*. 1992;5(5):303-324. doi:10.1002/nbm.1940050518
16. Aboagye EO, Bhujwalla ZM. Malignant Transformation Alters Membrane Choline Phospholipid Metabolism of Human Mammary Epithelial Cells. :6.
17. Park JM, Park JH. Human in-vivo 31P MR Spectroscopy of Benign and Malignant Breast Tumors. *Korean J Radiol*. 2001;2(2):80-86. doi:10.3348/kjr.2001.2.2.80

18. Guinney J, Dienstmann R, Wang X, de Reyniès A, Schlicker A, Soneson C, Marisa L, et al. The consensus molecular subtypes of colorectal cancer. *Nat Med*. 2015;21(11):1350-1356. doi:10.1038/nm.3967
19. Steen RG. Response of Solid Tumors to Chemotherapy Monitored by in Vivo 31P Nuclear Magnetic Resonance Spectroscopy: A Review. *Cancer Res*. Agust 1989:12.
20. Ng TC, Grundfest S, Vijayakumar S, Baldwin NJ, Majors AW, Karalis I, Meaney TF, et al. Therapeutic response of breast carcinoma monitored by 31P MRS in situ. *Magnetic Resonance in Medicine*. 1989;10(1):125-134. doi:10.1002/mrm.1910100112
21. Bakermans AJ, Bazil JN, Nederveen AJ, Strijkers GJ, Boekholdt SM, Beard DA, Jeneson JAL. Human Cardiac 31P-MR Spectroscopy at 3 Tesla Cannot Detect Failing Myocardial Energy Homeostasis during Exercise. *Front Physiol*. 2017;8. doi:10.3389/fphys.2017.00939
22. Krikken E, van der Kemp WJM, van Diest PJ, van Dalen T, van Laarhoven HWM, Luijten PR, Klomp DWJ, et al. Early detection of changes in phospholipid metabolism during neoadjuvant chemotherapy in breast cancer patients using phosphorus magnetic resonance spectroscopy at 7T. *NMR Biomed*. 2019;32(6):e4086. doi:10.1002/nbm.4086
23. Hendriks AD, Kemp WJM van der, Luijten PR, Petridou N, Klomp DWJ. SNR optimized 31P functional MRS to detect mitochondrial and extracellular pH change during visual stimulation. *NMR in Biomedicine*. 0(0):e4137. doi:10.1002/nbm.4137
24. Kan HE, Klomp DWJ, Wong CS, Boer VO, Webb AG, Luijten PR, Jeneson JA. In vivo 31P MRS detection of an alkaline inorganic phosphate pool with short T1 in human resting skeletal muscle. *NMR in Biomedicine*. 2010;23(8):995-1000. doi:10.1002/nbm.1517
25. Bottomley PA, Griffiths JR. Handbook of Magnetic Resonance Spectroscopy In Vivo: MRS Theory, Practice and Applications | Wiley. Wiley.com. https://www.wiley.com/en-us/Handbook+of+Magnetic+Resonance+Spectroscopy+In+Vivo%3A+MRS+Theory%2C+Practice+and+Applications-p-9781118997666. Accessed October 22, 2019.
26. Raaijmakers AJE, Italiaander M, Voogt IJ, Luijten PR, Hoogduin JM, Klomp DWJ, van den Berg CAT. The fractionated dipole antenna: A new antenna for body imaging at 7 Tesla. *Magn Reson Med*. 2016;75(3):1366-1374. doi:10.1002/mrm.25596
27. Erturk MA, El-Sharkawy A-MM, Moore J, Bottomley PA. 7 Tesla MRI with a transmit/receive loopless antenna and B1-insensitive selective excitation. *Magn Reson Med*. 2014;72(1):220-226. doi:10.1002/mrm.24910
28. Vaughan JT, Adriany G, Snyder CJ, Tian J, Thiel T, Bolinger L, Liu H, et al. Efficient high-frequency body coil for high-field MRI. *Magnetic Resonance in Medicine*. 2004;52(4):851-859. doi:10.1002/mrm.20177
29. Löring J, van der Kemp WJM, Almujayyaz S, van Oorschot JWM, Luijten PR, Klomp DWJ. Whole-body radiofrequency coil for (31) P MRSI at 7 T. *NMR Biomed*. 2016;29(6):709-720. doi:10.1002/nbm.3517

Chapter 2

Quantifications of relaxation time changes during tissue-fixation and tumor biomarkers in ex vivo recta at 7T MRI.

Quincy van Houtum

Catalina (S.) Arteaga de Castro

Martijn Intven

Miangela (M.) Lacle

Sieske Hoendervangers

Alice (M.) Couwenberg

Helena (M.) Verkooijen

Dennis (W.J.) Klomp

Marielle (E.P.) Philippens

Keywords: MRI, Quantification, Relaxation, Fixation, Rectum, *ex vivo*

Abstract

Introduction: For restaging of rectal carcinoma after neoadjuvant therapy with ultrahigh field MRI, validation with high resolution *ex vivo* scans is required. As *ex vivo* MRI is challenging because tissue fixation and degradation alter tissue properties, we quantified changes in magnetization at ultrahigh field MRI during fixation using porcine recta. These results are used to investigate possible MR biomarkers for tumor discrimination in human rectal specimen that could be translated to *in vivo* imaging.

Methods: Relaxation time maps were acquired in five porcine and nine human recta specimens using a 7T MR system. To evaluate changes in relaxation times, serial measurements in porcine recta were done every 2 hours during fixation up to 16 hours. Changes in T_1, T_2 and T_2^* were quantified in the segmented circular muscle, mucosa and submucosa. The human recta were scanned within 3 hours of formaldehyde fixation and T_1 and T_2 relaxation times were quantified in tumor and healthy tissue.

Results: The largest change in tissue relaxation over time was found in the circular muscle with a T_2^* decrease of 0.7 ms/hr ($p<0.05$) and a T_1 decrease of 17 ms/hr. The mucosa and submucosa showed only a decrease in T_1 of 9 ms/hr ($p<0.05$) and 15 ms/hr ($p<0.05$) respectively. Changes in proton density of -0.6 %/hr and -0.5 %/hr for the circular muscle and mucosa, were observed. Based on the *ex vivo* porcine recta measurements showing a large decay in T_1 during the first few hours of fixation it was decided to quantify the T_1 and T_2 of human specimens within 3 hours of fixation. The T_1 and T_2 values of human specimens were 844±106 ms and 56±4.6ms for tumor tissue and 835±76ms and 52±7.9ms for the healthy tissue including mainly the circular muscle.

Discussion: The fixation of *ex vivo* rectal tissue reduced T_1 relaxation times of the circular muscle, mucosa and submucosa and reduced T_2^* relaxation times of the circular muscle over time. Dehydration caused by the fixation was also observed as a decrease in proton density. These findings directed the tissue characterization of human rectal specimens by imaging within a few hours of fixation to minimize fixation influences in T_1 and excluding T_2^* quantification. The human specimens showed no difference in T_1 or T_2 between tumor and healthy tissue. However, the latter could be caused by the high tumor inhomogeneity in the human specimens.

Abbreviations: clinical complete responders **(cCR)**, neoadjuvant chemoradiation **(CRT)**, pathological complete response **(pCR)**, total mesorectal excision **(TME)**, signal-to-noise ratio **(SNR)**, region of interest **(ROI)**, field of view **(FOV)**, gradient echo **(GE)**, number of sampled averages **(NSA)**, repetition time **(TR)**, echo time **(TE),** spoiled gradient recalled echo **(SPGR)**, inversion recovery **(IR)**, turbo spin-echo **(TSE)**, multi-echo **(ME)**.

Introduction

More than 14000 people in the Netherlands were diagnosed with colorectal cancer in 2018, making it the third and fourth largest cause of cancer morbidity and mortality, respectively[1–3]. In almost a third of patients the primary tumour is situated in the rectum. For locally advanced rectal cancer the standard of care is neoadjuvant chemoradiation (CRT) followed by total mesorectal excision (TME) surgery. Approximately 15-20% of the patients after CRT and TME show no residual tumour cells in the resection specimen; a pathological complete response (pCR). These statistics question the additional value of TME surgery in these patients. For this reason, organ preserving strategies in clinical complete responders after neoadjuvant therapy are currently being explored, such as the watch-and-wait strategy[4–7].

Currently, MRI is the most important clinical diagnostic tool to define the regression status of the patient. As the clinical accuracy in the detection of residual tumour cells is low, selection of patients remains challenging in the discrimination of clinical responders (cCR) from pathological complete responders and non-pathological complete responders[5,6]. The lack of proper biomarkers for detection of residual tumour cells may be overcome with the use of ultra-high field MRI as the differences in tissue relaxation properties between different tissue types (normal vs tumor) increase. Therefore, image contrast is enhanced and can be used for tissue differentiation. In addition, ultra-high field MRI allows for higher imaging resolutions at shorter scanning time with sufficient signal to noise ratio (SNR), when compared to lower magnetic field strengths. The increased spatial resolution can be exploited to differentiate between residual tumour and fibrotic tissue and find small tumour residues.

To investigate if ultra-high field MRI improves the distinction of pCR from non-pCR, validation of imaging with pathology is mandatory. As an intermediate step for the validation of *in vivo* imaging, resected specimens can be imaged and used for validation with pathology. *Ex vivo* MRI, however, presents a challenge compared to *in vivo* imaging as the tissue image contrast is affected by tissue alterations, due to fixation, tissue degradation and the loss of blood flow. Degradation of the tissue will increase all relaxation times as the integrity of structures are lost, and fluids are released. This can be counteracted with immediate formaldehyde fixation after resection for up to 20 hours to inhibit tissue degradation. During the fixation process, the tissue degradation effects are stopped, the formaldehyde reacts with peptides and lipids creating large cross-linked molecular complexes, retaining initial tissue state but changing the chemical environment[8,9]. This effect inherently alters the MR properties of the tissue as it reaches a more dehydrated and rigid state and it is expected to show decreased longitudinal and transverse relaxation times. To

translate MR contrast from the *ex vivo* to the *in vivo* situation, care must be taken to incorporate these contrast alterations as the relaxation times are not identical to the *in vivo* situation. Furthermore, optimization of high-resolution imaging protocols requires knowledge of tissue relaxation times.

To closely study the effects of fixation on MR contrast we therefore quantified the changes in relaxation time during fixation of *ex vivo* recta at ultrahigh field MRI, using porcine recta as a model for human recta[10]. In addition, the transverse and longitudinal relaxation parameters of non-tumorous and tumour tissue in *ex vivo* human recta were quantified based on the knowledge obtained from the *ex vivo* animal recta. This might be used to investigate possible MR tumor biomarkers that could be translated to *in vivo* imaging.

Material & Methods

Animals

Between June and October 2015, five rectal specimens from pigs (Vion Food Group NV, Boxtel, Netherlands) were collected from animals, which were sacrificed for the food processing industry and not for the purpose of this study, within 15 minutes after termination by CO_2 and an electric shock. The rectal specimens were transported in a thermally isolated cooler with plastic ice packs to cool the specimens and maintain the temperature below 7˚C, slowing down the degradation process of the tissue. After transport, the rectal specimens were immediately cleaned from faeces by thoroughly flushing them with tap water. Redundant fat lobes were resected. The specimens were then refrigerated (4-7 °C) until fixation prior to the scan session. After positioning inside a closable PVC tube, each rectal specimen was submerged in a neutral buffered 4% formaldehyde solution. To ensure full fixation of the porcine tissue without compromising the integrity of the tissue and its shape, the rectal lumen was filled with formaldehyde using a syringe, retaining the tubular shape of the specimen.

Patients

Nine rectal specimens collected from rectal cancer patients who underwent rectal resection after neoadjuvant therapy were scanned to characterize the tissue properties for biomarker evaluation and protocol optimization. Each specimen was thoroughly rinsed with water by the pathologist prior to fixation to clean it from faeces and residual blood. No fat lobes were removed nor was any incision made. The specimens were then inserted in a closeable PVC tube identical to the porcine recta experiments and filled with a neutral buffered 4% formaldehyde ensuring that no air pockets were left inside the specimen. The fixation process was immediately performed after surgery. The time between surgery and the scanning varied between specimens with a maximum delay of 6 hours.

High Resolution MRI

A 32-channel high density receive coil array-pad with a surface area of 34 x 14 cm^2 (MR Coils, Netherlands, Zaltbommel) was wrapped around the tube with the specimen and positioned at the centre of a dual-transmit head coil (NOVA Medical Inc., United States of America, Wilmington MA) which was placed at the isocenter of a 7T MRI system (Philips Healthcare, Best). The combination of both the coil and the ultrahigh field MR system allowed for imaging at high spatial resolution.

Sequence Details

Images of the recta for localization and planning of image-based B_0 shimming were obtained using a T_1-weighted 3D gradient echo sequence (GE). Aside from 3rd and 2nd order image based B_0 shimming of the main magnetic field for the porcine and human experiments respectively, other preparation phases were identical throughout all experiments. B_1 calibration was acquired to adjust the B_1 field for obtaining 100% of the nominal flip angle in the area of interest through manual RF power optimization.

For the porcine recta experiments quantitative T_2 and T_2^* maps were acquired using a multi-echo spin-echo (ME-SE) and a multi echo T_2^*-weighted gradient echo sequence (ME-GE) with 6 and 16 echoes respectively. T_1 changes were monitored using a spoiled gradient recalled echo (SPGR) protocol. All other imaging parameters for the porcine recta experiments are shown in table 1. In addition, dynamic field drifts due to the relatively long scan time were corrected by measuring and adjusting the scanner resonance frequency between each shot in SPGR sequences.

After the preparation phase of the human rectal specimens (same as for the pig recta), a high resolution T_2^*-weighted 3D GE sequence was used to acquire images for planning all other human rectal specimen related MR sequences and for delineation of regions of interest during processing. Quantitative T_1 and T_2 values were obtained in the patient specimens. The sequence used for T1 mapping in animal specimens were sensitive to small B1 changes. Therefore, we chose to use a 2D GE inversion recovery (IR) sequence with 20 IR times for the T_1 mapping on the human specimens. A 2D turbo spin-echo sequence (TSE) with 15 echoes was used for T_2 mapping. No T_2^* mapping was obtained as it was found to change relatively fast over time compared to other changes in the relaxation parameters in the porcine recta measurements. All other imaging parameters of the human rectal specimen experiments are shown in table 2.

Table 1. Overview of parameters used for all porcine specimen related MR sequences including the field of view (FOV), repetition time (TR), echo time (TE), the number of sampled averages (NSA) and acquisition time (Acq. Time). ([a], Two different repetition times were used to allow B_1 map calculations. [b], Two different flip angles for T_1 quantification were used during the T_1-weighted 3D-SPGR sequence. See discussion for further details. [c], Angle of the refocusing pulse in the spin echo sequence).

	B_0 –map	**B_1 - map**	**T_1-weighted**	**T_2 - map**	**T_2^* - map**
Technique	3D dual echo SPGR	3D Dual-TR GE	3D SPGR	2D T_2w multi echo SE	3D T_2^*w GE
FOV (mm^3)	210 x 115 x 100	100 x 100 x 100	100 x 100 x 20	80 x 80 x 0.5	100 x 100 x 20
Resolution (mm^2)	3.00 x 3.00 x 5.00	1.00 x 2.00 x 3.00	0.35-0.50 x 0.35-0.50 x 0.5	0.50 x 0.50	0.50 x 0.50 x 0.5
Slice thickness (mm)	-	-	-	0.5	-
Nr. of Slices	20	33	40	1	40
Flip angle	10°	50°	6° | 32° [b]	90° | 180° [c]	10°
TR (ms)	3.90	40.0 | 200 [a]	16.0	2500	119
TE (ms) | NxΔTE (ms)	1.63 | 1.00	1.52 | -	2.10 | -	10 | 6×10ms	2 | 16×2ms
turbo factor	-	-	160 - 250	-	-
SENSE	-	1	1	1	1
NSA	2	1	2	2	1
Acq. time (min:sec)	0:12	5:00	32:00	13:20	8:03

Table 2. Overview of parameters used for all human specimen related MR sequences including the field of view (FOV), repetition time (TR), echo time (TE), the number of sampled averages (NSA) and acquisition time (Acq. Time). The repetition interval and inversion recovery time are denoted separately for the T_1-maps protocol with α and β respectively.

	T_1-weighted	**T_2^*-weighted**	**T_1-maps**	**T_2 - map**
Technique	3D SPGR	3D GE	2D GE IR	2D TSE
FOV (mm^3)	450 x 146 x 300	80 x 80 x 50	100 x 80 x 0.5	90 x 80 x 0.5
Resolution (mm^2)	3.00 x 3.00 x 3.00	0.30 x 0.30 x 0.30	0.35-0.50 x 0.35-0.50	0.50 x 0.50
Slice thickness (mm)	-	-	0.5	0.5
Nr. of Slices	100	833	1	1
Flip angle	15°	30°	5°	90° | 180°
TR (ms)	14	16.0	50	1465
TE (ms) | NxΔTE (ms)	1.9 | -	10.0 | -	8 | 200^{α} | 20x15.4$^{\beta}$	6.1 | 15×6.1ms
turbo factor	-	-		15
SENSE	1	1	1	1
NSA				2
Acq. time (min:sec)	3:30			

α) Interval β) Inversion recovery time. 50 acquisitions every 10s

Sequence Timing

Firstly, for the porcine specimens, MRI scans were obtained once, prior to fixation, with the specimen emerged in Galden D05 (Solvey Plastics, Netherlands, Klundert), a perfluoropolyether fluorinated fluid without hydrogen protons, to minimize B_0 distortions. Immediately after submerging the recta in formaldehyde, the full imaging protocol, excluding the B_0 and B_1 map, was repeated every two hours. Additionally, the time since start of fixation was recorded. The human recta were also submerged in formaldehyde and imaged within 3 hours after start of fixation.

Processing

Images were processed using MATLAB 2014b (Mathworks, United States, Natick, MA). For T_2^* and T_1 calculations of the porcine recta, regions of interest (ROI) were drawn on the high resolution T_2^*-maps as these images showed the highest contrast between different tissue types. The circular muscle, submucosa and mucosa were distinguished and delineated. The same tissues were delineated separately in the T_2 maps. All delineations were guided by B_1 maps to exclude regions with an effective flip angle deviating more than ±25%. For all relaxation maps of the human rectal specimens two ROI were made using the high resolution T_2^*-weighted images: one within the tumour and the second within healthy tissue which included the circular muscle, submucosa and mucosa, reflecting the *in vivo* case with a lower resolution.

$$\log(SI) = -\frac{1}{T_2} * TE + log(S0) \qquad [1]$$

To decrease noise contributions for both T_2^* and T_2 measurements of the porcine recta and T_2 measurements of the human recta, the signal intensity within a ROI was averaged for all echoes in the echo train before solving the linearized equation 1 with SI the signal intensity of each echo, T_2 corresponding either to T_2 or T_2^* relaxation times, TE the echo time and S0 the signal at the start of acquisition. T_2 of the human recta were also calculated voxel wise and using signal averaging in a ROI using equation 1. T_1 was calculated by magnitude reconstruction using the signal in a ROI and applying an inversion to all signal acquired before the zero crossing using equation 2 with SI the signal intensity of each inversion time, M_0 the initial magnetization, TR the repetition time and TI the inversion time.

$$SI = \mathrm{M}_0 \left(1 - e^{\frac{(TR-TI)}{T1}}\right) \qquad [2]$$

For both transverse relaxation parameters, a linear trend line in the time series was fitted for each tissue type. The measured change in T_2 and T_2^* over time was tested by calculating the 95% confidence interval for the slope and conducting a two-tailed one-sample t-test with a significance level, α of 0.05.

As we used the signal change in the SPGR as a measure for change in proton density (small flip angle) and T_1 (larger flip angle), the SPGR signal intensity was simulated to investigate the linearity of the signal with respect to T_1 using equation 3. A TR of 16 ms, an expected T_1 range of [900 - 1500] ms and both the low and high flip angle of 6° and 32° were used with M, the longitudinal magnetisation at equilibrium set to 1. T_2^* effects were not taken into account given the short TE chosen. To test linearity of signal intensity with respect to T_1, the coefficient of determination, R^2 was calculated for a linear fit to the simulated signal intensities.

$$S = \frac{M\left(1-\exp\left(-\frac{TR}{T_1}\right)\right)\sin\alpha}{1-\exp\left(-\frac{TR}{T_1}\right)\cos\alpha} \qquad [3]$$

The measured T_1 changes in the rectal specimen were expressed as the change in signal intensity over time normalised to the signal intensity of the first scan since fixation. Relative pixel intensities inside the ROI for each tissue type were averaged per slice. To properly visualize T_1 changes of every porcine recta its time series as time of fixation between all specimens varied, the measured time points of each series were aligned with the time point closest to the start of fixation, disregarding small differences in the time intervals. Signal change for each delineated tissue type in both the high and low flip angle series was tested calculating the 95% confidence interval (CI) for the slope and performing a two-tailed one-sample t-test with a significance level, α of 0.05. Changes in the low flip angle series were considered as changes in proton density while changes in the large flip angle series were considered as a combination of T_1 and PD changes. To separate both effects, all slopes of the high flip angle series were corrected by adding the slope of the low flip angle series to eliminate the effect of changes in proton density during fixation. This approach decreases the contribution of flip angle inhomogeneities in the calculated T_1, compared to absolute T_1 measurements when using SPGR sequences as in the DESPOT1 method[11,12].

Results

Porcine specimen

Histological slices and the macroscopic image (fig. 1) created after fixation showed no compromised tissue structures and microscopic assessment agreed with these results. Using the 32-channel receiver array coil at 7T, images could be obtained that allowed mapping of relaxation times at high spatial resolution (fig. 2 and 3). Due to B_1 inhomogenities three porcine data sets were unsuited for quantification of T_2 in the mucosa and two porcine data sets for measuring T_2 in the circular muscle. ROI analyses of the relaxation parameters in the porcine recta only showed a significant T_2^* reduction ($p < 0.001$) in the circular muscle of 0.7 ms/hr, 95% CI [1, 0.5].

Consequently, the clear signal intensity difference between circular muscle and mucosa at the start of fixation due to the longer T_2^* was reduced on the last scans. For T_2, only a rapid change was observed in the submucosa from pre-fixation to fixation whilst for the remaining tissues T_2 remained constant pre- and during-fixation without any significant change ($p > 0.05$).

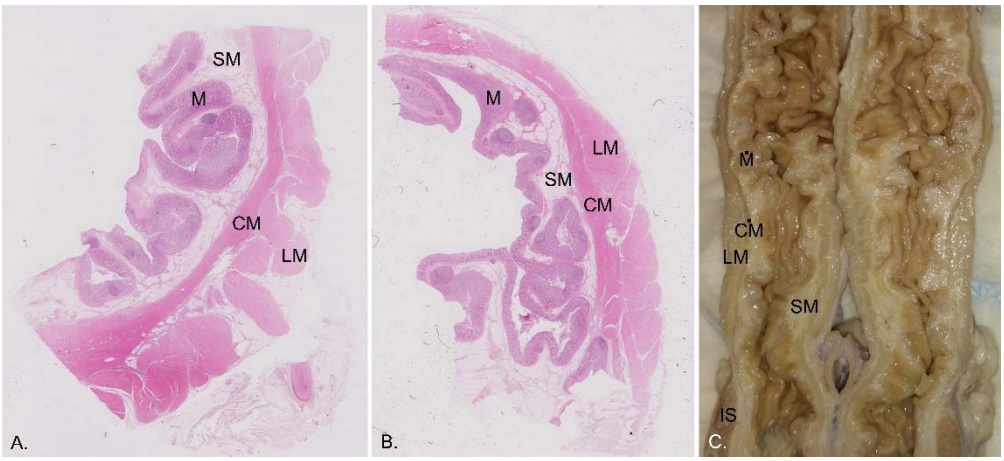

Figure 1. (**A**. and **B**.) Histology of a fixated porcine rectum with labels for multiple tissues, namely the mucosa (M), submucosa (SM), circular muscle (CM) and longitudinal muscle (LM). (**C**.) Macroscopic photo of a longitudinally cut fixated porcine rectum with the same annotated tissue structures as in figure A and B.

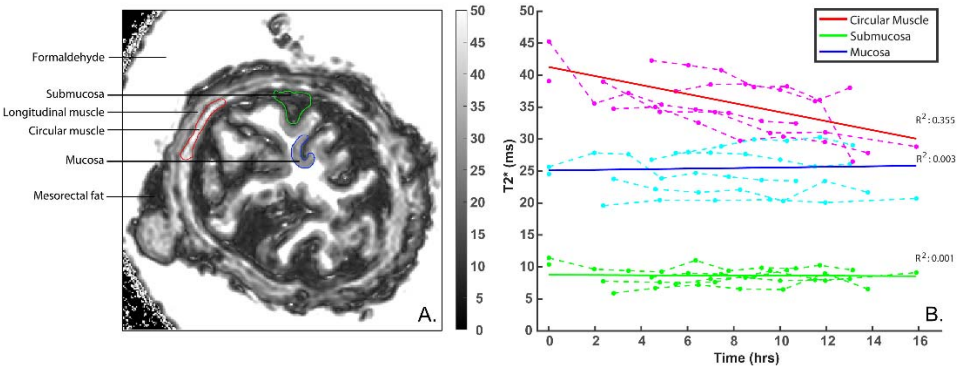

Figure 2. (**A.**) T_2^*-map of an imaged pig rectum in formaldehyde with anatomical labelling. The circular muscle, the submucosa and the mucosa are delineated in red, green and blue respectively. (**B.**) The T_2^* over time for three different tissue regions of interest as delineated in A.

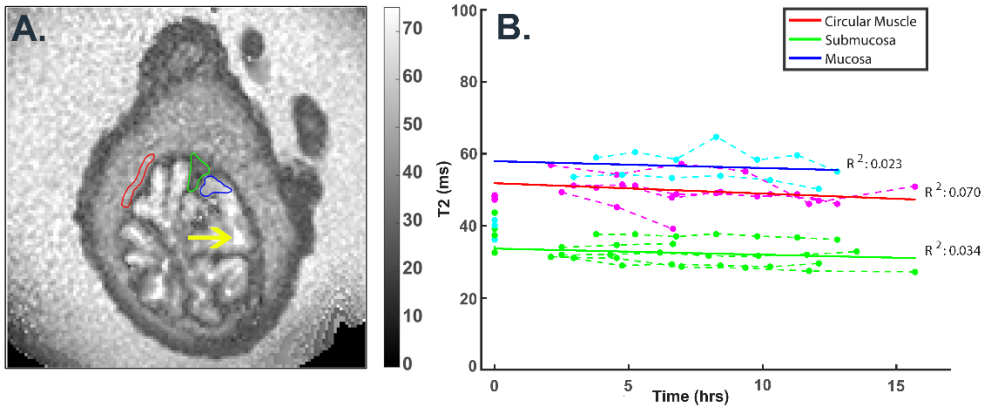

Figure 3. (**A.**) T_2-map of an imaged pig rectum in formaldehyde. The circular muscle, the submucosa and the mucosa are delineated in red, green and blue respectively. The hyper-intense signal from formaldehyde is denoted by the yellow arrow (**B.**) The T_2 over time for three different tissue regions as delineated in A.

The results of the SPGR simulations are shown in figure 4 to visualize the linearity of the signal intensity within the expected T_1 range for both flip angles including the ±25% margin. This holds for both the high and low flip angle though the latter shows a higher R^2 value. The absolute change in T_1 calculated from the percentage signal decrease were -9.2ms per percent signal change and -24.9ms per percent signal change for the high and low flip angle results, respectively. As the low flip angle method is not very sensitive for changes in T_1, we assumed that mostly reduction of protons was measured.

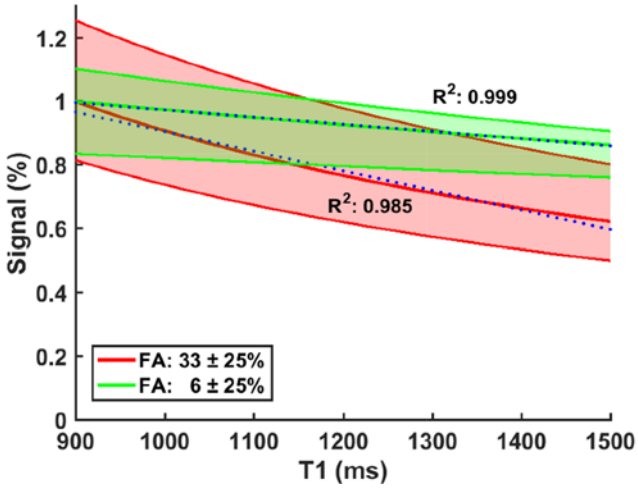

Figure 4. Simulated SPGR signal intensity over a range of T_1 relaxation times using equation 1. Simulations were performed with a TR of 16 ms, low and high flip angles of 6° (green) and 32° (red) respectively within a T_1 range of 900 - 1500 ms. A linear fit was performed and the coefficient of determination, denoted per flip angle, is used as a measure for linearity.

The analysis of the SPGR data of the porcine specimens shown in figure 5 demonstrate that the low flip angle series (fig 4.A-C) show a significant decrease of the normalized signal intensity in the circular muscle of 0.6%/hr ($p < 0.001$) with a 95% CI of [0.7, 0.5] and in the mucosa of 0.5%/hr ($p < 0.001$) with a 95% CI of [0.7, 0.3]. The change measured in the submucosa, 0.7% per hour with a 95% CI of [1.2, 0.1], was not significant ($p=0.058$).

The high flip angle series (fig. 5.D-E) before correcting for proton density weighting, resulted in a significant increase rate of 1.3%, 0.5% and 1% normalized signal intensity per hour in the circular muscle ($p < 0.001$), mucosa ($p < 0.025$) and submucosa ($p<0.025$) respectively. Correcting for changes in proton-density yielded 1.9% per hour with 95% CI of [1.7, 2.1], 1.0% per hour with 95% CI of [0.9 1.1] and 1.7% per hour with 95% CI of [1.6, 1.7] for the circular muscle, mucosa and submucosa respectively. Using the inversed regression coefficient of the simulated high flip angle SPGR signal, -9.2ms per percent signal, we were able to determine the absolute T_1 changes, namely; -17ms/hr in the circular muscle with a 95% CI of [-19, -16], -9ms/hr in the mucosa with a 95% CI of [-10 -8] and -15ms/hr in the submucosa with a 95% CI of [-26, -16].

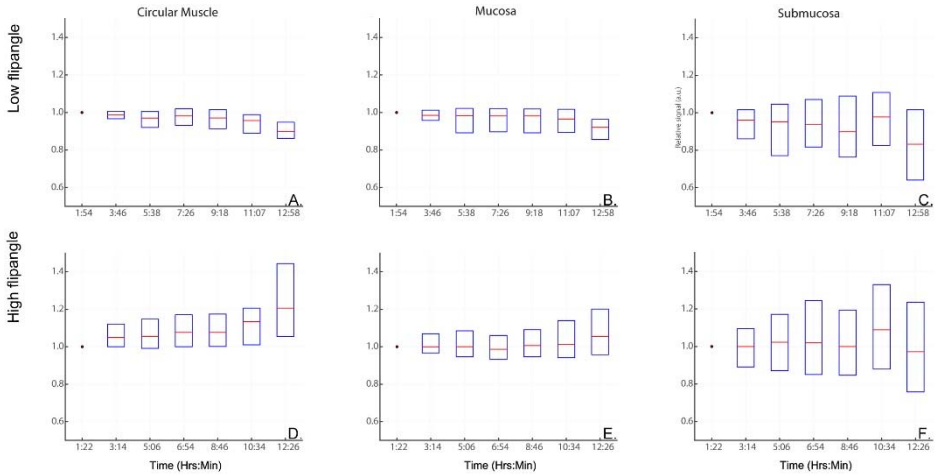

Figure 5. (**A-F.**) Normalized signal intensities over time in the circular muscle, mucosa and submucosa using a low, 6° and high, 33° flip angle showing the first and third quartile and the median (red line) of the delineated regions in all slices. The signal is relative to the first scan in its time-series, denoted by the red dot. Time for each series was aligned with the time-series which was closest to the start of fixation for both the low and high flip angle sequences.

Human specimen

All patients were operated successfully, and each specimen was brought to pathology within 10-30 minutes after surgery. All specimens contained tumour that

was confirmed by the pathologist after manual inspection of the specimens. Every tumour location was successfully recorded with respect to its position in the specimen and the PVC tube. T_1 and T_2 mapping were possible in eight of the nine specimens as one specimen suffered from inhomogeneous B_1^+. Figure 6 shows examples of the different image contrasts and quantification maps obtained of the human *ex vivo* specimens. The table in figure 6 shows the mean T_1 and T_2 values found in tumorous and non-tumorous regions after signal averaging. Mean T_1 relaxation times were 844±106ms with 95% CI range of [776, 913] and 835±76ms with 95% CI range of [778, 892] for tumor containing and healthy human rectal tissue respectively. The variance of T_1 in non-tumorous ROI was similar to the variance calculated for the tumorous ROIs. T_2 values within the tumor and non-tumorous rectal tissue are shown in the table in figure 6E. Mean T_2 relaxation times were 56±5ms with 95% CI range of [52, –61] and 52±7.9ms with 95% CI of [48, 57] for the tumor and non-tumorous rectal tissue ROIs respectively.

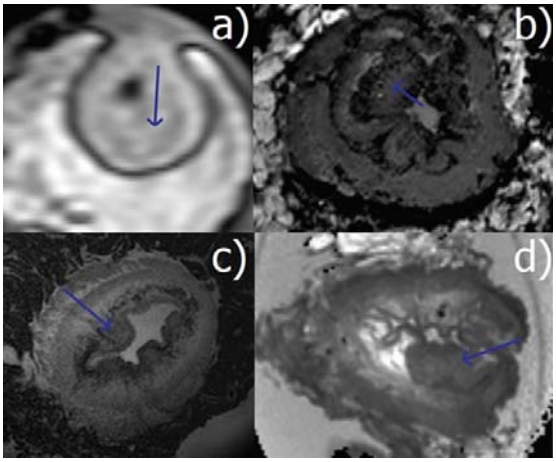

E)	T_1						T_2					
Patient#	Tumor	95% CI		Healthy	95% CI		Tumor	95% CI		Healthy	95% CI	
1	977	884	1069	909	838	980	48	47	50	43	42	44
2	897	841	953	847	800	893	59	57	62	57	56	58
3	760	722	798	858	813	902	54	51	57	50	39	51
4	810	724	893	835	750	919	65	60	71	54	48	61
5	995	920	1070	920	877	973	53	51	54	61	60	62
6	748	697	796	693	613	771	56	51	67	40	37	44
7	889	782	1010	882	853	921	55	41	69	64	44	84
8	678	642	714	733	677	779	57	56	58	57	55	60
Mean	844	776	913	835	778	892	56	52	61	52	48	57
St. Dev.	106	-	-	76	-	-	4.6	-	-	7.9	-	-

Figure 6. A). T_1-weighted MR image from the inversion recovery acquisition of a human *ex vivo* specimen. **B-D).** High resolution T_2-weighted MR images from the multi-echo TSE protocol of different human specimens. The blue arrows in figures A to D point to the tumor tissue of the rectal specimens. **E.)** Table with the calculated T_1 and T_2 values per patient specimen for tumor tissue and healthy rectal tissue. Abbreviations: Standard deviation (St. Dev.) Confidence interval (CI).

Discussion

Quantitative MRI with a high spatial resolution was feasible in *ex vivo* porcine and human rectal specimens. Mapping of T_2 and T_2^* relaxation times and the T_1-weighted signal change over time at different flip angles allowed us to quantify and visualize changes of MR tissue properties during tissue preservation by formaldehyde fixation in porcine recta. Combining the measured PD change with the SPGR simulations made it possible to convert the relative signal change over a period of 12 hours of 23% in the circular muscle, 20% in the submucosa and 12% in the mucosa, to absolute T_1 change. The overall largest changes were found in the circular muscle with a decrease in T_1 and T_2^* of 17 ms/hr and 0.7 ms/hr respectively. Less change was observed in the submucosa with a T_1 decrease of 15 ms/hr and the least change was seen in the mucosa with a T_1 decrease of 9 ms/hr. Moreover, a significant decrease in proton density in the circular muscle and mucosa of 7.2% and 6.0% per 12 hours, was found using the SPGR low flip angle series. The degradation process is inhibited as we expected a decrease of the relaxation times due to tissue alterations and dehydration. Changes in proton density however are less than changes in T_1 and T_2^*, thus tissue alterations caused by the fixative are thought to be the general cause of the decay.

Quantification of T_2^* is sensitive to susceptibility effects that are very prevalent in the rectum due to faeces, air and B_0 inhomogeneities, especially *in vivo*. The change of T_2^* over time still allows interpretation of fixation related changes however influences absolute T_2 measurements significantly. Therefore, only T_1 and T_2 constants in the human rectal specimen were quantified to favour future translation to the *in vivo* case. In addition, given that most tumors are mass-like and solid than the surrounding soft tissue, T_2 quantifications were thought to show the biggest difference in the human specimens. Quantification of relaxation time parameters in eight human rectal specimens showed no significant difference of T_2 relaxation times between tumorous and non-tumorous tissue with average T_2 of 56±4.6 and 52±7.9ms respectively. However, the tumor containing tissue did show slightly higher relaxation values. The T_2 relaxation values of the healthy tissue agree with our T_2 relaxation times found in porcine recta. No significant T_1 relaxation time differences between tumorous and healthy human rectal tissue was found with average T_1 of 844±106ms and 835±76ms respectively.

The high spatial resolution allowed by 7 T enabled delineation of multiple histological structural layers in the rectal wall of the porcine specimens. On the human specimens, we decided to include all tissues into one single ROI, to represent the *in vivo* case, given that such high spatial resolution is challenging to achieve *in vivo*. In addition, *in vivo* rectal imaging would present movement and artefacts coming from

passing air, air-tissue susceptibilities and peristaltic rectal motion. Therefore, delineation of three different rectal sublayers is challenging even if the same spatial resolution as in the *ex vivo* specimens could be achieved. Although the relaxation times of the circular muscle and the mucosa are similar after fixation, resulting in equal signal intensities and thus contrast loss, they are separated anatomically by the submucosa, still allowing proper delineation. The *in vivo* protocols will benefit from higher contrast with respect to the *ex vivo* images as blood circulation is present and no tissue degradation nor fixation effects occur, favouring future validation and contrast-based spatial correlation. Differentiation of the different tissues in the *ex vivo* situation by means of the tissue intrinsic relaxation properties, can be translated for tissue characterization *in vivo* in order to be used for the detection of residual tumor.

No changes in T_2 were observed during fixation for all three different tissues types, but the T_2 values measured in the mucosa prior to fixation did show a lower T_2 than in the fixated situation. This can be explained by partial volume effects. The mucosa pre-fixation is measured in Galden, which gives no signal on proton imaging, while formaldehyde has a long T_2 relaxation time as shown by the yellow arrow in figure 3. It was not an issue with the T_2^* protocol as sufficient SNR and contrast difference between mucosa and formaldehyde allowed for a more accurate delineation by excluding partial volume pixels and it includes multiple slices. However, the fixation process will lower T_2 relaxation times, as is concluded in multiple brain preservation studies, because the specimen solidifies[13–16]. Conversely, the transverse relaxation times are expected to increase during the first stage of tissue decomposition as autolysis damages cells and structures. Both processes, the T_2 increase due tissue degradation and T_2 decrease due to tissue fixation, occur simultaneously and could counteract each other, resulting in a stable T_2, as is seen in our results. Though not on-par with literature, we attributed this to the inherent penetration rate of the fixative in combination with the duration of the experiment. For example, Dawe et al. showed that a steep decline of T_2 values occurs in near surface tissue of the brain during the first day of fixation[16]. Similarly though, we found that the outer structure, the circular muscle, also showed the most decrease, all be it in T_1 and T_2^* and not T_2. Formaldehyde penetration is a non-linear and slow diffusion process of approximately 5mm per 8 hours, depending on tissue-type, strengthening the argument of experiment duration as an explanation for no change in T_2. Preservation with formaldehyde results in protein cross-linking and dehydration[8,9]. The decrease in PD can be interpreted as dehydration. This is apparent in all tissue layers which, in addition to the histological images, which confirms that the fixation process of the full rectal wall was guaranteed by submersion in formaldehyde and filling of the rectal lumen with formaldehyde after 12 hours. The location of the submucosa may explain the insignificant PD change, as the tissue is enfolded by the circular muscle and

mucosa. This causes a delay in fixation compared to superficial tissue and it is possible that our measurements were too early to measure substantial PD change.

T_2 weighted MRI is the most important imaging modality for tumour staging and response monitoring in rectal cancer. Yamada et al. reported on fully fixated human recta imaged at 3T and quantified T_2 relaxation times for staging of human rectal carcinoma[17]. T_2 maps provided insight on mural invasion depths in the colorectal wall of human rectal specimens which allowed differentiation of fibrotic and tumoral tissue. The T_2 values of the circular muscle and submucosa agree with our measurements. However, they showed a higher T_2 value for the submucosa compared to our measurements, being 165ms versus 35ms for the porcine recta and 165ms versus 51ms for the human recta. This leads to a hyper-intense submucosa whilst our images clearly show a hypo-intense submucosa. Even though they imaged at lower field strength, this difference is substantial. Although the fixative they used had a higher concentration of 10% v/v formaldehyde where we used a 4% v/v formaldehyde solution, this cannot explain the difference in T_2. The best explanation arises from comparison of the submucosa composition in the HE stained histological slices. Healthy porcine recta were used to increase throughput and flexibility, because patient material is limited and irregularly available. Even though a high similarity in size and function between gastrointestinal anatomy of pigs and humans exists, the histological slices showed a major variety in submucosa composition mostly due to differences in connective-tissue and fatty components, which is more prevalent in human specimens[10]. Our histological slices clearly depict a homogenous submucosa and during ROI selection in the MR images of the pig recta, inhomogeneous areas were avoided. Fatty components were not included according to the study of Yamada et al. though it would explain the increase of the measured T_2 in a voxel as fatty tissue has a relatively high T_2 relaxation time compared to the other components. From literature, it has been observed that tumour tissues have longer T_2 relaxation times, which were also expected to be observed in this *ex vivo* study[18,19]. Moreover, the T_2 relaxation times measured in our experiments in human rectal specimen agree with the porcine recta measurements of the circular muscle. ROI selection of healthy tissue in the human recta did not differentiate between the three different rectal layers as the high spatial resolution in not readily feasible *in vivo*.

A challenge at 7T is B_1 inhomogeneity which currently is inevitable, even after optimization of the B_1 field. This causes imperfect excitation and refocussing resulting in a lower measured T_2. One way to overcome this would be with the use of adiabatic RF pulses, which require higher duty cycles and therefore longer TRs. These effects make measurements unfeasible within reasonable scan times. Future studies could benefit from an update of the setup equipment to help to overcome the B_1 inhomogeneity in a specific area of interest. Securing the rectum in the centre of

the tube by means of MR inert material blocks could lengthen the RF wave, increasing B_1 homogeneity. Another option is to employ new RF-pulse strategies such as SPINS and kT-points which also provide in more homogenous flip angles over a larger FOV, even at higher field strengths[20,21].

Nevertheless, the B_1 inhomogeneity was within the ±25% limits of the requested flip angle for most of the relaxation time quantifications. However, the variable flip angle method for T_1 relaxation time calculation is very sensitive for B_1 inhomogeneity. The DESPOT$_1$ technique holds only for small ranges of T_1 and deviation from the two set flip angles results in low T_1 accuracy. To overcome this, we looked at the relative signal change over time. To ensure that the relative signal change linearly correlated to changes in T_1 when using a fixed flip angle, signal intensities were simulated (fig. 4). These simulations show high linearity in the chosen T_1 range for both the high and low flip angle. It also confirmed that the low flip angle images are hardly affected by T_1-changes as only unrealistic large changes in T_1 influence the signal. This made it possible to separate change in proton-density which is linked to the water content and change in T_1 by analysing both the low and high flip angle images. However, the assumption may have caused a minor overestimation of the decrease in proton and T_1 without affecting the intended purpose of this study as we look at the overall change over time. Given the sensitivity of the DESPOT method to B_1 inhomogeneities, human *ex vivo* T_1 experiments were performed with a more robust T_1 method that also allowed to obtain T_1 relaxation maps.

The T_1 values here found for the human specimens were within the range of T_1 values found for tumor and non-tumorous soft tissues at 7T[18]. No significant difference in T_2 relaxation times was found between tumor and healthy human rectal tissue in the present study, which does not agree with discriminative value of T_2-weighted MR images reported in literature[19]. However, from images and histological examination, it is seen that tumor tissue is inhomogeneous which may cause our result. This makes proper evaluation of MR parameters at UHF of tumor tissue cumbersome. This can also be seen by the increased standard deviation of the tumor T_1 values compared to healthy T_1 values measured in the human specimens.

Conclusion

To conclude, the fixation of *ex vivo* rectal tissue will lower the T_1 relaxation times of the circular muscle, mucosa and submucosa and reduces the T_2^* relaxation times of only the circular muscle as seen in porcine ex vivo specimens. In addition, dehydration by the fixation was measured using proton-density weighted images in all tissue types. The decrease of relaxation times results in contrast loss between the circular muscle and mucosa, but both tissues are anatomically separated by the

submucosa, which guarantees tissue discrimination. However, T_2 relaxation times in human recta are not different between tumour and non-tumorous tissue and seem not suitable as biomarker for *in vivo* detection of residual tumour after chemoradiation. This work increased the understanding of *ex vivo* rectal tissue characteristics by quantifying the MR related effects of tissue fixation and allows optimization of high-resolution MR imaging of human recta both *in* and *ex vivo*.

Acknowledgements

This project was funded by the Dutch digestive diseases foundation, Maag Lever Darm stichting. We would like to thank Vion Food with special regards to J. van Eindhoven for supplying the porcine recta and J.J.M. Zwanenburg for imaging protocol support.

References

1. Colorectal cancer statistics | World Cancer Research Fund International. http://www.wcrf.org/int/cancer-facts-figures/data-specific-cancers/colorectal-cancer-statistics. Accessed February 27, 2017.
2. Key Statistics for Colorectal Cancer. https://www.cancer.org/cancer/colon-rectal-cancer/about/key-statistics.html. Accessed February 27, 2017.
3. Marmot M, Atinmo T, Byers T, Chen J, Hirohata T, Jackson A, James W, et al. Food, nutrition, physical activity, and the prevention of cancer: a global perspective. 2007.
4. Maas M, Beets-Tan RGH, Lambregts DMJ, Lammering G, Nelemans PJ, Engelen SME, van Dam RM, et al. Wait-and-see policy for clinical complete responders after chemoradiation for rectal cancer. *J Clin Oncol Off J Am Soc Clin Oncol*. 2011;29(35):4633-4640. doi:10.1200/JCO.2011.37.7176
5. Sammour T, Price BA, Krause KJ, Chang GJ. Nonoperative Management or "Watch and Wait" for Rectal Cancer with Complete Clinical Response After Neoadjuvant Chemoradiotherapy: A Critical Appraisal. *Ann Surg Oncol*. 2017;24(7):1904-1915. doi:10.1245/s10434-017-5841-3
6. Walker AS, Zwintscher NP, Johnson EK, Maykel JA, Stojadinovic A, Nissan A, Avital I, et al. Future Directions for Monitoring Treatment Response in Colorectal Cancer. *J Cancer*. 2014;5(1):44-57. doi:10.7150/jca.7809
7. Sauer R, Becker H, Hohenberger W, Rödel C, Wittekind C, Fietkau R, Martus P, et al. Preoperative versus postoperative chemoradiotherapy for rectal cancer. *N Engl J Med*. 2004;351(17):1731–1740.
8. Rolls G. Fixation and Fixatives (2) – Factors influencing chemical fixation, formaldehyde and glutaraldehyde. *Leica Biosyst*. March 2012. http://www.leicabiosystems.com/pathologyleaders/fixation-and-fixatives-2-factors-influencing-chemical-fixation-formaldehyde-and-glutaraldehyde/. Accessed December 12, 2016.
9. III.—THE RATE OF PENETRATION OF FIXATIVES - Medawar - 1941 - Journal of Microscopy - Wiley Online Library. http://onlinelibrary.wiley.com/doi/10.1111/j.1365-2818.1941.tb00884.x/abstract. Accessed February 27, 2017.
10. Mach N, Berri M, Esquerré D, Chevaleyre C, Lemonnier G, Billon Y, Lepage P, et al. Extensive Expression Differences along Porcine Small Intestine Evidenced by Transcriptome Sequencing. *PLOS ONE*. 2014;9(2):e88515. doi:10.1371/journal.pone.0088515
11. Deoni SCL, Rutt BK, Peters TM. Rapid combinedT1 andT2 mapping using gradient recalled acquisition in the steady state. *Magn Reson Med*. 2003;49(3):515-526. doi:10.1002/mrm.10407
12. Deoni SCL, Peters TM, Rutt BK. Determination of optimal angles for variable nutation proton magnetic spin-lattice, T1, and spin-spin, T2, relaxation times measurement. *Magn Reson Med*. 2004;51(1):194-199. doi:10.1002/mrm.10661
13. Birkl C, Langkammer C, Golob-Schwarzl N, Leoni M, Haybaeck J, Goessler W, Fazekas F, et al. Effects of formalin fixation and temperature on MR relaxation times in the human brain. *NMR Biomed*. 2016;29(4):458-465. doi:10.1002/nbm.3477
14. Yong-Hing CJ, Obenaus A, Stryker R, Tong K, Sarty GE. Magnetic resonance imaging and mathematical modeling of progressive formalin fixation of the human brain. *Magn Reson Med*. 2005;54(2):324-332. doi:10.1002/mrm.20578
15. Tovi M, Ericsson A. Measurements of T1 and T2 over time in formalin-fixed human whole-brain specimens. *Acta Radiol Stockh Swed 1987*. 1992;33(5):400-404.
16. Dawe RJ, Bennett DA, Schneider JA, Vasireddi SK, Arfanakis K. Postmortem MRI of human brain hemispheres: T2 relaxation times during formaldehyde fixation. *Magn Reson Med*. 2009;61(4):810-818. doi:10.1002/mrm.21909

17. Yamada I, Yoshino N, Hikishima K, Miyasaka N, Yamauchi S, Uetake H, Yasuno M, et al. Colorectal carcinoma: Ex vivo evaluation using 3-T high-spatial-resolution quantitative T2 mapping and its correlation with histopathologic findings. *Magn Reson Imaging*. doi:10.1016/j.mri.2016.12.028

18. Gambarota G, Veltien A, Laarhoven H van, Philippens M, Jonker A, Mook OR, Frederiks WM, et al. Measurements of T1 and T2 relaxation times of colon cancer metastases in rat liver at 7 T. *Magn Reson Mater Phys Biol Med*. 2004;17(3):281-287. doi:10.1007/s10334-004-0068-2

19. Damadian R. Tumor Detection by Nuclear Magnetic Resonance. *Science*. 1971;171(3976):1151-1153. doi:10.1126/science.171.3976.1151

20. Sun H, Fessler JA, Noll DC, Nielsen J-F. Joint design of excitation k-space trajectory and RF pulse for small-tip 3D tailored excitation in MRI. *IEEE Trans Med Imaging*. 2016;35(2):468-479. doi:10.1109/TMI.2015.2478880

21. Malik SJ, Keihaninejad S, Hammers A, Hajnal JV. Tailored excitation in 3D with spiral nonselective (SPINS) RF pulses. *Magn Reson Med*. 2012;67(5):1303-1315. doi:10.1002/mrm.23118

Chapter 3

B0 shimming simulations of the liver using a local array of shim coils in the presence of respiratory motion at 7 T

Lieke van den Wildenberg

Quincy van Houtum

Wybe (J.M.) van der Kemp

Catalina (S.) Arteaga de Castro

Alex Bhogal

Paul Chang

Sahar Nassirpour

Dennis (W.J.) Klomp

Keywords: Local array of shim coils, B_0 shimming, 7 Tesla MRI, Liver, simulations

Abstract

Ultra-high field MRI has the potential to become a clinically viable tool due to its higher intrinsic SNR and CNR compared to current clinical MR field strengths. However, one of the main technical challenges with increasing field strength is the static magnetic field inhomogeneity. This study investigates via simulations the potential of a local array of shim coils in B0 field shimming of the liver during different respiratory phases. Biot-Savart simulations were performed using *in vivo* B0 field maps of the liver as input. The maps were acquired in 5 volunteers during free breathing and throughout inspiratory and expiratory breath-holds on a 7 T whole-body MR system. Array configurations of shim coil loops that could be merged with RF receiver arrays were simulated to analyze field uniformity in the generated B0 maps. Simulations showed an improvement of 10±4.7% in free breathing, 41±6.7% inspiratory state and 24±12% in expiratory state using standard shimming hardware of the scanner in addition with the local array of shim coils compared to the standard first and second order shimming. Local shimming is important especially at higher magnetic field strengths because of the increased impact of differences in magnetic susceptibility between air/bone-tissue interfaces. As demonstrated by simulations, the spatial field distribution of a local array in combination with standard hardware shimming can compensate these distortions by 10 to 41% better than only using the traditional B0 shimming.

Abbreviations: Magnetic Resonance **(MR)**, Magnetic Resonance Imaging **(MRI)**, Computed Tomography **(CT)**, signal-to-noise ratio **(SNR)**, contrast-to-noise ratio **(CNR)**, Magnetic Resonance Spectroscopic **(MRS)**, Radio frequency **(RF)**, versus **(vs.)**, gradient echo **(GE)**, field of view **(FOV)**, repetition time **(TR)**, echo time **(TE)**.

Introduction

Magnetic resonance imaging (MRI) is increasingly being used as a diagnostic modality to inform on lesions in the liver that are detected by ultrasound imaging or computed tomography (CT). This is especially the case for staging and restaging in oncologic patients (1). Ultra-high field MRI (≥ 7 T) has the potential to become a clinically viable tool for diagnostics, treatment planning and monitoring due to higher intrinsic signal-to-noise ratio (SNR) and contrast-to-noise ratio (CNR) compared to lower magnetic field strengths. This increase in SNR and CNR allows for higher spatial resolution and higher sensitivity in image acquisition than conventional clinical MRI (3T and below), which enables the detection and monitoring of smaller lesions in greater detail or obtain more accurate metabolic information with MR spectroscopy.

One of the technical challenges with increasing magnetic field strengths is the static magnetic field (B_0) inhomogeneity. Variations in the B_0 field lead to local frequency offsets that can cause artefacts during MR imaging and MR spectroscopic (MRS) measurements (2). MRS is particularly sensitive to B_0 field variation both spatially and temporally (ΔB_0) because it directly effects spectral resolution (3). Temporal or dynamic B_0 field inhomogeneities are either caused by scanner instability (e.g. eddy currents and drift), anatomical motion related to breathing and cardiac pulsations, or temporal B_0 fluctuations in the MR system. The magnetic susceptibility property of tissues in the body defines the ratio between the magnetic field and the resulting magnetization. Differences in the magnetic susceptibility result also in local magnetic field inhomogeneities,

$$\vec{B}_{nuc} = \left(1 - \sigma - \frac{2}{3} \cdot \chi\right) \cdot \vec{B}_{mac}, \qquad [1]$$

where $\vec{B}_{nuc}$ is the magnetic field of the nucleus proportional to the macroscopic magnetic field ($\vec{B}_{mac}$), which depends on the shielding effect produced by the electric shell around the nucleus (σ) and on the magnetic susceptibility (χ) (4). Increasing the field strength leads to an increase in susceptibility and, therefore, in local field inhomogeneities. This is resulting in an increased variance in the spatial frequency pattern as shown in,

$$f(\vec{r}) = \gamma \cdot \left(B_0 + \Delta B_0(\vec{r})\right) \qquad [2]$$

with $f(\vec{r})$ the spatial frequency pattern, γ the gyromagnetic ratio, and $\Delta B_0(\vec{r})$ the spatial difference of B_0 (5). If not accounted for, these distortions in the B_0 field will reflect as artefacts, peak shifts, line broadening, ghosting, phase corruption, and signal loss (2). In MRS, higher ΔB_0 causes reduced signal and broader line widths which causes lower SNR and reduced spectral resolution. On the other hand,

artefacts may be mitigated by acquiring during breath hold or by using gated acquisition strategies (6).

There are several correction methods for addressing B_0 inhomogeneity in the liver to also mitigate the reduced SNR and spectral resolution. The standard hardware strategy involves the use of shim fields that are generated by gradient coils or dedicated shim coils located within the bore-liner of the scanner. Current offsets added to imaging gradients will generate linear fields while dedicated shim coils typically generate up to third order spherical harmonic terms (4,7). Typical research systems are equipped with second order shimming capabilities that can remove the lowest spatial order variations in the B_0 field in a region of interest (8). To reduce more of the spatial order variations, higher order spherical harmonics are needed (9). Time varying B_0 fluctuations originating from physiological motion are more challenging to compensate. Applying image based B_0 shimming, while monitoring breathing and/or respiratory triggering, can help reduce B_0 field variations, however, generally at the cost of increased scan time and often not available at the MR system.

Juchem et al. showed that in conjunction with static second order shimming, the addition of a local array of shim coils that can be steered externally can reduce the residual magnetic field inhomogeneities (10,11). In this way, the field homogeneity can be improved throughout the duration of the scan in the brain (10,11). From this we know that using a local array of shim coils will reduce the B_0 inhomogeneity, because significantly higher order spherical harmonics are needed to mitigate more localized B_0 offsets (12). The array of shim coils can generate a spatially varying magnetic field counteracting $\Delta B_0(\vec{r})$ (equation 2).

In this study, we investigate via simulations the potential of adding a local array of shim coils in addition with the standard hardware shimming method in the scanner to further reduce the variations in the B_0 field in the liver during different respiratory phases. Simulations are compared to the conventional second order shim method at 7 T.

Methods

Acquisition

A whole-body 7 T MR scanner with a multi-transmit RF system (Achieva, Philips Health Care, Cleveland, OH, USA) was used to acquire B_0 maps of the liver in five healthy volunteers, which are used in the B_0 shimming simulations. All volunteers signed informed consent prior to scanning, and the study was approved by the local medical ethics committee.

Eight transceiver fractionated dipole antennas with 16 additional receive loops (Tesla Dynamic Coils, Zaltbommel, The Netherlands) interfaced to 8 parallel 2 kW channels were positioned symmetrically around the abdomen (13). Radio frequency (RF) phase shimming was performed to maximize transmission efficiency and optimize B_1^+ field homogeneity in the liver. Volunteers were scanned in supine position at the iso-center of the MR scanner with the body array positioned around the liver. Dual-echo B_0 maps were acquired during free breathing as well as during inspiratory and expiratory breath-hold in five volunteers. Sequence parameters were as follows: GE, 386 × 410 × 180 mm^3 FOV, 6 × 6 × 6 mm^3 voxel size, FA = 4°, TR = 6 ms, TE = 1.413 ms, ΔTE = 1 ms, slice thickness = 6 mm, number of slices = 30, scan time = 24.1 s.

Simulation

3D B_0 shimming simulations were performed using 30 slices of the gradient dual-echo field maps of the five volunteers in the full organ. The full liver was segmented manually in the 3D B_0 maps obtained in the three different respiratory states using MATLAB (R2016, Natick, MA) prior to the simulations. The simulated local shim coil array consisted of 16 circular loops with a diameter of 5 cm determined by the mechanical dimensions of the transceiver array (13). Each loop consisted of 20 coil windings of enameled copper wire having a diameter of 0.56 mm. Two coils of the B_0 shim array were placed on each dipole antenna of the body array with a distance between the two coils of 14 cm measuring from the center of the shim coils and 2.5 cm to the surface of the body. The coils were arranged in 2 rows of 8 coils, similar to the RF receive loops, to closely surround the abdomen in the simulations. The schematic overview in Figure 1 represents the local array of shim coils in combination with the body arrays as used in the simulations. Depending on the size of the volunteer, the eight antennas and thus the pairs of shim coils are further or closer together.

The magnetic field that was generated by a constant electric current through the shim coil array in the simulation was calculated using Biot-Savart Law with software provided by MR Shim GmbH (Reutlingen, Germany):

$$d\vec{\boldsymbol{B}} = \frac{\mu_0}{4\pi} \frac{I\, d\vec{\boldsymbol{l}} \times \hat{\boldsymbol{r}}}{r^2} \qquad [3]$$

where $d\vec{\boldsymbol{B}}$ is the magnetic field due to an infinitesimal current element, μ_0 the magnetic constant, *I* the current, $d\vec{\boldsymbol{l}}$ vector length of the element, $\hat{\boldsymbol{r}}$ the unit vector from element towards where the field is measured, and r the distance from the element to where the field is measured (14). The optimal current for each shim coil was calculated to minimize the least-squares deviation of the total field (ΔB_0 (x, y, z)

+ shim coil created field) in the full liver region. This calculation was done for each simulation with

$$A \cdot x = B \qquad [4]$$

where A is a matrix of vectorization of the B_0 field images for each of the shim channels for the given mask, x is a vector representing the optimized currents, and B is the B_0 field in the direction of the main 7 T field that the shim coils generate. The B_x and B_y components of the field are neglected. To calculate the optimized currents, the residual field will be minimized using the B field as the negative measured B_0 field.

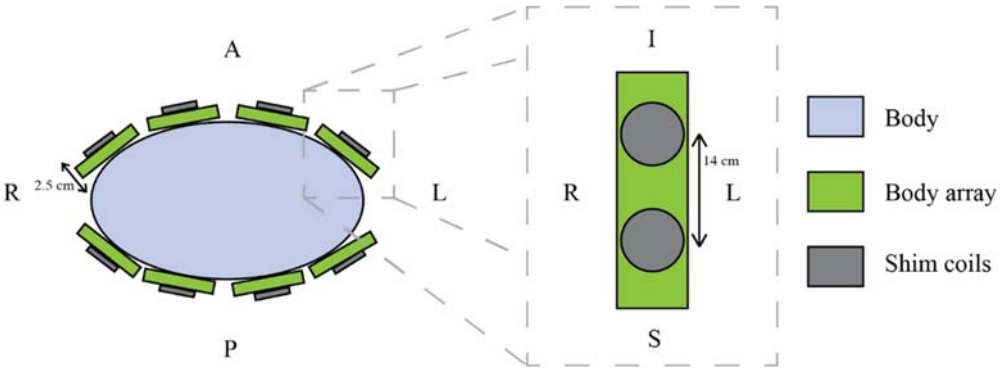

Figure 1: Schematic of the local shim array in combination with the body array showing the position of the local array of shim coils with respect to the body array and the body in the simulation. *A: anterior, P: posterior, R: right, L: left, I: inferior, and S: superior.*

Three types of simulations were performed in this study; case 1) standard hardware shimming of the scanner, case 2) local shimming with the local array of shim coils, and case 3) standard hardware shimming of the scanner in addition with the local array of shim coils (Figure 2). In case 1, the unshimmed B_0 map over the liver performed in the scanner in the different respiratory states is used to fit up to second order B_0 harmonics as standard available. From the simulated shimmed B_0 maps, the mean and standard deviation of the field were calculated and expressed in Hertz (yB_0). The improvement for the shim results in each breathing state was compared to the unshimmed condition; the standard deviation of frequency offsets within the liver was used to calculate the improvement in percentage. In case 2, the unshimmed B_0 maps over the liver of the three respiratory states were fit to the spatial B_0 distribution of the 16 local coils. The mean and standard deviation of the shimmed field as expressed in Hz was compared to the shimmed results of case 1 for each respiratory state. This to assess shimming performance using coils embedded in receivers versus coils embedded in the bore-liner. Finally, in case 3, the unshimmed

B_0 maps were fitted to the 2nd order shim harmonics as well as the 16-channel coil array combined. The improvement in shimming was compared to the shimmed solution of case 1 so to investigate the gain in shim performance when both shim solutions would be available at the same time.

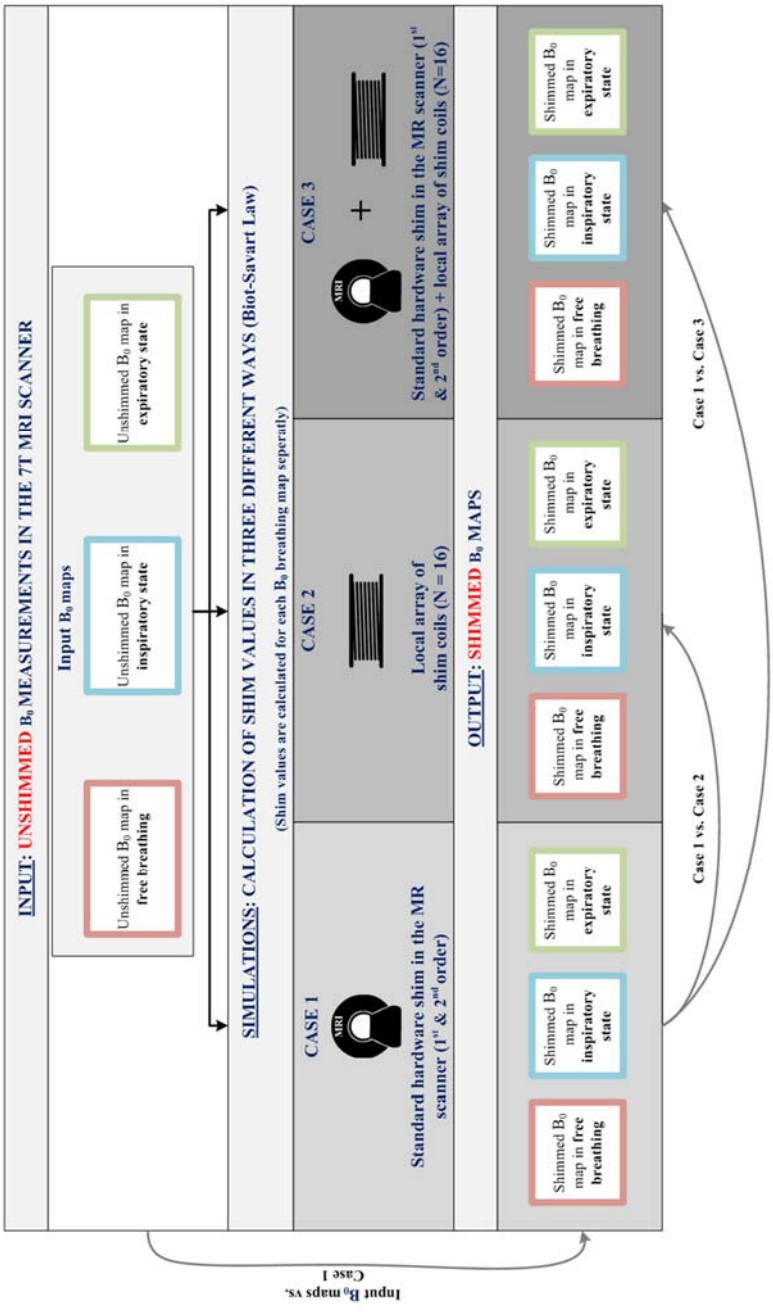

Figure 2: Schematic overview of the performed simulations and comparisons between the different cases. The input of the simulation is unshimmed B_0 maps from the 7 T MR scanner in three respiratory states. In case 1 the standard shimming method is simulated, in case 2 the local array of shim coils and in case 3 both the local array of shim coils in combination with the standard shimming method is simulated. Improvements in B_0 homogeneity using the default shimming hardware in case 1 is investigated by comparing case 1 with the simulation input e.g. the unshimmed B_0 maps. Cases 2 and 3 are compared to case 1 to investigate the additional value of the local array of shim coils compared to the conventional shim hardware.

Results

Five unshimmed dual-echo B0 maps of the liver were acquired in free breathing, inhaled and exhaled state. The livers were segmented in the three different respiratory stages (see Figure 3 for free breathing and inspiratory state examples). Figure 3 has the 2D livers contoured in red, which is later used as the mask in the simulations.

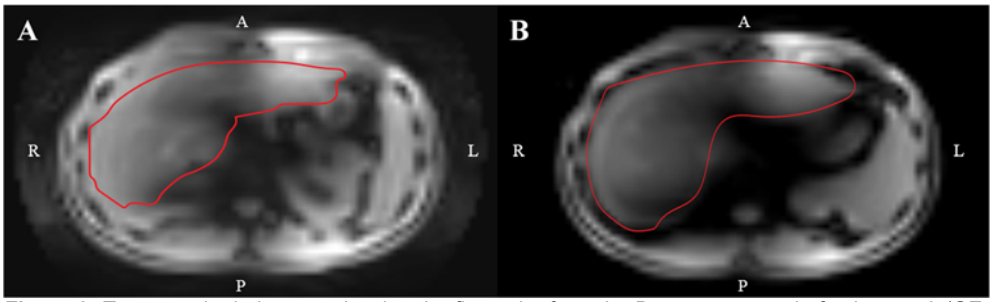

Figure 3: Two magnitude images showing the first echo from the B_0 maps protocol of volunteer 3 (GE, 386 × 410 × 180 mm^3 FOV, 6 × 6 × 6 mm^3 voxel size, FA = 4°, TR = 6 ms, TE = 1.413 ms, ΔTE = 1 ms, slice thickness = 6 mm, number of slices = 30, scan time = 24.1 s) of the liver of volunteer 3. **A)** Free breathing **B)** Inspiratory state. *A: anterior, P: posterior, R: right, and L: left.*

Simulations allowed calculations of the B_0 fields in combination with different shimming methods. From the 3D dataset, a representative 2D transverse slice of the liver is shown in Figure 3 both during free breathing (A) as in inspiration (B). From the same slice an overlay of the different simulated B_0 fields is shown in Figure 4. The B_0 field without shimming (input B_0 map - free breathing) shows a decaying gradient from right to left in the body. Applying the first and second order shim of the scanner, results in an improvement of the B_0 field homogeneity (Figure 4, case 1 - free breathing). In case 2 (Figure 4, free breathing) further improvement is shown in the simulated B_0 field after local shimming with only the local array of shim coils. Finally, we see most improvement in the B_0 uniformity after using standard hardware shimming (1^{st} and 2^{nd}) in addition with the local array of shim coils (Figure 4, case 3 - free breathing). Simulations performed on the free breathing state B_0 maps in all the five volunteers in combination with the standard hardware shimming and the local array of shim coils show an increased improvement in homogeneity of B_0 on the full liver in comparison with the standard hardware shimming in the scanner (10±4.7%) (Table 1).

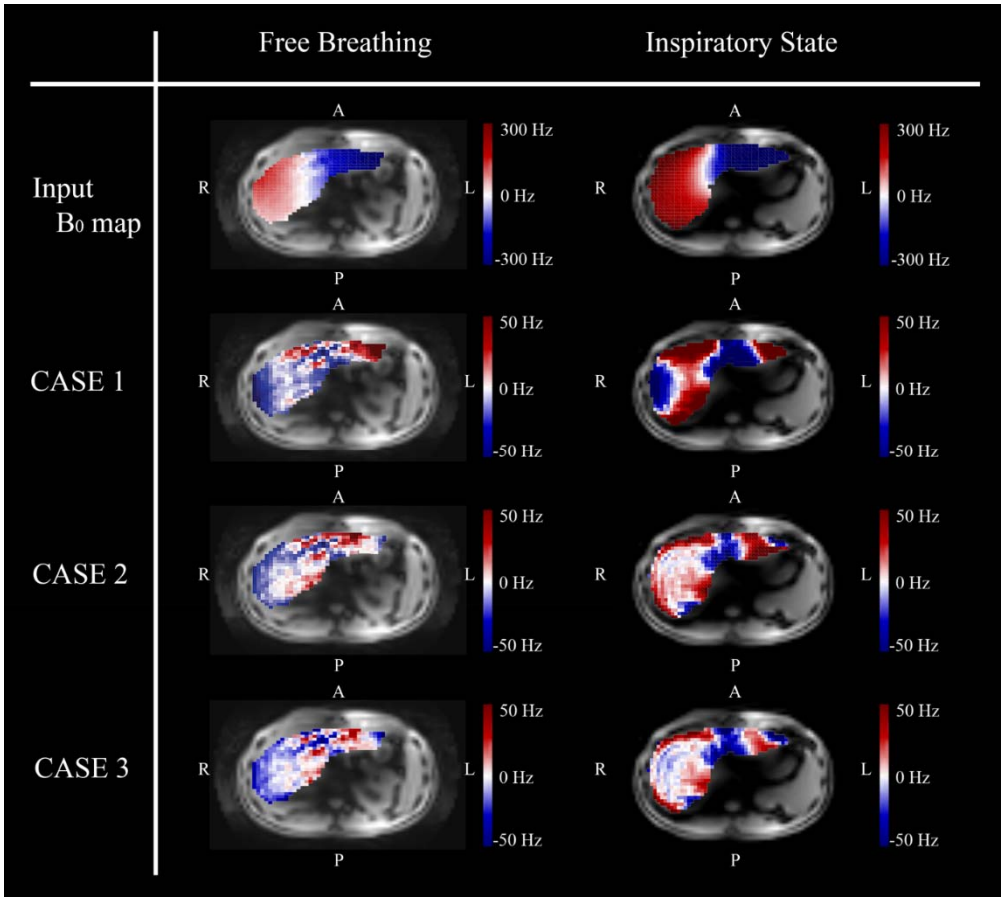

Figure 4: Eight magnitude images showing the first echo from the B_0 maps protocol showing the simulated B_0 field of a single slice in the liver of volunteer 3, obtained during free breathing and in inspiratory state. The non-shimmed input and the three shim cases are shown in the different rows; **input B_0 map)** unshimmed B_0 maps, **case 1)** simulated standard hardware shimming (1st and 2nd order) B_0 maps, **case 2)** simulated local array of shim coils B_0 maps, and **case 3)** simulated standard hardware shimming (1st and 2nd order) in addition with local array of shim coils B_0 maps. *A: anterior, P: posterior, R: right, and L: left. Note: input B_0 map has a different scaling.*

Figure 4 in column inspiratory state shows a 2D slice of the liver in inspiratory state of the same 2D slice of the liver as in Figure 3B, but with different overlays of simulated B_0 fields. The simulated B_0 field with static first and second order shimming (Figure 4, case 2 - inspiratory state) shows improvement compared to the unshimmed B_0 field (input B_0 map, inspiratory state). When using only the local array (Figure 4, case 2 - inspiratory state), it outperforms the standard hardware shimming method by 37% (case 2, inspiratory state; Table 1). The standard hardware shimming in combination with the local array of shim coils increases this improvement to 51% in comparison with only the standard hardware shimming method (Figure 4, case 3 - inspiratory state). In general, there is an improvement of

Improvement of B_0 between the different cases in percentage (%)

	Input B_0 maps vs. case 1			**Case 1 vs. Case 2**			**Case 1 vs. Case 3**		
	Free breathing state	Inspiratory state	Expiratory state	Free breathing state	Inspiratory state	Expiratory state	Free breathing state	Inspiratory state	Expiratory state
V1	56	25	63	8	35	10	13	44	20
V2	69	57	72	13	15	15	14	32	35
V3	69	57	69	15	37	33	16	51	42
V4	54	51	62	5	7	7	4	35	11
V5	60	35	65	3	30	5	6	42	11
MEAN	**62±7.3**	**45±14**	**66±4.2**	**9±4.6**	**25±11**	**14±10**	**10±4.7**	**41±6.7**	**24±12**

Table 1: Improvement in percentage of the B_0 values before and after shimming using the simulations of five volunteers in all three respiratory states. The input B_0 maps are compared to simulations from case 1 using the static 1st and 2nd order shim method in column 1. Case 2, shimming using the local array of shim coils and case 3, shimming using both the local array of shim coils and the static 1st and 2nd shim hardware are compared to case 1 in column 2 and 3 respectively.

B_0 homogeneity in the full liver of the five volunteers (in inspiratory state) of 41±6.7% in average when shimming is performed with standard hardware shimming in addition with the local array of shim coils (Table 1).

The expiratory state also shows an improvement of 24±12% in field homogeneity in the full liver when using the standard hardware shimming with local array of shim coils (case 3) in comparison to case 1, using solely the static first and second order shimming method (Table 1). A summary of all comparisons is shown in Table 1.

Discussion

This study was set out to investigate by simulations whether it was possible to reduce variations in B_0 field in the liver at different respiratory states with standard hardware shimming in addition of a local array of shim coils in comparison with the standard 1st and 2nd order scanner B_0 shim. Simulations show that standard hardware shimming in combination with the local array shim coils in the simulations led to a 10±4.7% improvement of the B_0 shimming during free breathing, 41±6.7% improvement during inspiratory state, and 24±12% improvement during expiratory compared to the standard hardware shimming (Table 1). When using dynamic updating of the local shim coils over the breathing cycle in combination with the standard hardware shimming, there is the potential of a B_0 improvement between 24% and 41%.

As the results showed in Table 1, it is useful to acquire shimmed B_0 maps for every breathing state separately instead of using free breathing shimmed B_0 maps with the standard hardware-based shimming. Using the local array of externally steered coils that maximize the magnetic field homogeneity locally, improvements in the B_0 map during breath-hold are higher than the B_0 improvements seen during free breathing. Due to its smaller size and larger distance to the magnet crystal, the local array of shim coils often has fewer problems with eddy-currents than the higher order harmonic shims embedded in the bore liner of the MRI. Therefore, it may be possible to update them dynamically without the need for complex pre-emphasis so to simplify their use (7).

Normally we use first and second order shimming for the standard scanner hardware to correct for B_0 inhomogeneities, but our scanner hardware is also able to correct up to third order shimming. However, third order shimming corrections often lead to more and sharper variations around the edges of the shimming area when compared to second order shimming in the liver. Outside the optimized region, the third order harmonic shims can cause large offsets which can lead to new artefacts, while the offsets caused by the more condensed local shim array are expected to be substantially less.

Employing the local shim array in-vivo requires knowledge of the positions to perform accurate simulations, meaning a software process that exports the B_0 map including input of the location of all shim coils is necessary. Resulting configurations would be used to automatically steer the local array of shim coils. However, extra B_0 calibration scans are required to obtain the field maps, which when shim coils are embedded in flexible receiver arrays need to be obtained in each scan session.

Because of software and hardware limitations, it currently is not possible to test the local array of shim coils in-vivo. However, during in-vivo measurements motion and torsion of the local array of shim coils that could arise from Lorentz forces generated by the current going through the enameled copper wires in the main magnetic field should be taken into account. Fortunately, calibration procedures can be used to directly map the B_0 field map per unit of current of the actual shim coil. In our study we used simulations instead to investigate the potential gain of local shim strategies without being hindered by potential practical implementation issues.

Since the body itself is the primary source of B_0 distortions in high static magnetic field strengths of 3 T and higher, at ultra-high field MRI systems the need for an improved patient-specific shimming capability becomes evident in order to benefit from the higher spectral dispersion. As expected, the inhomogeneities between different tissue types and tissue-air interfaces can be substantial at ultra-high field MRI systems as also observed in our study. Nevertheless, the presence of a local array of shim coils can recover a substantial part of the B_0 field homogeneity, when compared to solely using the scanner shim.

Conclusion

This study shows that local B_0 field variations in the liver at 7 T can be reduced by using an array of local shim coils. Simulations show that B_0 shimming during free breathing improves by 10±4.7% when using a local shim coil array in combination with the standard hardware shimming when compared to only the standard hardware. However, dynamic updating during the standard hardware shimming method of the scanner in combination with the local array of shim coils lead to a potential B_0 homogeneity improvement of the liver that ranges between the 24% and 41%. As local shimming becomes more important at ultra-high magnetic field strengths, the use of local shim coil arrays will become a necessity, particularly for larger organs such as the liver.

References

1. Maniam S, Szklaruk J. Magnetic resonance imaging: Review of imaging techniques and overview of liver imaging. World Journal of Radiology 2010; 2(8):309-322.
2. Truong Trong-Kha, et al. Effects of static and radiofrequency magnetic field inhomogeneity in ultra-high field magnetic resonance imaging. Magnetic Resonance Imaging. 2006; 24:103-112.
3. Juchem C, de Graaf RA. B0 magnetic field homogeneity and shimming for in vivo magnetic resonance spectroscopy. Analytical Biochemistry 2017;529:17-29.
4. Salomir R, De Senneville BD, Moonen CTW. A Fast Calculation Method for Magnetic Field Inhomogeneity due to an Arbitrary Distribution of Bulk Susceptibility. Magnetic Resonance Engineering 2003; 19B(1):26-34.
5. Brown RW, Cheng YCN, Haacke EM, Thompson MR, Venkatesan R. Magnetic Resonance Imaging: Physical Principles and Sequence Design. Wiley Blackwell. 2nd edition. New Jersey. P 4.
6. Ba-Ssalmah A, Fakhrai N, K Matzek W, M Herneth A, Stadler A, Bastati N, J Herold C, Shima W. Magnetic Resonance Imaging of Liver Malignancies. Top Magn Reson Imaging 2007; 18(6):445-455.
7. Bhogal A, Versluis M, Koonen J, Siero J.C.W., Boer V.O., Klomp D., Luijten P.R., Hoogduin H. Image-Based Method to Measure and Characterize Shim-Induced Eddy Current Fields. Concepts in Magnetic Resonance Part A 2013; 42(6): 245-260.
8. Spielman DM, Adalsteinsson E, Lim KO. Quantitative assessment of improved homogeneity using higher-order shims for spectroscopic imaging of the brain. Magn Reson Med 1998; 40:376–382.
9. Pan JW, Lo KM, Hetherington HP. Role of high order and degree B0 shimming for spectroscopic imaging of the human brain at 7 Tesla. Magn Reson Med 2012; 68:1007-1017.
10. Juchem C, Nixon TW, Diduch P, Rothman DL, Starewicz P, de Graaf RA. Dynamic Shimming of the Human Brain at 7 T. Magnetic Resonance Engineering 2010; 37B(3):116-128.
11. Juchem C, Nixon TW, McIntyre S, Boer VO, Rothman DL, de Graaf RA. Dynamic multi-coil shimming of the human brain at 7 T. Journal of Magnetic Resonance 2011; 212(2):280-288.
12. Pan JW, Lo KM, Hetherington HP. Role of very high order and degree B0 shimming for spectroscopic imaging of the human brain at 7 T. Magn Reson Med. 2012; 68:1007–1017.
13. Steensma BR, Voogt IJ, Leiner T, Luijten PR, Habets J, Klomp DWJ, van den Berg CAT, Raaijmakers AJE. An 8-channel Tx/Rx dipole array combined with 16 Rx loops for high-resolution functional cardiac imaging 7 T. Magnetic Resonance Materials in Physics, Biology and Medicine 2018; 31:7-18.
14. Young HD, Freedman RA. University Physics with Modern Physics. Pearson Education Limited. 14th edition. Global edition. P 948-949.

Chapter 4

Low SAR ^{31}P (multi-echo) spectroscopic imaging using an integrated whole-body transmit coil at 7T

Quincy van Houtum

Dimitri Welting

Mark (W.J.) Gosselink

Dennis (W.J.) Klomp

Catalina (S.) Arteaga de Castro

Wybe (J.M.) van der Kemp

NMR in Biomedicine 2019

Keywords: X-Nuclei, MRSI, SAR, In Vivo, RF, Quantification, fast acquisition.

Abstract

Introduction & methods: Phosphorus (^{31}P) MR spectroscopic imaging provides opportunities to monitor potential biomarkers. However, current applications of ^{31}P MRS are generally restricted to relatively small volumes as small coils are used. Conventional surface coils require high-energetic adiabatic RF pulses to achieve flip-angle homogeneity, leading to high specific absorption rates (SAR) and occupy space within the MRI bore. A birdcage coil behind the bore cover can potentially reduce the SAR constraints massively by use of conventional amplitude modulated pulses without sacrificing patient space. Here, we demonstrate that the integrated ^{31}P birdcage coil setup with high power RF amplifier at 7T allows for low flip-angle excitations with short TR for fast 3D CSI and 3D T_1-weighted CSI as well as high flip-angle multi-refocusing pulses, enabling multi-echo CSI that can measure metabolite T_2, over a large FOV in the body.

Results: B_1^+ calibration showed a variation of only 30% in maximum B_1 in four volunteers. High SNR MRSI was obtained in the gluteal muscle using two fast *in vivo* 3D spectroscopic imaging protocols, with low and high flip angles, and with multi-echo MRSI without exceeding SAR levels. In addition, full liver MRSI was achieved within SAR constrains.

Discussion: The integrated ^{31}P body coil allowed for fast spectroscopic imaging and successful implementation of the multi-echo method in the body at 7T. Moreover, no additional enclosing hardware was needed for ^{31}P excitation, paving ways to include larger sized subjects and more space for receiver arrays. The increase in possible number of RF excitations per scan time, due to the improved B_1^+ homogeneity and low SAR, allows to exchange SNR for spatial resolution in CSI and/or T_1 weighting by simply manipulating TR and/or flip angle to detect and quantify ratios from different molecular species.

Abbreviations: Adiabatic multi-echo spectroscopic imaging **(AMESING)**, Magnetic Resonance Spectroscopic Imaging **(MRSI)**, Adenosine triphosphate **(ATP)**, Chemical Shift Imaging **(CSI)**, Free induction decay **(FID)**, Glycerophosphoethanolamine **(GPE),** Glycerophosphocholine **(GPC)**, Multi-echo spectroscopic imaging **(MESING)**, Phosphorus **(^{31}P)**, Phosphocreatine **(PCr)**, Phosphocholine **(PC)**, Phosphodiesters **(PDE)**, Phosphoethanolamine **(PE)**, Inorganic Phosphate **(Pi)**, Phosphomonoesters **(PME)**, specific absorption rate **(SAR)**, repetition time **(TR)**.

Introduction

Phosphorus (^{31}P) MR spectroscopic imaging provides opportunities to monitor tissue metabolism by measuring specific energy- and phospholipid-metabolites. Phosphocreatine (PCr), ATP (with α-, ß- and*γ*-resonances) and inorganic phosphate (Pi) give insight into cell energy metabolism. Decreased PCr/ATP ratios in the heart can be used as diagnostic indicators in systemic diseases such as type 2 diabetes and obesity.[1–3] Inorganic phosphate (Pi) can be used to calculate tissue pH as its resonance frequency changes with the acidity of the environment. Phosphomonoesters (PME) and phosphodiesters (PDE) allow assessment of phospholipid metabolism.[4–6] At ultra-high field (>7 tesla), the increased SNR and increased spectral resolution facilitate the individual detection of phosphomonoesters (PC, PE) and diesters (GPC, GPE)[7]. Enhanced PME to PDE ratios (PC to GPC, PE to GPE) are indicative of proliferation and are often seen in tumor tissue [5,6,8–13]. A change in these ratios during (chemo) therapy are markers of therapy response and take place well before morphological changes can be observed[14–16].

Still, these potential biomarkers are monitored generally to quantify metabolite concentrations or to investigate ratios between different molecular species, thus requiring solely a metabolite density weighted signal. From proton MRI it is known that most clinically relevant contrast, when compared to proton density weighted MRI, is obtained from T_1-and T_2-weighting. In fact, one study showed that in ^{31}P spectra the T_2 relaxation itself may be used as a marker in breast cancer and another study reported that intra-mitochondrial and cytosolic inorganic phosphate (Pi) can be discriminated based on T_1 differences [17,18].

However, current applications of ^{31}P MRS are generally restricted to relatively small volumes such as the brain, breast, and calf muscle as small birdcage or conventional surface coils are used[4,19]. Conventional surface coils require high energetic adiabatic RF pulses to achieve flip angle homogeneity, as inhomogeneous excitation leads to discrepancies in spectra over larger fields of view. Consequently, this can lead to high specific absorption rates (SAR), thus limiting the number of consecutive scans, particularly when considering metabolite relaxation parameter quantifications, fast spectroscopy methods or T_1-and T_2-weighted sequences.

Recent work by Van der Kemp et al. showed an adiabatic multi-echo spectral imaging (AMESING) sequence, which included voxel specific T_2 quantification of the different metabolites in the acquired spectrum [8,18]. This allowed T_2-weighted SNR enhancement, for an increased metabolite sensitivity, or T_2 information per metabolite. In the so-called AMESING sequence, uniform excitation is achieved using adiabatic half pass RF pulses and the homogeneous refocusing with adiabatic BIR-4 180° pulses, which require high B_1^+ (~100 μT) and relatively long pulse

durations (8ms). These pulses are therefore SAR demanding and consequently restricted to body surface applications.

Moving to larger field of views in the body is therefore challenging, as greater B_1 field discrepancies are present with inhomogeneous excitation. Application of larger surface coils and adiabatic pulses would require even more power, which would limit the acquisition even more. In addition, long repetition times necessary for sufficient spin relaxation between pulses and for minimization of average SAR, result in clinically impractical scan times for a single protocol.

To achieve uniform $B_1^{+/-}$ fields such as with conventional ^{1}H MRI, small X-nuclei RF-birdcage coils for head and extremities allow for diverse pulse sequences and enable numerous contrasts. Indeed even multi-echo acquisitions in the brain at 7T are possible within SAR guidelines using these plug-and-play devices[19].

In another recent publication, Löring et al. showed an insertable ^{31}P birdcage body coil that can produce uniform B_1 fields, thus allowing the use of rectangular RF pulse excitations[20]. This birdcage coil is wide enough to accommodate the human torso, allowing ^{31}P MRSI of the human body, yet occupies space from the bore limiting inclusion of heavy patients and reduces space for receiver coils. Löring et al. did show the application of low-flip Ernst-angle excitations, with accompanying short repetition times (TR), which can result in fairly homogeneous excitation fields over the entire spectral bandwidth for in vivo ^{31}P MRS at 7T and acceptable scan times over a larger field of view.

In this work, we present that the permanent installation of a ^{31}P body coil behind the covers of the patient tube, i.e. without sacrificing patient space, while interfacing to a high-power RF amplifier, increases its usability. The reduction in SAR with this body coil allows the use of rectangular and even multiple rectangular composite pulses. Applications on the large gluteal muscle and liver are shown, including low flip angle excitation with short TR for fast 3D CSI and 3D T_1-weighted CSI, as well as high flip angle multi-refocusing pulses enabling multi-echo CSI, over a large FOV.

Methods

Coil setup

31P-MRSI was performed using an in-house designed birdcage body coil, permanently integrated into a 7 tesla MRI system (Philips Healthcare, Best, Netherlands), with a bore diameter of 60 cm for full body coverage. The coil, tuned at 120 Mhz was interfaced to and driven by a 25kW RF amplifier for a B1+field of 15μT at the center of the bore (Figure 1A)[21]. Two overlapping phosphorus receiver coils (10 x 16 cm2) in quadrature mode and two separate fractionated dipole antennas (30 cm) for proton imaging were used in quadrature transceiver mode[21].

The proton antennas were positioned on the left and right side of the phosphorus receiver coils as can been seen in figure 1A and B.

In vitro and in vivo setup

In vitro measurements were performed on a body-sized phantom created from a barrel (Ø27 cm, height 38 cm) filled with foam, normal saline and a small sphere (Ø4 cm) filled with a 1 M Pi solution. The composition ensured loading matched to a human body for both the ^{31}P coils and ^{1}H antennas during measurements. For the *in vivo* measurements four healthy volunteers, three males and one female, with a BMI range of [21.6 - 26.5], were imaged in prone position with the gluteal muscles at the isocenter of the MR bore.

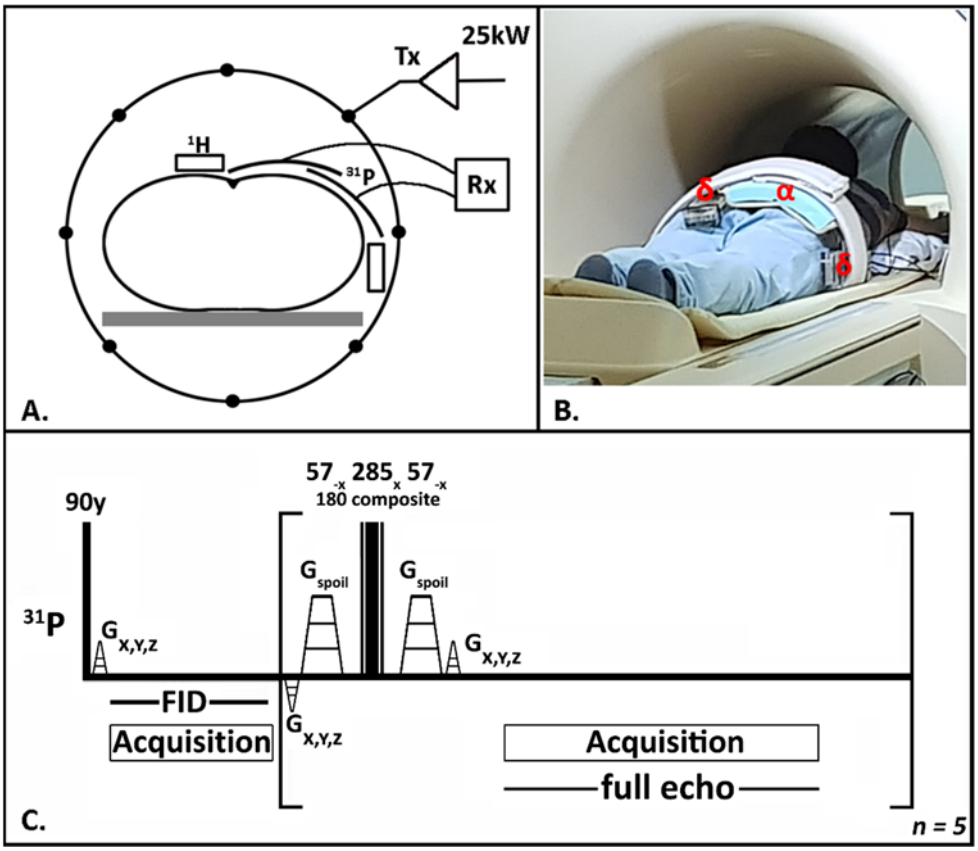

Figure 1. A) Schematic of the ^{31}P body MRSI setup with the integrated birdcage body coil for transmit represented by the circle including the 25 kW power supply, the ^{31}P receiver coils shown by the two arcs, the blocks for the two dipole antennas and the subject centered in the body coil and MR bore. **B)** Photo of the setup showing a volunteer on the MR bed with the full imaging setup installed including (**α**) the ^{31}P receiver loops, (**δ**) proton dipole antennas and noticeable absence (behind patient tube) of the ^{31}P body coil, corresponding to the schematic in A. **C)** The pulse sequence of the multi-echo spectroscopic imaging protocol with rectangular pulse excitation, refocusing composite block pulses plus the encoding and spoiling gradients.

The ^{31}P receiver coil and proton imaging setup were placed on the gluteal muscles of the volunteers. One volunteer was imaged in right decubitus position with the ^{31}P receiver coils positioned at liver height, between the bed and the volunteer. The study was approved by the UMC Utrecht Medical Ethical Review Board and all volunteers gave written informed consent.

MR data acquisition

First, a proton image for anatomy localization followed by a B_0 map for image based B_0 shimming, were obtained. To make sure that the flip angles (FA) were kept similar for all volunteers, a FA calibration with the carrier frequency set to PCr (i.e. set to 0 ppm), was made. The ^{31}P B_1^+ field calibration was done with a non-localized block pulse sequence with a series of increasing flip angles and a TR of 2500 ms, which included gradient spoiling. The zero-crossing of the signal intensity, marking the actual 180° angle e.g. no signal, was used to adjust output power.

Two fast chemical shift protocols using rectangular block pulses with the carrier frequency set to PCr, one with maximized signal intensity for Pi using the Ernst angle for Pi based on a T_1 of 4300ms and another at a higher flip angle to increase T_1-weighting, were acquired at an isotropic resolution of 40 mm, matrix size 10 x 6 x 6; 512 acquisition points; BW 8000 Hz; TR of 150 ms, flip angle, α of 16°and 40°, number of averages 10 and included elliptical k-space sampling resulting in a scan duration of 7:03 min[17,22].

A multi-echo spectroscopic imaging protocol (MESING), shown in figure 1C, was used in order to acquire a single free induction decay (FID) by means of a pulse acquire and five full echoes in one k-space step, while k-space data was sampled spherically[8,19]. The sequence was modified such that the excitation was performed using a rectangular 90° pulse at 15 μT, followed by a composite refocusing made out of three rectangular RF pulses of equal B_1^+ amplitude and flip angles of $57°_{-x}$, $285°_{x}$ and $57°_{-x}$ for a refocusing bandwidth of 2 ppm. The refocusing part of the sequence is repeated five times to obtain five echoes. The carrier frequency of all pulses was set to Pi and PCr for the *in vitro* and *in vivo* experiments respectively. The latter was based on the bandwidth of the refocusing pulses and the *in vivo* ^{31}P metabolite with the highest concentration (PCr), which results in increased signal intensity favoring SNR. Both the *in vitro* and *in vivo* experiments with MESING were performed with an isotropic resolution of 40 mm with the carrier frequency set to Pi and PCr respectively. Other parameters were TR, 5000 ms; ΔTE, 45ms; BW, 7800 Hz; Matrix, 8 x 8 x 6; 256 acquisition points and a scan duration of 21:20 min. The *in vitro* experiment was used to validate the adapted protocol and applicability over a large field of view *in vivo*.

Liver spectra were acquired using a 3D ^{31}P chemical shift imaging protocol with Hamming weighted acquisition at a 15mm isotropic nominal resolution. The flip angle of 8° and a TR of 60 ms were chosen for optimal SNR with the Ernst angle for GPE and GPC assuming a T_1 of around 6000 ms [23]. The carrier frequency was set to PCr and other CSI parameters were TE, 0.44 ms; Bandwidth, 4800 Hz; matrix size, 12x8x8; NSA, 80 and 256 acquisition points for a total scan duration of 21:48 min.

Data Processing

All ^{31}P MRSI data were processed in Matlab 2017 (The MathWorks Inc., Natick, MA). Calibrations of the phosphorus B_1^+ field from all volunteers were summarized by using the peak intensity of phosphocreatine of each FA dynamic scan obtained per volunteer after apodization in the time domain with a Gaussian filter of 30 Hz. Shown data were normalized using the maximum signal intensity of each volunteer and the inter-subject variation was calculated using the variation in the periods of each individual fit per volunteer using equation 1.

$$SI = \frac{\sin\alpha\,(1-e^{-\frac{TR}{T1}})}{(1-e^{-\frac{TR}{T1}}\cos\alpha)} \qquad [1]$$

3D Multi-echo spectral data were spatially filtered using a 3D hamming window, followed by inverse Fourier transformation to the spatial domain. FID and echoes were apodized using a 40 Hz Gaussian filter and *in vivo* data were zero filled to double the number of samples thereafter. First order phase correction was applied to the FID by circular shifting the first missing data points resulting from the acquisition delay. T_2 of the metabolites was calculated by fitting a mono-exponential model as described in [Eq. 2] using the Levenberg-Marquardt algorithm.

$$SI = S_0 * e^{-\frac{TE}{T_2}} \qquad [2]$$

All other 3D chemical shift imaging data were averaged, spatially filtered using a 3D hamming window and transformed to the spatial domain by inverse Fourier transformation. The FIDs were apodized in the time domain with a Gaussian filter of 40 Hz and 24 Hz for the gluteal muscle and liver respectively and zero filled to double the number of samples. Phase corrections were applied manually, thereafter.

Results

All subjects fitted well in the ^{31}P whole body coil setup as this coil is integrated within the MRI, behind the covers of the bore, providing sufficient space for the dipole transceivers and receive loops as shown in Figure 1A and B. The flip angle sweep acquired in four volunteers (different coil load) for B_1^+ calibration of the ^{31}P whole body coil is shown in figure 2 and the average variation in maximum B_1 between the volunteers was 30% using 23 kW as peak power. Variation of B_1^+, as indirectly observed from the FA series, remains low despite differences in coil load from the volunteers (BMI range 21 – 26 kg/m^2). The power settings were corrected for each volunteer, based on the interpolated zero crossing at 180° that is independent of T_1 relaxation, to achieve the right flip angle on the subsequent acquisitions.

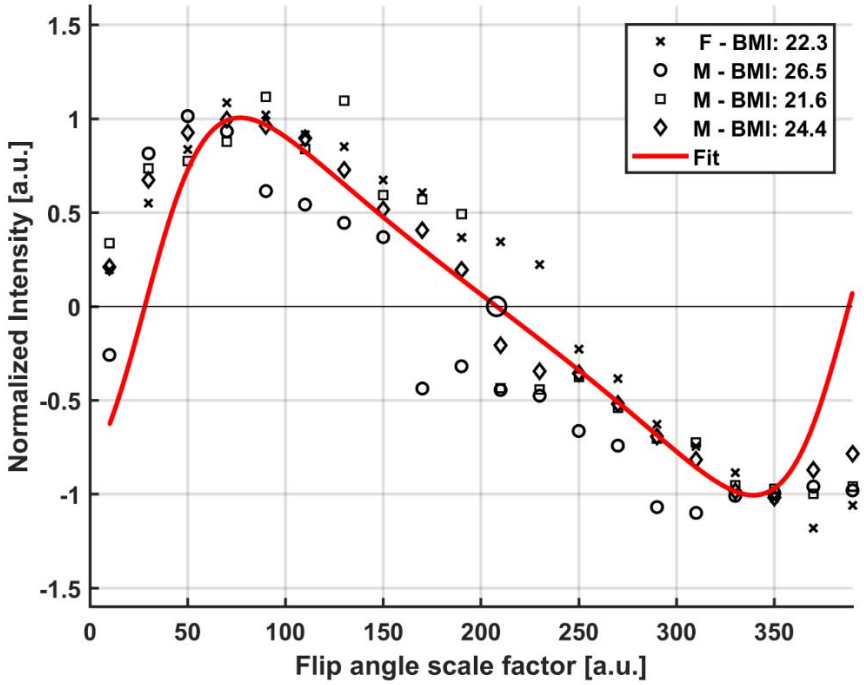

Figure 2. *In vivo* flip angle series showing the excitation profiles for all four volunteers showing the maximum PCr peak versus each flip angle scale factor. An average inter-subject variation of 30% was calculated. Body mass index and gender of each volunteer is denoted in the legend. T_1 relaxation effect is apparent from the asymmetry of the 90° vs. 180° pulses and mirrored 360° degrees pulse due to not fully relaxed spins. The zero-crossing of the fit for calculating correct power adjustments is marked by the larger black circle.

The integrated body coil in combination with the quadrature ^{31}P receive loops showed high SNR ^{31}P MRSI (3.9 for PME to 82 for PCr), as shown in the spectra in figures 3 to 6. B_0 shimming and partial volume effects were suboptimal over such large FOV, with a measured line width of 0.20 ppm before apodization. T_1-weighting is apparent from the relative decrease of PCr and increase of α- and γ-ATP resonances in figure 3C compared to figure 3D. In addition, the β-ATP peak is decreased and the PDE peak shows a similar but minor decrease. An increase of the Pi signal is noticed in figure 3D compared to 3C.

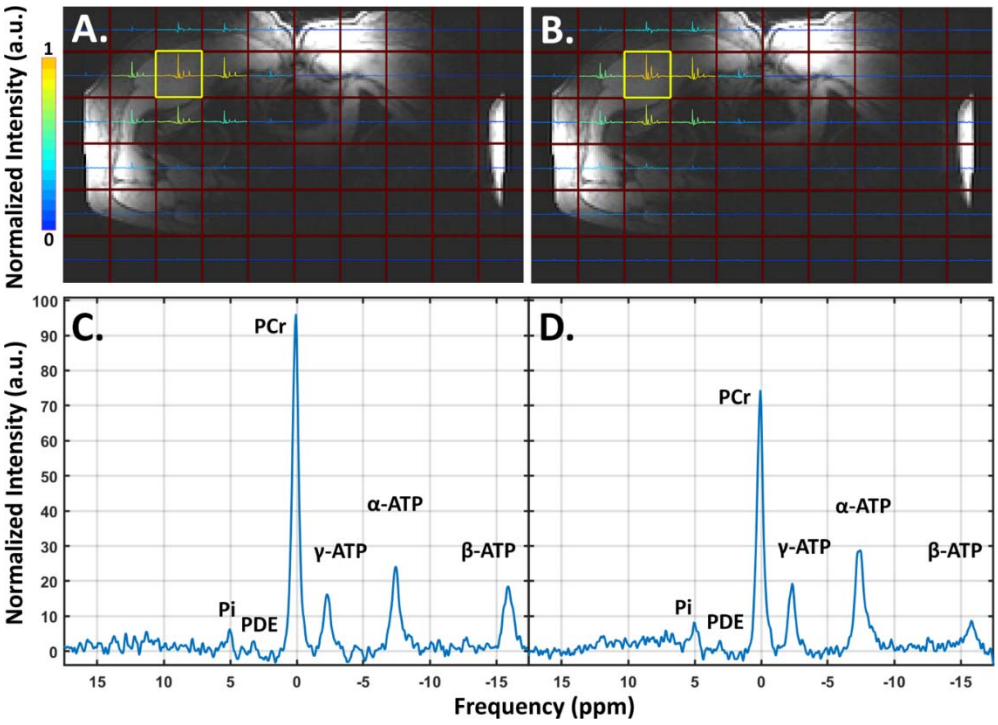

Figure 3. Two spectral images of the *in vivo* 3D CSI data sets projected on the MR localizer image with **A)** a low flip angle (16°) and **B)** a high flip angle (40°) with same TR (150 ms). Spectral data shown in A and B are normalized to the maximum signal and the y-axes of all voxels are scaled to the maximum signal in the 2D spectral images. Two *in vivo* T_1 weighted spectra of **C)** the voxel highlighted by the yellow square in A and **D)** the voxel highlighted in B, normalized to the noise of each spectrum. Data were acquired using the quadrature mode receiver coil setup in combination with the ^{31}P body coil and TR and flip angles were chosen to introduce T_1-weighting. The metabolite peaks of inorganic phosphate (Pi), the phosphodiesters (PDE), phosphocreatine (PCr) and α-, ß-, and γ-ATP are labeled in both individual spectra.

The MESING data were acquired well within SAR limits and with sufficient SNR to allow T_2 fitting (Figure 4 and 5). The MESING refocusing 180° composite block pulse used 15 µT and was 4.26 ms long, which compared to the 100 µT adiabatic RF pulse of 8 ms of the AMESING sequence used in the breast by van der Kemp et al, resulted in an 83-fold reduced effective B_1 integral. In vitro average T_2 of inorganic phosphate in the phantom using the MESING method resulted in 232 ± 35 ms (Figure 4) and the T_2 of phosphocreatine from a single volunteer measured 177 ± 35 ms (Figure 5). Base-line roll artefact is visible in the FID in figures 4C and 5C resulting from equal data processing of FID and echoes by correcting for the bandwidth difference. As the ^{1}H antennas are inherently decoupled from the ^{31}P coils, adequate ^{1}H MR images for localization could be obtained shown by the proton images in figures 4B and 5B.

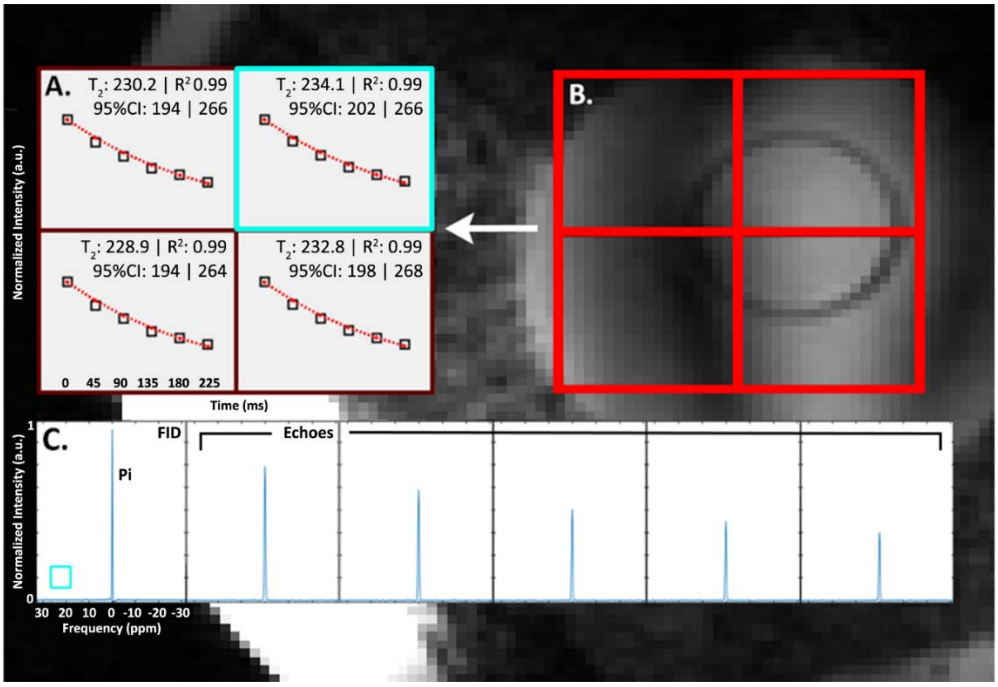

Figure 4. A) *In vitro* T_2 measurement of inorganic phosphate in the body-sized phantom using the multi-echo spectral imaging sequence for each voxel in **B)** the red grid on the localizer image of the sphere. The normalized maximum peak value for the FID and each echo plus the corresponding fit are denoted as black squares and a red dotted line respectively. Average T_2 over all four voxels for the Pi contained in the small sphere was 232 ± 35 ms. **C)** The spectra of the FID and five echoes for the single voxel highlighted by the blue square, acquired using the ^{31}P dual coil receiver in combination with the ^{31}P body coil. The frequency scaling shown for the x-axis of the FID is equal for all other echoes.

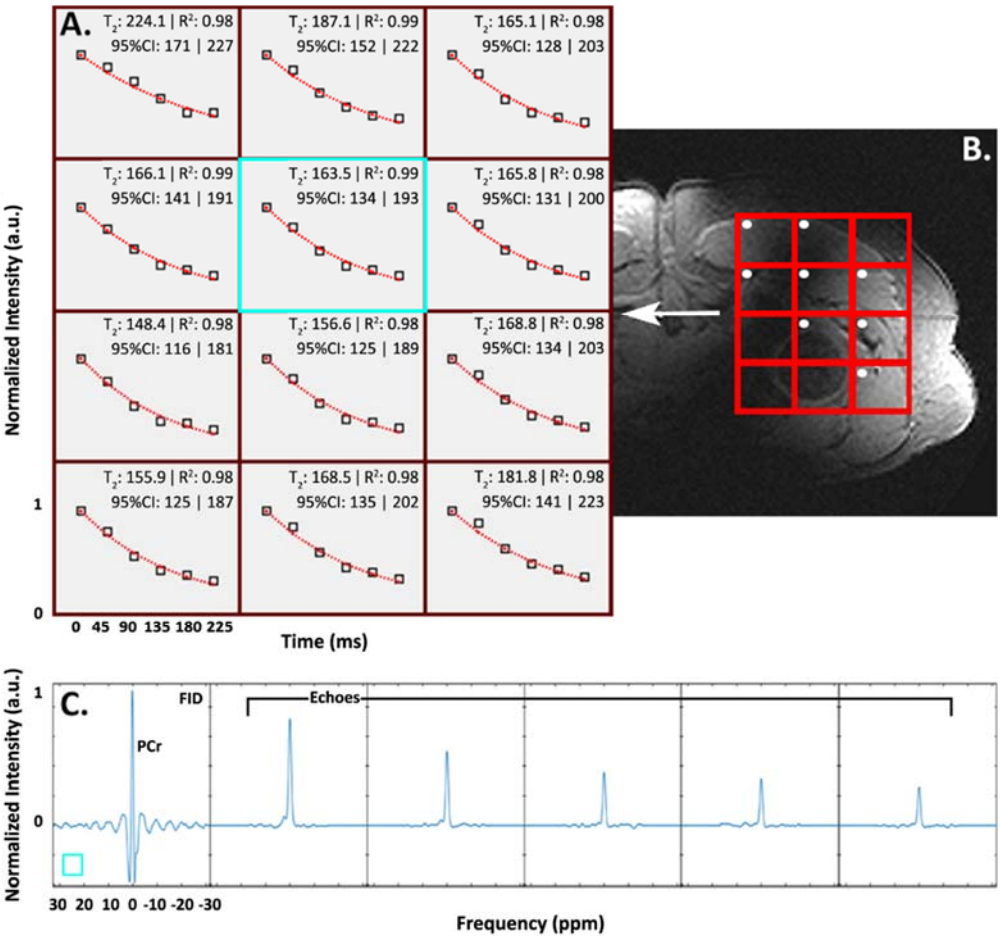

Figure. 5. A) *In vivo* T_2 fits of phosphocreatine using the multi-echo spectroscopic imaging data from a single volunteer in voxels corresponding to the gluteal muscles as shown by the red grid in **B)** the T_1-weighted localizer image. Normalized maximum peak value for the FID and each echo are denoted as open squares and the red dotted lines represent the fit. Echo times applicable to all voxels are shown in the bottom left. Average T_2 from all voxels with high muscle tissue content, denoted by the white dots, was 177 ± 35 ms. **C)** Spectra of the FID and five echoes for the voxel highlighted by the blue square, acquired using the ^{31}P dual coil receiver in combination with the ^{31}P body coil. The frequency scaling shown for the x-axis of the FID is equal for all other echoes.

Averaging four local liver voxels from the 3D CSI protocol resulted in sufficient SNR to discriminate PD, PC, GPC, GPE, Pi and ATP resonances (Figure 6). The yellow voxels in figure 6B indicate voxels origin and a residual opposite phased PCr peak, denoted by an arrow, is visible in the spectrum.

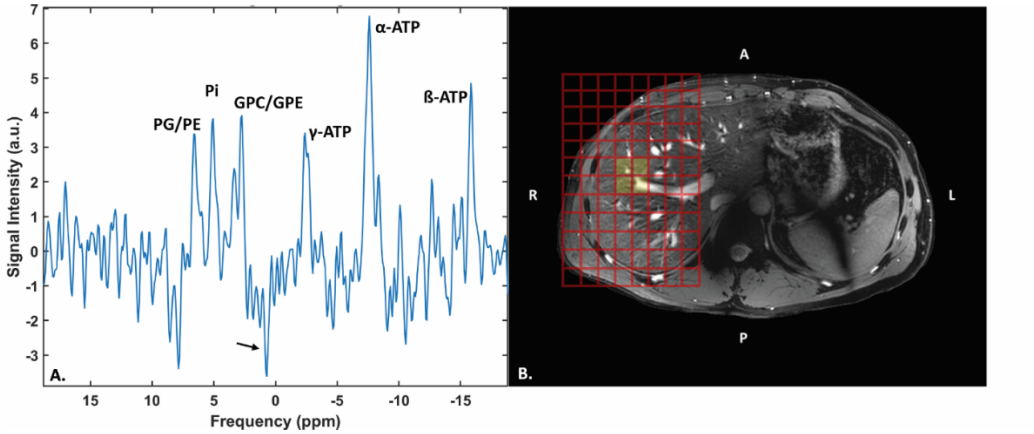

Figure 6. A) Liver spectrum after averaging all liver voxels from the 3D CSI protocol shown in **B)** the localizer image. Data was acquired with the ^{31}P whole-body transmit coil in combination with the ^{31}P receiver coils in quadrature mode. Metabolite peaks of PME, Pi, PDE and the three ATP resonances are denoted. The arrow points to the opposite phased PCr resulting from residual signal contamination from the muscles.

Discussion

Multiple, SAR demanding, body oriented ^{31}P MRSI methods were explored successfully using the fully integrated ^{31}P whole body coil at 7 tesla. Power calibrations of the homebuilt bird-cage coil in multiple volunteers showed consistent performance with 30% inter-subject variability of coil load. Metabolic information from the gluteus maximus and the full liver was acquired, and the multi-echo chemical shift imaging method was successfully implemented. Simultaneous use of the ^{31}P receiver coils with the ^{1}H transceiver antennas preserved volunteer comfort as more freedom was experienced due to the lack of additional enclosing hardware that normally a ^{31}P transmit coil would require. The ^{31}P whole body coil with uniform excitation in the body, enabled the use of low demanding SAR, conventional rectangular RF pulses instead of the high energetic adiabatic RF pulses required with conventional surface coils for achieving homogeneous excitations. This decreases overall SAR, increasing the number of possible RF excitations per scan time to permit reduction of acquisition duration by decreasing TR or even the use of high flip angles, in ^{31}P MRSI.

B_1^+ field homogeneity was assessed from designs by Löring as our design is merely scaled to the bore size. The homogeneity of the insert was shown from the use of B_1-maps from 3 T proton MRI, which have identical diameter and coil layout as the present ^{31}P body coil and are tuned to almost the same frequency[20].

Liver spectra were acquired over a large field of view and with minimal signal contamination by positioning the volunteer in right decubitus position, weighted k-space acquisition and small voxel size. Increasing the number of sample averages regained SNR per voxel. This allowed discrimination of the mono-and di-esters, PE, PC and GPC, GPE, respectively.

MESING was validated on a phantom with inorganic phosphate as the average T_2 of 232ms found corresponded to the T_2 of the body-sized phantom measured with the conventional AMESING sequence from Kemp et al. (data not shown)[8]. The *in vivo* application of MESING showed an average T_2 of PCr in the gluteal muscle of 177ms ± 35 ms, which is comparable to the reported T_2 value of PCr in the calf muscle of around 217 ± 14 ms[8,24]. Note that the T_2 value measured by Bogner et al (23) is an average of seven volunteers, where individual physiological differences between volunteers are averaged out, while our measured value in the gluteal muscle is an average from multiple voxels for just one volunteer, without averaging out possible physiological differences. Another possible cause for a difference in T_2 is sub-optimal refocusing pulses caused by imperfect power adjustments, however the flip angle sweep in figure 2 shows only little variance between subjects, making it less probable to be the source of a lower T_2. A difference in physiology of the gluteal muscle compared to the calf muscle, could result in a slightly higher chemical exchange rate between PCr and ATP, which leads to a lower T_2 [18,19,25].

The T_2 relaxation property of the metabolites, acquired with MESING provided a higher information density from the phosphorus spectra compared to a conventional MRSI experiment. Because metabolite-specific MR properties are available, the signal of each individual metabolite of interest can be corrected for T_2 blurring during acquisition, subsequently favoring SNR or used as a new contrast for each metabolite. This increases diagnostic significance and allows for new research in molecular dynamics and tissue environments. It can also be of interest to areas where B_0 shimming can be difficult, as the reduced spectral SNR caused by static B_0 inhomogeneities could be regained using the MESING method. In conventional proton MRI, T_2 is an important biomarker to discriminate tumor from healthy tissue, aiding in diagnosis and disease prognosis. However, MRI focuses on morphological changes whilst metabolic changes occur prior to any observable structural alterations, creating opportunities for MRSI[26,27]. T_2 contrast in MRSI however, is still not available in the clinic but may increase insight in diseases when used as a biomarker including relaxation information for each metabolite separately. Though

quantification of metabolite concentrations requires no transverse nor longitudinal relaxation weighting, it has recently been shown by van der Kemp et al. that shortening of the transverse relaxation time of inorganic phosphate can be used as a biomarker in breast cancer spectroscopy[18].

In our T_1 weighted ^{31}P MRSI focusing on Pi, we choose two TR and flip angle combinations, which remained close to and deviated from the optimal Ernst angle condition for cytosolic Pi, allowing for T_1-weighting with the latter condition. Other metabolites are T_1-weighted in both situations; however, the weighting is amplified for PCr, PME and PDE with T_1 relaxation rates in the order of several seconds (≥ 3.1 s), whereas the optimal Ernst angle condition is almost met for the β- and γ-ATP resonances with T_1 relaxation rates of around 1800ms in the high flip angle experiment[24]. As such, SNR remained high and T_1 contrast fair, as can be seen by the increased peaks of γ-and α-ATP resonances and decrease of PCr. The observed decrease of the ß-ATP peak in our measurements can be explained by the decreased excitation bandwidth at higher flip angle. Figure 3C and D show minor change between the two Pi peaks with respect to the noticeable decrease of PCr. Theoretically this could suggest an increase in signal contribution from intra-mitochondrial Pi.

The adaptation of the RF pulses to operate at 15 μT rather than 100 μT comes at the cost of a lower pulse bandwidth. The implemented composite refocusing pulse used in MESING has a bandwidth of less than 240 Hz. However, setting the carrier frequency to PCr resulted in higher SNR compared to lower concentrated metabolites and allowed validation of the adapted sequence *in vivo*. The use of multiband RF pulses may be considered to broaden the bandwidth, or in analogy with multi-slice TSE, rather than exciting slices sequentially within the TR, multiple narrow band excitations could be combined to cover the entire spectrum within the same scan time. As RF power deposition with conventional RF pulses is substantially decreased, more alternative pulse sequences, similar to pulses used in proton MRI, can be applied.

In our study we have used a 2-channel receiver array, merely to demonstrate the feasibility of body-oriented ^{31}P MRSI. When expanding the receiver array to a total of 16 or 32 elements, as already shown by Valkovič et al., full body coverage can be obtained[28]. Combined information from multiple coils around the body could increase field of depth as SNR and subsequently sensitivity can be regained by strategic coil combinations methods such as whitened singular value decomposition [29]. The space requirements for such setup may be comparable to conventional clinical MRI receiver arrays, where 16 channel body arrays are being used on regular basis. The ^{31}P receivers, as demonstrated here, can be merged with the relatively thin dipole antennas as can been seen in figure 1A and B, without efficiency losses[20].

While we have shown that a uniform transmit field with highly sensitive reception fields can be achieved with the whole-body coil and merged with a ^{1}H imaging setup, care must be taken in optimizing scan protocols for motion artifacts and B_0 shimming. The MESING sequence can be used to regain SNR loss caused by imperfect B_0 shimming, but will not compensate for dynamic B_0 changes, nor will it improve line widths. Real time dynamic shimming using training sets or field cameras can improve spectral resolution, yet they require even more additional hardware[30–32]. Another alternative could be to use rapid MRSI techniques that include (compressed) SENSE, EPI or spiral readouts, in principle facilitating single shot MRSI acquisitions, where each shot can be frequency aligned prior to averaging[22]. Still, even without any of these techniques, spectral ^{31}P resolution at 7 T was 0.20 ppm, sufficient to discriminate the metabolites of interest in the human body. However, increased spectral resolution would allow improved discrimination of for instance the two Pi species.

Conclusion

The homebuilt fully integrated ^{31}P body coil allowed ^{31}P MRS methods to be explored that would have been SAR demanding with surface coils. Without sacrificing bore space, the improved hardware allowed full liver coverage ^{31}P MRSI and a multi-echo sequence, with inherently lower SAR, was successfully implemented for use in the body. The latter technique, though with improvements, allows for further research into new approaches in MRS biomarkers and additional metabolite specific information.

References

1. Hwang J-H, Choi CS. Use of in vivo magnetic resonance spectroscopy for studying metabolic diseases. *Exp Mol Med*. 2015;47(2):e139. doi:10.1038/emm.2014.101
2. Hwang J-H, Stein DT, Barzilai N, et al. Increased intrahepatic triglyceride is associated with peripheral insulin resistance: in vivo MR imaging and spectroscopy studies. *American Journal of Physiology-Endocrinology and Metabolism*. 2007;293(6):E1663-E1669. doi:10.1152/ajpendo.00590.2006
3. Rider OJ, Francis JM, Ali MK, et al. Effects of catecholamine stress on diastolic function and myocardial energetics in obesity. *Circulation*. 2012;125(12):1511-1519. doi:10.1161/CIRCULATIONAHA.111.069518
4. Valkovič L, Chmelík M, Kršňák M. In-vivo 31P-MRS of skeletal muscle and liver: A way for non-invasive assessment of their metabolism. *Analytical Biochemistry*. 2017;529:193-215. doi:10.1016/j.ab.2017.01.018
5. Klomp DWJ, Bank BL van de, Raaijmakers A, et al. 31P MRSI and 1H MRS at 7 T: initial results in human breast cancer. *NMR in Biomedicine*. 2011;24(10):1337-1342. doi:10.1002/nbm.1696
6. van der Kemp WJ, Stehouwer BL, Luijten PR, van den Bosch MA, Klomp DW. Detection of alterations in membrane metabolism during neoadjuvant chemotherapy in patients with breast cancer using phosphorus magnetic resonance spectroscopy at 7 Tesla. *SpringerPlus*. 2014;3(1):634. doi:10.1186/2193-1801-3-634
7. Purvis LAB, Clarke WT, Valkovič L, et al. Phosphodiester content measured in human liver by in vivo 31 P MR spectroscopy at 7 tesla. *Magn Reson Med*. 2017;78(6):2095-2105. doi:10.1002/mrm.26635
8. van der Kemp WJM, Boer VO, Luijten PR, Stehouwer BL, Veldhuis WB, Klomp DWJ. Adiabatic multi-echo 31P spectroscopic imaging (AMESING) at 7 T for the measurement of transverse relaxation times and regaining of sensitivity in tissues with short T2* values. *NMR Biomed*. 2013;26(10):1299-1307. doi:10.1002/nbm.2952
9. Negendank W. Studies of human tumors by MRS: A review. *NMR in Biomedicine*. 1992;5(5):303-324. doi:10.1002/nbm.1940050518
10. Aboagye EO, Bhujwalla ZM. Malignant Transformation Alters Membrane Choline Phospholipid Metabolism of Human Mammary Epithelial Cells. *Cancer Res*. 1999;59(1):80-84.
11. Glunde K, Jie C, Bhujwalla ZM. Molecular Causes of the Aberrant Choline Phospholipid Metabolism in Breast Cancer. *Cancer Res*. 2004;64(12):4270-4276. doi:10.1158/0008-5472.CAN-03-3829
12. Park JM, Park JH. Human in-vivo 31P MR Spectroscopy of Benign and Malignant Breast Tumors. *Korean Journal of Radiology*. 2001;2(2):80. doi:10.3348/kjr.2001.2.2.80
13. Runge JH, van der Kemp WJM, Klomp DWJ, Luijten PR, Nederveen AJ, Stoker J. 2D AMESING multi-echo 31P-MRSI of the liver at 7T allows transverse relaxation assessment and T2-weighted averaging for improved SNR. *Magnetic Resonance Imaging*. 2016;34(2):219-226. doi:10.1016/j.mri.2015.10.018
14. Steen RG. Response of Solid Tumors to Chemotherapy Monitored by in Vivo 31P Nuclear Magnetic Resonance Spectroscopy: A Review. *Cancer Res*. 1989;49(15):4075-4085.
15. Ng TC, Grundfest S, Vijayakumar S, et al. Therapeutic response of breast carcinoma monitored by 31P MRS in situ. *Magnetic Resonance in Medicine*. 1989;10(1):125-134. doi:10.1002/mrm.1910100112
16. Semmler W, Gademann G, Bachert-Baumann P, Zabel HJ, Lorenz WJ, van Kaick G. Monitoring human tumor response to therapy by means of P-31 MR spectroscopy. *Radiology*. 1988;166(2):533-539. doi:10.1148/radiology.166.2.3336731

17. Kan HE, Klomp DWJ, Wong CS, et al. In vivo 31P MRS detection of an alkaline inorganic phosphate pool with short T1 in human resting skeletal muscle. *NMR Biomed*. 2010;23(8). doi:10.1002/nbm.1517
18. van der Kemp WJM, van der Velden TA, Schmitz AM, et al. Shortening of apparent transverse relaxation time of inorganic phosphate as a breast cancer biomarker. *NMR Biomed*. October 2018:e4011. doi:10.1002/nbm.4011
19. van der Kemp WJM, Klomp DWJ, Wijnen JP. 31P T2s of phosphomonoesters, phosphodiesters, and inorganic phosphate in the human brain at 7T. *Magnetic Resonance in Medicine*. 80(1):29-35. doi:10.1002/mrm.27026
20. Löring J, van der Kemp WJM van der, Almujayyaz S, van Oorschot JWM, Luijten PR, Klomp DWJ. Whole-body radiofrequency coil for (31) P MRSI at 7 T. *NMR Biomed*. 2016;29(6):709-720. doi:10.1002/nbm.3517
21. Raaijmakers AJE, Italiaander M, Voogt IJ, et al. The fractionated dipole antenna: A new antenna for body imaging at 7 Tesla. *Magn Reson Med*. 2016;75(3):1366-1374. doi:10.1002/mrm.25596
22. Pohmann R, von Kienlin M, Haase A. Theoretical Evaluation and Comparison of Fast Chemical Shift Imaging Methods. *Journal of Magnetic Resonance*. 1997;129(2):145-160. doi:10.1006/jmre.1997.1245
23. Chmelik M, Považan M, Krššák M, et al. In vivo 31P magnetic resonance spectroscopy of the human liver at 7 T: an initial experience. *NMR in Biomedicine*. 2014;27(4):478-485. doi:10.1002/nbm.3084
24. Bogner W, Chmelik M, Schmid AI, Moser E, Trattnig S, Gruber S. Assessment of (31)P relaxation times in the human calf muscle: a comparison between 3 T and 7 T in vivo. *Magn Reson Med*. 2009;62(3):574-582. doi:10.1002/mrm.22057
25. Ren J, Sherry AD, Malloy CR. 31P-MRS of Healthy Human Brain: ATP synthesis, Metabolite Concentrations, pH, and T1 Relaxation Times. *NMR Biomed*. 2015;28(11):1455-1462. doi:10.1002/nbm.3384
26. Cheng W, Ping Y, Zhang Y, Chuang K-H, Liu Y. Magnetic Resonance Imaging (MRI) Contrast Agents for Tumor Diagnosis. Journal of Healthcare Engineering. doi:10.1260/2040-2295.4.1.23
27. Chung WJ, Chung HW, Shin MJ, et al. MRI to differentiate benign from malignant soft-tissue tumours of the extremities: a simplified systematic imaging approach using depth, size and heterogeneity of signal intensity. *Br J Radiol*. 2012;85(1018):e831-e836. doi:10.1259/bjr/27487871
28. Valkovič L, Dragonu I, Almujayyaz S, et al. Using a whole-body 31P birdcage transmit coil and 16-element receive array for human cardiac metabolic imaging at 7T. *PLoS ONE*. 2017;12(10):e0187153. doi:10.1371/journal.pone.0187153
29. Rodgers CT, Robson MD. Receive array magnetic resonance spectroscopy: Whitened singular value decomposition (WSVD) gives optimal Bayesian solution. *Magn Reson Med*. 2010;63(4):881-891. doi:10.1002/mrm.22230
30. Barmet C, Zanche ND, Pruessmann KP. Spatiotemporal magnetic field monitoring for MR. *Magnetic Resonance in Medicine*. 2008;60(1):187-197. doi:10.1002/mrm.21603
31. Boer VO, van de Bank BL, van Vliet G, Luijten PR, Klomp DWJ. Direct B0 field monitoring and real-time B0 field updating in the human breast at 7 Tesla. *Magn Reson Med*. 2012;67(2):586-591. doi:10.1002/mrm.23272
32. Dietrich BE, Brunner DO, Wilm BJ, et al. A field camera for MR sequence monitoring and system analysis. *Magn Reson Med*. 2016;75(4):1831-1840. doi:10.1002/mrm.25770

Chapter 5

CSIgui: an open-source view and processing tool for multi-dimensional MRSI data in MATLAB

Quincy (Q.) van Houtum

Wybe (J.M.) van der Kemp

Dennis (W.J.) Klomp

Zenodo 2020

Keywords: MATLAB, Analysis, Processing, GUI, MRS data

Introduction

MR Spectroscopy (MRS) allows for non-invasive detection of all nuclei with a non-zero spin in the human body. Most sensitive is ^{1}H MRS with the highest gyromagnetic ratio (γ_{1H}: 42.58 Mhz T^{-1}) and high natural abundance compared to other nuclei. Recent advances in producing homogenous RF transmit (Tx) fields at ultra-high magnetic fields (>7 tesla), i.e. the implementation of a birdcage body coil for X-nuclei transmit(Tx), in combination with an increasing number of RF receiver (Rx) coils made whole body MRS imaging of the less sensitive nuclei phosphorus (^{31}P), sodium (^{23}Na), deuterium (^{2}H) and more feasible *in vivo* [1–3].

The number of receiver channels (Rx) is increased to acquire significant signal to noise ratio (SNR) for processing and ultimately clinical relevance [4,5]. In addition, arger fields of view are possible with the new transmit body coils which allow more homogeneous transmit fields (B_1^+) [6,7]. This consequently increases the dimensionality of the spectroscopy data and current strategies which aim more and more for MR spectroscopic imaging (MRSI) further increase the acquired information density. As current MR systems cannot process this additional data stream, data processing must be done using raw data formats instead of common data formats such as dicom or spar and sdat.

Therefore, a research friendly tool to easily view multi-dimensional X-nuclei spectroscopy data and to analyze MRSI data with multiple RF channels, many voxels (due to the increased field of view), numerous sample averages and more.

CSIgui (Chemical shift imaging graphical user interface) development started as a necessity to visualize and analyse multi-dimensional MRSI data in MATLAB (The Mathworks Inc., Natick, MA). However, spectroscopy data is difficult to interpret without proper spatial localization of the voxels in MR image space. To allow proper localization a method to merge MRI data into MRSI space was added. This development continued and multiple conventional spectroscopy processing functions were added, creating a backbone for raw MRS data processing. It now supports single- and multi- dimensional data, can import different file types, process raw data and enables specific MRS processing tasks on individual spectra and bulk data.

Download and Installation

The current CSIgui version is frozen and archived on GitHub and a published release accessible via Zenodo. ("github.com/Sugocy/CSIgui/releases/tag/vThesis" and "doi.org/10.5281/zenodo.3669640").

Installation

Navigate to the CSIgui root directory in MATLAB and run *"CSIgui.m"*, either via MATLAB's command window or current folder window. The application will automatically add itself to the MATLAB search path, enabling global use in MATLAB by calling CSIgui.

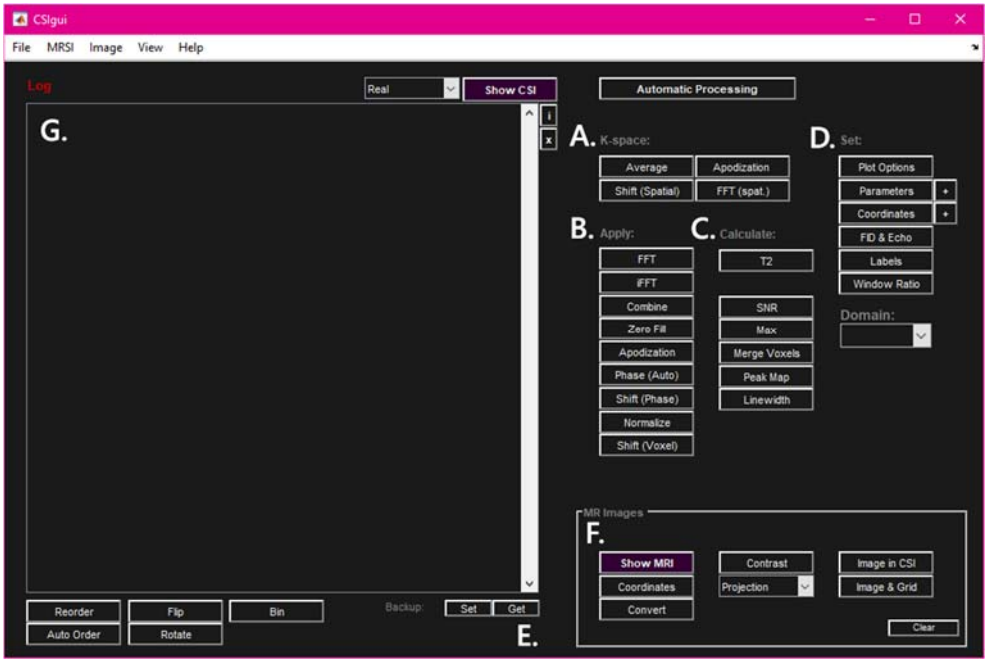

Figure 1. The main window of CSIgui with the different sections which are labelled with a letter in this figure. **(A. – C.)** The k-space, apply and calculate section that allows processing of MRS k-space data, applying processing functions to spectroscopy data or calculating values from the MRS data. **(D.)** A specific part of the GUI to set parameters and other information which is lacking in general raw data headers. **(E.)** The grey square shows MRI specific options such as viewing loaded images and converting MR images to spatial MRSI space. **(F.)** General data manipulation options are found in this section including creating a backup of current MRS data, rotating the MRS data array and changing the order of the data dimensions. **(G.)** List window that shows information loaded data and the logs of all operations in CSIgui.

Content

In the root directory the following files and directory are expected: "CSIgui.m", containing the core code of the GUI "CSIgui.fig", License, README.md and directory "Files".

Methods

After installation and running the command 'CSIgui.m' CSIgui starts with the user interface screen shown in figure 1. A detailed explanation of its algorithms is defined:

Load Data

Loading data in CSIgui is possible using two of the following methods. The first is within the GUI by selecting "*File* > *Open*" in the top menu and the second method is accessed by using specific input arguments in MATLAB scripts or the Command window. More in-depth details on MRS loading data can be found in the scripts "csi_loadData.m", "csi_loadList.m", "csi_readSDAT.m", "csi_readSPAR.m" and csi_readText in the CSIgui root directory "Files".

Supported data types:

.data/.list:	raw data stored in a two column float32 format and the Gyroscan parameter list file as exported with Gyroscan release 5.
.spar/.sdat:	raw data stored as VAX-CPX float and the Gyroscan parameter file as exported with Gyroscan release 5.
*.dcm:	Images stored as Philips DICOM v4.2.
.par/.rec:	Images stored as Philips PAR/REC v4.2.
*.txt	Spectroscopy data stored as two columns; the real and imaginary parts.

Input arguments

CSIgui can be called as a regular function in MATLAB and supports multiple input variables. This allows integration of CSIgui with other data processing scripts coded by the user to easily view multidimensional spectral data or to apply specific processing steps. Examples are shown below.

>>> CSIgui('label' , var);

Supported input labels and corresponding variables

Label	***Synonym***	**Input**
data		structure output from csi_loadData() for loading list/data files
list		structure output from csi_loadList() or csi_loadData()
csi	*spec* | *mrs*	array of any size with spectra or fids.
labels		labels per dimension of the data array
filepath	*fp*	file path to spectroscopy data file as cell* – *.spar/sdat | *.list/data | *.mat
filepathi	*fpi*	file path to an image data file as cell* – *.dcm | *.par/rec

NB. *The file paths string variables have to be passed to CSIgui as a cell-variable; {"D:\Example"}. See examples below.

Examples:

```
>>>  fp = "D:\Data\MyData\raw_001.data";
>>>  CSIgui(  { fp } ,  "filepath" );

>>>  fp = "D:\Data\MyData\raw_001.data";
>>>  fpi = "D:\Data\MyData\FFE.dcm";
>>>  CSIgui( { fp } , "filepath" , { fp i}, "filepathi");

>>>  load( "someSpectra.mat", "array" );
>>>  CSIgui( array, "mrs");
```

Data Indexing

Summary of data handling of both MRSI and MRI data in CSIgui: dimension indexing, array sizes and CSI-space.

MRSI Indexing

CSIgui is compatible with MRSI arrays of all sizes within the available amount of random-access memory (RAM) in MATLAB. Displaying the data is linked to dimension indexing. By default, the application expects the following dimensional indexing of the MRSI data:

Index 1:	Samples of a spectrum or free induction decay (FID);
Index 2/3:	The X (width) and Y (height) index of multi or single dimensional data.
Index >4:	Slice or Z index of multi or single dimensional data.

To edit the order of the dimensions of the MRSI data, the buttons "*Reorder*" or "*Auto Reorder*" can be used. For more details, see the "Processing" section below.

Example:
MRSI array of size: 1024 x 4 x 5 x 3 x 6;

Each spectrum of 1024 datapoints will be shown in a 2D plot i.e. a slice, of size 4x5 with available slice selections of 1 to 3 and 1 to 6.

MRI Indexing
CSIgui expects the width and height of the image array to be the row and column index respectively e.g. the first and second index. Higher dimensions of these 2D arrays are handled as separate slices. Loading image data using the application itself is advised if merging of both MRSI and MRI data is requested.

Display Data

Both the MRS and MRI data can be visualized separately or merged.

View MRSI
Pressing the "*Show CSI*" button will open a 2D plot of the MRSI data. The second and third dimension of the MRSI data set will be shown as the X (width) and Y (height) in this plot. Other higher dimensions are accessible for display through a small automatically launched window called "*CSIgui display panel*".

A single spectrum can be viewed by selecting a spectrum of interest in the CSIgui 2D plot window. This opens a 1D plot of the clicked spectrum and allows separate processing of this displayed spectrum. The selected spectrum is highlighted in the 2D plot window. If correct x-axis scaling is required, enter frequency information by pressing the "*Frequency*" button in the "*set"* section of CSIgui.

View MRI
Pressing the "Show IMG" button will open up MRgui2, a separate application. This application displays multiple image types and enables scrolling through all images in a single image-type array.

Merging MRSI and MRI
Tested and validated on transverse, sagittal and coronal MRI data sets in combination with transverse MRSI data sets only.

To merge the MRI data to MRSI space, coordinate information of both data sets is required. Pressing "*convert*" at the IMG options of CSIgui will calculate the coordinates of the images, calculate the coordinates of the MRSI data set and convert the images to MRSI space. Spatial information of MRSI data will be

requested if unavailable. If no image header information is in memory, required parameters will be requested too. Otherwise, the image coordinates are calculated automatically. The latter is applicable if the image data (dicom and Philips par/rec files) is loaded using CSIgui's default functions.

The desired image type for conversion must be given if multiple image types are available. Coordinate parameters can be entered separately by pressing the "*Coordinates*" button at the CSI and IMG section of CSIgui.

MRSI coordinate parameters:

Voxel size: The voxel size of each direction. For *.list/*.data files use the acquisition voxel size, not the reconstruction voxel size.

Offset: Offset of the MRSI stack.

MRI conversion parameters:

Image type: Image type such as magnitude (M), phase (P) or specific parameter maps E.g. B_0 (maps, T_1 maps) to use for conversion to MRSI space.

FFT correction: Half a voxel shift is present in any odd sized dimension of the data due to the FFT method used in MATLAB. Due to the FFT method, a half voxel shift is present. Setting this option to one (1) corrects for this offset. Default input is set to 1. Setting the option to zero (0) will disable the correction.

Calculation Data

CSIgui allows visualization of multi-dimensional calculated data as either a graph or a table.

Graph:

With respect to the x, y and z index on the second, third and fourth dimension, any additional dimensions in the MRSI data set such as averages, RF channels, echoes or other attributes are concatenated. This means every fifth dimension or above are combined to plot a line. To allow visualization of calculated data from multiple slices e.g. the z-dimension, the created figure includes tabs for each slice.

Table:

Display calculated values in tables for each available 2D plot e.g. slice. Any additional dimensions in the MRSI data set such as averages, RF channels, echoes or other attributes are concatenated in its corresponding slice table. Data or only the data selection in the visible table can be saved to a file.

Processing

Both MRSI and MRS data can be processed and analyzed by multiple available functions which are explained below. Hovering the mouse cursor over each button in CSIgui and over specific menu items shows short explanations of the available options or requirement of the functions. All options in the k-space, apply and calculate section apply to every individual spectrum in the dataset.

In addition to these multi-voxel processing functions, a single spectrum can be processed separately by opening the spectrum of interest in the CSIgui 2D plot. For more information, see below.

MRSI functions

The functions are ordered according to different sections available in CSIgui, including: Raw Data Processing, Apply, Calculate and Set.

K-SPACE

The processing options in this section are designed for file types which store raw MRSI data i.e. data stored in k-space domain.

- Average

  Data is averaged over the “aver” labelled dimension. If the label is not present, the user is asked to specify an index to average over.

- Spatial Apodization

  Apply apodization over the entire volume (each voxel in every dimension). A multi-dimensional filter window is calculated using one of the available filter window algorithms: Hamming, Hann, flat top or Blackman. The size of indexes labelled as “Kx”, “Ky” and, if 3D, “Kz” are used to define window size. If the proper labels are not present, the user is asked to specify at least two indexes. More in-depth details of the implemented algorithm can be found in the script “csi_apodization3D.m” in the CSIgui root directory “Files”.

  This function is useful if k-space is not sampled fully or to apply smoothening over the entire volume. Be aware: spatial apodization causes a significant increase in voxel size in all applicable directions [8].

- FFT (spatial)

  Fast Fourier Transform from k-space domain to spatial domain over the "Kx", "Ky" and, if present, "Kz" dimensions using the default functions in MATLAB shown in equation 1, with "data" the MRSI data either in the spatial "x" or k-space "f" domain and the dimension to apply the transform over, "index" . If the proper labels are not present, the user is asked to specify at least two indexes. In addition, the option to choose the shift method to center the zero-frequency component of the spectra is available. The default option (2, automatic) uses the circular shift function for odd sized dimensions instead of the "fftshift" and its inverse functions. Options 1 and 0 use solely the circular or Fourier shift function respectively. More in-depth details of the implemented algorithm can be found in the script "csi_rawfft.m" in the CSIgui root directory "Files".

  [1]

  if (size of k-space dimension is even)

  data(x) = …

  fftshift(*fft*(*ifftshift*(data(f), index), …

  [ ], index), index)

  elseif (size of k-space dimension is even)

  data(x) = *circshift*(data(f), -1 × *ceil*($\frac{size(\text{index})}{2}$ + 1) , index)

  end

APPLY

- FFT

  Fast Fourier Transform (forward) to convert the voxel data from time to frequency domain using default MATLAB functions shown in equation 2 with "data" the MRSI data either in the spatial "x" or frequency "f" domain. More in-depth details of the implemented algorithm can be found in the script "csi_fft.m in the CSIgui root directory "Files".

  data(f) = *fftshift*(*fft*(data(x))) [2]

- iFFT

  Inverse Fast Fourier Transform (backward) to convert the voxel data from frequency to time domain using default MATLAB functions shown in equation 3 with "data" the MRSI data either in the spatial "x" or

frequency “f” domain. More in-depth details of the implemented algorithm can be found in the script “csi_ifft.m in the CSIgui root directory “Files”.

$$data(x) = ifft(ifftshift(data(f))) \quad [3]$$

- Combine

  Combine channels from multiple RF coils using one of two available methods.

  Manual: Combine channels by summation or calculating the mean of all channels with the option to exclude specific channels.

  WSVD: Whitened singular voxel decomposition; the coils are combined using a noise weighting method [9]. A noise component is required for this algorithm to calculate a noise covariance matrix between all channels. The noise can be calculated from the positive edge of the spectrum using a noise mask which size can be set in the WSVD options window or using the noise measurements per channel which are available if a list/data file is in memory. With the latter approach the noise mask size setting is not used. For more in-depth information the user can open the script “wsvd.m” located in the “Files” directory of CSIgui repository or read the source article.

- Zerofilling

  Add trailing zeroes to data in the time domain. Target number of datapoints is requested and must be equal or greater than the actual number of datapoints. More in-depth details of the implemented algorithm can be found in the script “csi_zeroFill.m in the CSIgui root directory “Files”.

- Apodization (time domain)

  Apply 1D apodization to all voxels in the data set. The filter that will be applied to time domain data will be displayed in a new window and the user has the option to apply the filter or abort the operation. More in-depth details of the apodization algorithms can be found in the function “CSI_filterSpectra” in the main script of CSIgui.

- Phase (auto)

  Apply an automatic zeroth order phase correction using a given peak its frequency range in the spectrum. This algorithm will maximize the real part of the spectrum in the given range. More in-depth details of the implemented algorithm can be found in the script "csi_autoZeroPhase.m" in the CSIgui root directory "Files".

CALCULATE

All functions in this section apply to every individual spectrum in the dataset.

- T2

  Calculate T_2 by fitting the exponential decay function to a variable number of echoes. This function requires the echo dimension to be on the fifth index and will calculate T_2 for all voxels. The maximum signal in the spectra at the data range given by the user will be used to calculate T_2 using equation 4 with the maximum signals S, the signal amplitude A and the corresponding echo times t. The data range option allows the user to select a peak signal of interest. Results will be shown as graphs which include the maxima over all echoes e.g. the measured data, the resulting fit values, the T_2 values plus confidence intervals of the fit and the coefficient of determination (R^2). All T_2 values will be saved automatically to a *.mat file named with current date and time. Stored data includes the T_2 relaxation time values, R^2 values, amplitude of the exponential fit and the confidence intervals. More in-depth details of the implemented fitting algorithm can be found in the script "T2_exp.m" in the CSIgui root directory "Files".

$$S = Ae^{-(\frac{t}{T2})} \quad [4]$$

- SNR

  Calculate the SNR for each spectrum using a noise mask with variable size and using either the real or the magnitude part of the data using equation 5. The SNR will be calculated using the maximum signal intensity in the range specified by the user. Data can be visualized as a graph if multiple dimensions (e.g. index 5 or higher) are present or as a table.

$$\mathrm{SNR} = \frac{mean\left(max\left(real(\mathrm{spec})\right)\right)}{abs\left(std\left(spec(\mathrm{noise\ mask})\right)\right)} \quad [5]$$

NB: Use of either the real or absolute part of the spectrum in the numerator can be chosen.

- Max

  Two methods to view the maximum value at a given range of a spectrum are available. The first method calculates and displays the maximum value of each spectrum and data can be visualized as either a graph or as a table. The second method displays the maximum values of the full data set as a 3D volumetric scatter plot with size and color normalized to the largest maxima in the calculated data.

- Linewidth

  Calculate the linewidth at full width half maximum (FWHM) for each individual spectrum in the data set. Values are returned in ppm if the frequency parameters are available (See Set > Parameters). Results can be displayed as a graph or as a table and can be exported to text file. More in-depth details of the implemented algorithm to calculate a linewidth at the half hight of a signal peak can be found in the script “csi_LineWidth.m” in the CSIgui root directory “Files”.

- Normalized

  Normalize the MRS data set to either the maximum or minimum signal, a peak intensity, spectral noise or a custom value in the entire data volume or per voxel using the real part of the data.

- Shift (voxel)

  Shift the MRSI data set by a number of voxels by altering the grid coordinates or manipulating the index of the MRS data set.

SET

- Parameters

  Set the nucleus of interest, magnetic field strength, bandwidth and possible shift (in ppm) to calculate x-axis values for each spectrum with the option for unities time (s), frequency (Hz) and parts per million (ppm).

- Coordinates

  Set the voxel sizes in all applicable directions and any possible offset if the dimensional stack to calculate coordinates of for each voxel.

- FID & Echo

  Split FID and Echo data to enabling separate editing. This is specifically designed for the multi-echo spectroscopic Imaging (MESING) sequence.

- Window Ratio

  Set the 2D Plot window its size ratio equal to the voxel ratio of the MRSI data.

- Plot Options

  Set specific 2D plot options: Color scaling, Y-axis scaling and X-axis scaling. The latter allows zoom in on specific peaks in the 2D plot.

- Labels

  Change the names e.g. labels of each dimension.

MRI functions

Functions in the MRI section of the GUI are focused on merging MRI with MRSI data. MRI data can be converted to MRSI space and display contrast of these images can be managed.

- Coordinates (MRI)

  Calculate coordinates for each voxel in the image data set. If no image header information from dicom or par file is present, required parameters are requested. See Displaying data > Merging MRI and MRSI for more information.

- Convert

  Convert the MRI data to the MRSI space. This requires coordinates of both data sets and missing information will be requested automatically. If multiple image types are present, the image type of interest to convert is requested.

- Contrast

  Set display contrast of the image when displayed simultaneously with the MRSI data.

- Image in CSI

  Display all the images used for the currently viewed CSI array. Only works if MR images are converted to CSI space.

- Image & Grid

  Create one figure with the 2D CSI voxel grid and the images. No spectra plotted. Solely for displaying and localization.

Individual spectrum

Individual spectra can be viewed by clicking on a voxel in the 2D plot window of CSIgui. A separate plot window showing the 1D data and a 1D options panel will open. Multiple processing options for the 1D data are available and explained here:

- Phasing

  Manual: Apply manual phase correction in a separate GUI.

  Automatic: Automatically try to maximize the real part of the spectrum at a given interval or position. The interval must be given in sample points.

  Phase all: Manually phase the shown spectrum and apply the calculated correction to all other spectra in the data set.

  The GUI for applying manual phase corrections can be used separately from CSIgui using the script “csi_PhaseCorrectionGUI.m”

- FFT

  Fast Fourier Transform (forward) to convert the spectrum from the time domain to the frequency domain using equation 2.

- iFFT

  Inverse Fast Fourier Transform (backward) to convert the spectrum from the frequency to the time domain using equation 3.

- Apodization

  Apply apodization to the data using an available 1D filter. The filter that will be applied to time domain data will be displayed in a new window and the user has the option to apply the filter or abort operation. More in-depth details of the apodization algorithms can be found in the function “CSI_filterSpectra” in the main script of CSIgui.

- Zero Fill

  Add trailing zeroes to data in the time domain. Target number of datapoints is requested and must be equal or greater than the actual number of datapoints. More in-depth details of the implemented

algorithm can be found in the script “csi_zeroFill.m in the CSIgui root directory “Files”.

- Linewidth

  Calculate linewidth at FWHM of a specific peak of interest or in all peaks found automatically. Will show processing results of each peak in separate windows.

- SNR

  Calculate the SNR of the spectrum. SNR value is displayed in the MRS information box in CSIgui.

- Data Display

  Set the unit of the displayed x-axis and the data type to be shown.

- Replace voxel

  Replace the spectrum in the dimensional data set with the processed single spectrum.

- Export

  Export the displayed spectrum to file; sdat/spar, text and mat-file.

Merging Voxels

Merge Voxels opens a separate window with the images and MRSI voxel grid as an overlay for each index in the (k)z-dimension. Select voxels of interest and press save to save data to file or merge to open the merge menu.

Merge menu:

- Set SNR filter on to include and/or exclude a peak at a specific SNR level.
- Set SNR weighting to weight the averaging to peak of interest SNR.
- Apply frequency alignment prior to averaging by shifting each spectrum using the maximum 1D cross-correlation between all peaks and the spectrum with the maximum signal.

Exporting Data

Data

Exporting MRSI data can be found in the MRSI menu in CSIgui. Supported export file types are sdat/spar, text and mat-files. Specific parameters will be requested for spar and sdat files. Saving the data as a mat-file allows the user to continue working in CSIgui by loading the mat-file in question when needed. In addition, the exported data in text format is compatible with JMRUI v4 and higher.

Figures

A displayed 2D MRS plot from CSIgui can be saved to file using the menubar options MRSI > Export > Figure. In addition, CSIgui can automatically loop through all slice and attribute indexes and save each 2D MRSI plot as a separate image file.

GUI Appearance

CSIgui has a day and night mode with the latter being the default setting. Change the theme in the menu bar in View > Theme. To customize the color layout, go to View > Set Custom Color and enable Custom color in View > Theme.

Results

A few examples are shown that highlight the functionality and potential of CSIgui (fig. 1-5). The tool allows processing, visualization and localization of raw 3D CSI data as acquired in a ^{31}P loading phantom in combination with MR images (fig. 1). In addition, it is possible to view the data in between all processing steps which are explained. Application of CSIgui to heart and liver ^{31}P spectroscopic imaging data are shown in figure 2, where a coronal and transverse slice of two *in vivo* 3D CSI raw data sets, both acquired with a 16-channel receiver array can be seen. The different RF channels are combined using the WSVD algorithm implemented in CSIgui. Merging MRSI and MRI data allows localization of tissue specific voxels in the heart, liver and skeletal muscle including discrimination of different metabolite peaks (fig. 2B-C and 2E-F).

Another example of CSIgui its functionality is the T_2 quantification of inorganic phosphate in a sphere embedded in a large body-size phantom seen in figure 4. The presented data serves a validation purpose for a multi-echo spectroscopic imaging protocol [6]. The displayed fit results are generated using CSIgui including the image and individual spectra of the FID and echoes. This functionality is also used for *in vivo* T_2 quantification of phosphocreatine in the gluteus maximus (fig. 5). It shows the use of the image display function in CSIgui in combination with the T_2 calculation output.

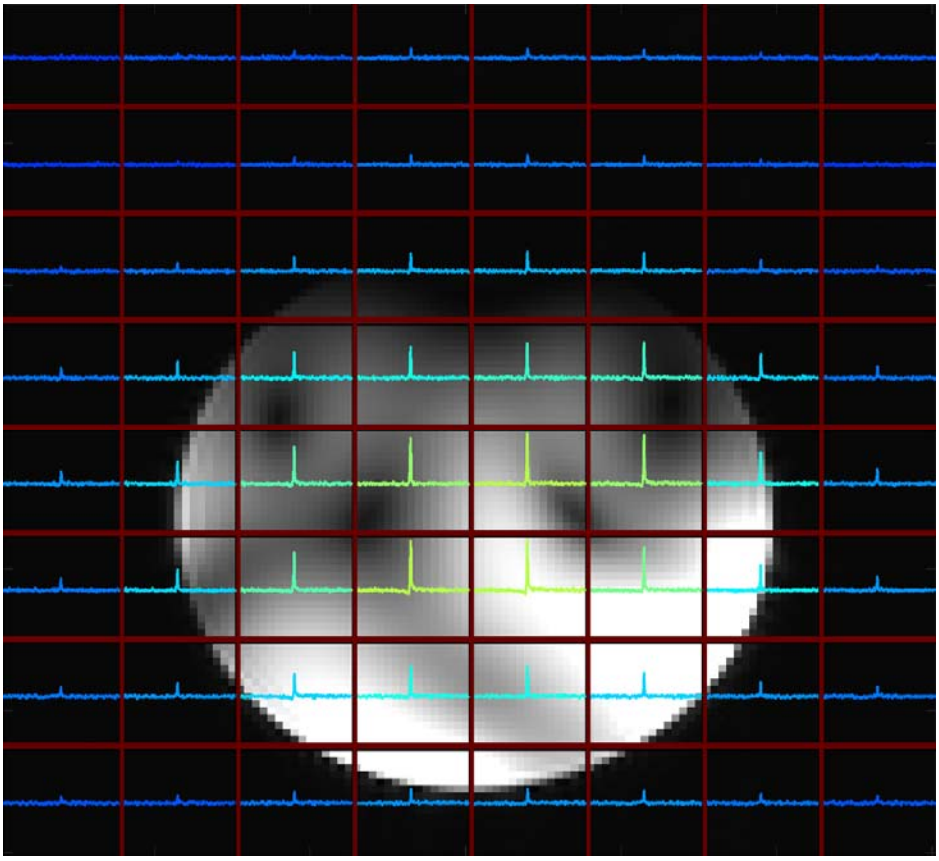

Figure 2. The 2D plot window of CSIgui showing a single slice from a 3D MRSI data set with a converted MR image in the background. The data were acquired in a 31P loading phantom containing a solution with a single 31P metabolite using a 3D CSI protocol in combination with a 1H/31P dual transceiver coil in quadrature mode. Using CSIgui, raw data were loaded and indexed e.g. shaped to k-space. The data was averaged over the number of sampled averages dimension and spatially filtered using a 3D hamming window before inverse Fourier transform of k-space to the spatial domain. The resulting FIDs from all voxels were apodized in the time domain using a Gaussian filter in a single operation. Zeroth order phase correction were applied automatically after Fourier transform to the frequency domain. The MRSI parameter file retrieved from the MR-system was loaded and frequency plus spatial parameters were set. This allowed converting the MR images to MRSI space and plot the resulting spectra on top of the calculated images.

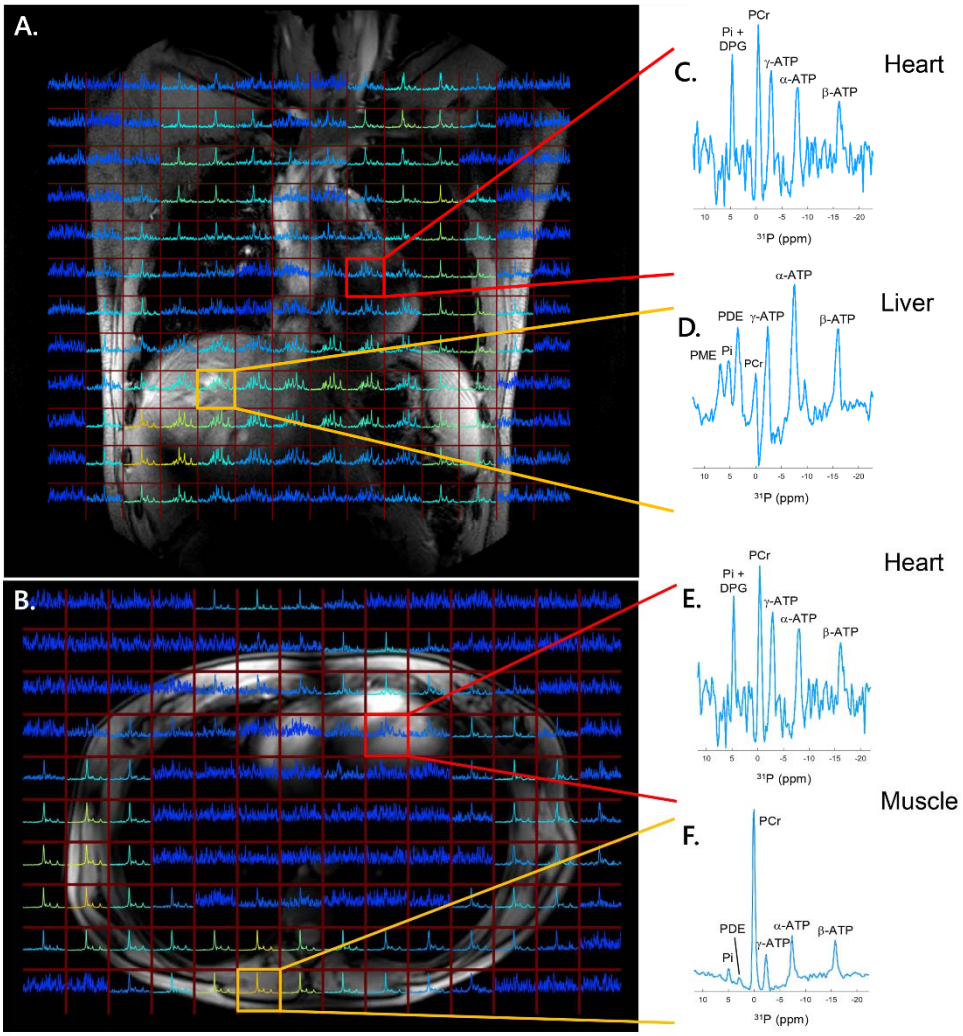

Figure 3. Collage of two *in vivo* 31P MRSI data sets of the heart and liver acquired with a 16-channel setup at 7 tesla and processed with CSIgui. **(A - B.)** A coronal and transverse MR image with a slice from the 3D CSI data set displayed on top. The heart, liver and skeletal muscle are visualized with the two red and two yellow squares respectively. The colors of the spectra are scaled to the maximum signal amplitude in the data volume with a yellow, high signal to blue, low signal color gradient. The y-axis is scaled to the maximum per voxel. MR images acquired during the same session are converted to MRSI space and plotted with in the background of the MRSI data. **(C - F.)** Four individual spectra from the two 3D data sets showing spectra in the heart, liver, and skeletal muscle. Different metabolites can be discriminated after processing and localization and show tissue specific signal intensities.

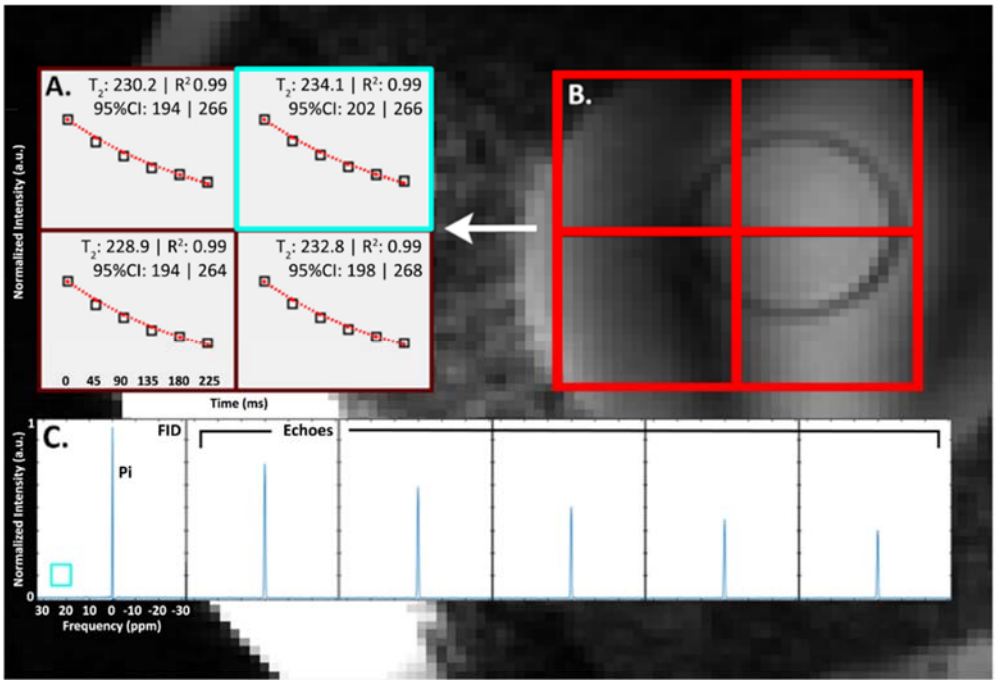

Figure 4. Multi-echo spectroscopic imaging data processed and presented for validation using CSIgui (Copied from chapter 4: "Low SAR 31P (multi-echo) spectroscopic imaging using a ^{31}P whole body birdcage coil at 7T"). **A)** *In vitro* T_2 measurement of inorganic phosphate in a body-sized phantom using a multi-echo spectral imaging sequence for each voxel in **B)** the red grid on the localizer image of the sphere which contains the metabolite. The normalized maximum peak value for the FID and each echo plus the corresponding fit are denoted as black squares and a red dotted line respectively. Both the line color and marker appearance were edited using CSIgui. Average T_2 over all four voxels for the Pi contained in the small sphere was 232 ± 35 ms. **C)** The spectra of the FID and five echoes for the single voxel highlighted by the blue square, acquired using a ^{31}P dual coil receiver in combination with a ^{31}P body coil. The frequency scaling shown for the x-axis of the FID is equal for all other echoes.

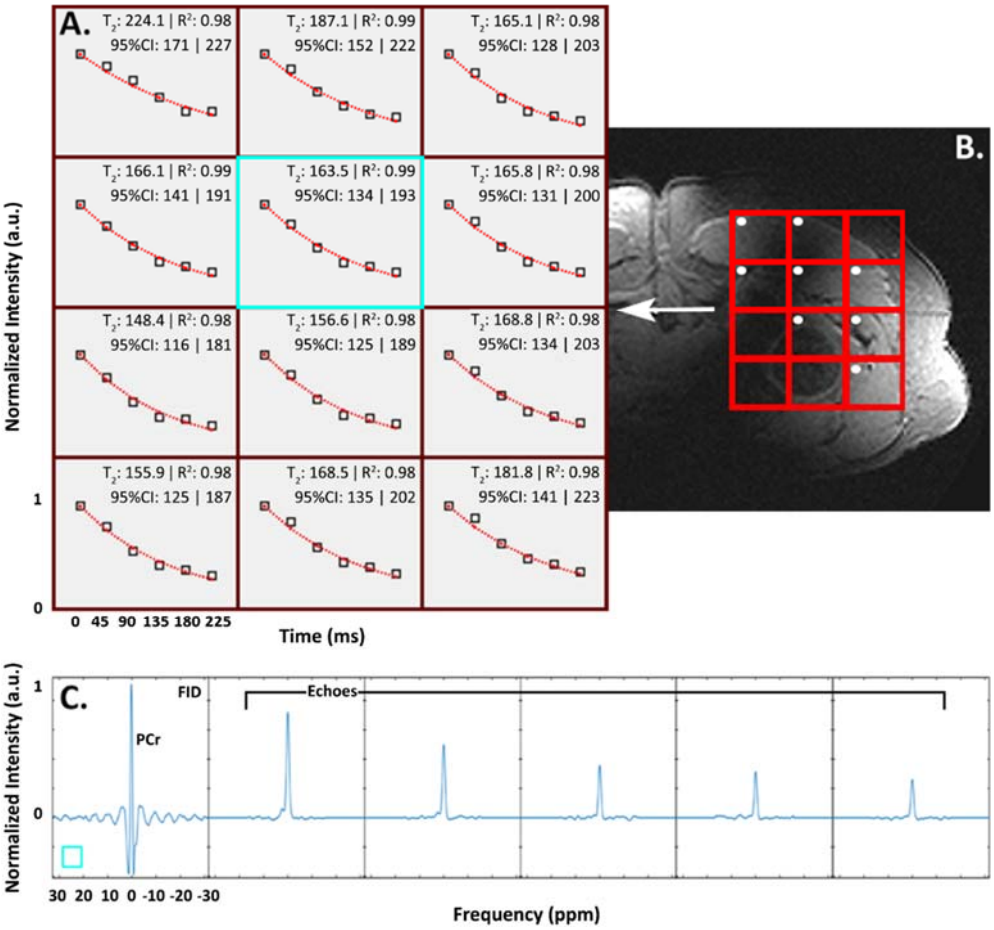

Figure. 5. *In vivo* multi-echo spectroscopic imaging data processed and presented using CSIgui. ((Copied from chapter 4: "Low SAR 31P (multi-echo) spectroscopic imaging using a ^{31}P whole body birdcage coil at 7T"). **A)** *In vivo* T_2 fits of phosphocreatine using multi-echo spectroscopic imaging data from a single volunteer in voxels corresponding to the gluteal muscles as shown by the red grid in **B)** the T_1-weighted localizer image. Normalized maximum peak value for the FID and each echo are denoted as open squares and the red dotted lines represent the fit which are all set using CSIgui options. Echo times applicable to all voxels are shown in the bottom left. Average T_2 from all voxels with high muscle tissue content, denoted by the white dots, was 177 ± 35 ms. **C)** Spectra of the FID and five echoes for the voxel highlighted by the blue square, acquired using a ^{31}P dual coil receiver in combination with a ^{31}P body coil. The frequency scaling shown for the x-axis of the FID is equal for all other echoes.

Discussion

Magnetic resonance spectroscopy (MRS) focusses on physiological changes in the body rather than monitoring morphological changes using imaging modalities such as computed tomography (CT) and magnetic resonance imaging (MRI). Technological advances at ultra-high-field MRS (7T and higher) create opportunities to better monitor and therefore investigate chemical processes in detail such as the energy metabolism, phospholipid metabolism but also the acidity of the environment. However, the new data generated is not easily processed by currently available software. The default MR console software cannot process the increased number of dimensions and those processing steps are not fully accessible. Visualization of all the additional data dimensions such as RF channels, averages, cardiac phases, echoes and more is cumbersome with the current available tools such as 3DiCSI (Hatch Center for MR research, Columbia University), which is discontinued and jMRUI which is not suitable for merging MRSI and MRI data or multi-channel data [10]. New data structures and novel processing of advanced MRSI is either slow or even impossible to view as the software code of common software packages is not easily changed or its source code not accessible.

To overcome this issue, CSIgui was created in MATLAB. MATLAB is a higher programming language and commonly used in the research environment for image and data processing. The large default algorithm library saves time and eases scripting, however for visualization of these data sets specific coding is required. CSIgui allows visualization and processing of the multi-dimensional MR spectroscopic data, with all code available to the user to understand algorithms or change it to their preferences. The core methodology of the GUI code is documented and in combination with available example code users can easily add their own functionality to the tool. This allows development of the tool by peers in the field. In addition, the tool enables exporting data to data formats which are used in software such as jMRUI (MRUI Consortium, http://www.jmrui.eu) and LCModel (LCModel, http://www.s-provencher.com/lcm-test.shtml).

One general limitation of CSIgui is the lack of support for data formats from (N)MR vendors other than Philips and Gyroscan. This can be solved by creating an addition to the code using example code in the “CSIgui.m“ file.

A learning curve is present in CSIgui especially if the user is not experienced with processing MRS data. For instance, the data domain is only tracked by the GUI when the user loads data using CSIgui. Otherwise the user must be aware when applying specific operations to the data such as 1D apodization or zeroth order phasing. In addition, converting MR images to MRSI space is also a complex step to verify by the user if specific artefacts such as fold over are present. However, the automatic processing option guides the user to apply each processing step in a correct order.

Conclusion

The default MR software is currently unable to process the additional data streams that come with multichannel data. CSIgui allows processing and analysis of the large MRSI data sets in a common research-oriented programming language, MATLAB. This allows the tool to be flexible in use with custom add-ons, custom processing code in MATLAB and in combination with other NMR tools used in the field.

References

1. Chmelik M, Považan M, Kršňák M, Gruber S, Tkačov M, Trattnig S, Bogner W. In vivo 31P magnetic resonance spectroscopy of the human liver at 7 T: an initial experience. *NMR in Biomedicine*. 2014;27(4):478-485. doi:10.1002/nbm.3084
2. Feyter HMD, Behar KL, Corbin ZA, Fulbright RK, Brown PB, McIntyre S, Nixon TW, Rothman DL, et al. Deuterium metabolic imaging (DMI) for MRI-based 3D mapping of metabolism in vivo. *Science Advances*. 2018;4(8):eaat7314. doi:10.1126/sciadv.aat7314
3. Bangerter NK, Kaggie JD, Taylor MD, Hadley JR. Sodium MRI radiofrequency coils for body imaging. *NMR in Biomedicine*. 2016;29(2):107-118. doi:10.1002/nbm.3392
4. Valkovič L, Dragonu I, Almujayyaz S, Batzakis A, Young LAJ, Purvis LAB, Clarke WT, Wichmann T, et al. Using a whole-body 31P birdcage transmit coil and 16-element receive array for human cardiac metabolic imaging at 7T. *PLoS ONE*. 2017;12(10):e0187153. doi:10.1371/journal.pone.0187153
5. van Houtum Q, Mohamed Hoesein FAA, Verhoeff JJC, van Rossum PSN, van Lindert ASR, van der Velden TA, van der Kemp WJM, Klomp DWJ, et al. Feasibility of 31P spectroscopic imaging at 7 T in lung carcinoma patients. *NMR in Biomedicine*. n/a(n/a):e4204. doi:10.1002/nbm.4204
6. van Houtum Q, Welting D, Gosselink WJM, Klomp DWJ, Arteaga de Castro CS, van der Kemp WJM. Low SAR 31P (multi-echo) spectroscopic imaging using an integrated whole-body transmit coil at 7T. *NMR in Biomedicine*. 0(0):e4178. doi:10.1002/nbm.4178
7. Löring J, van der Kemp WJM, Almujayyaz S, van Oorschot JWM, Luijten PR, Klomp DWJ. Whole-body radiofrequency coil for (31) P MRSI at 7 T. *NMR Biomed*. 2016;29(6):709-720. doi:10.1002/nbm.3517
8. Pohmann R, Kienlin M von. Accurate phosphorus metabolite images of the human heart by 3D acquisition-weighted CSI. *Magnetic Resonance in Medicine*. 2001;45(5):817-826. doi:10.1002/mrm.1110
9. Rodgers CT, Robson MD. Receive array magnetic resonance spectroscopy: Whitened singular value decomposition (WSVD) gives optimal Bayesian solution. *Magn Reson Med*. 2010;63(4):881-891. doi:10.1002/mrm.22230
10. Qui Z. NMR Information Server - News - 3DiCSI. http://www.spincore.com/nmrinfo/3DiCSI_1.shtml. Accessed January 17, 2020.

Chapter 6

Feasibility of ^{31}P spectroscopic imaging at 7T in lung carcinoma patients

Quincy (Q.) van Houtum

Firdaus (F.A.A.) Mohamed Hoesein

Joost (J.J.C.) Verhoeff

Peter (P.S.N.) van Rossum

Anne (A.S.R.) van Lindert

Tijl (T.A.) van der Velden

Wybe (W.J.M.) van der Kemp

Dennis (D.W.J.) Klomp

Catalina (C.S.) Arteaga de Castro

NMR in Biomedicine 2019

Keywords: ^{31}P MR spectroscopic imaging, response monitoring, lung carcinoma, X-nuclei MRS, *in vivo* application.

Abstract

Introduction & methods: Currently, it is difficult to predict effective therapy response to molecular therapies for the treatment of lung cancer based solely on anatomical images. ^{31}P MR spectroscopic imaging could provide as a non-invasive method to monitor potential biomarkers for early therapy evaluation, a necessity to improve personalized care and reduce cost. However, surface coils limit the imaging volume in conventional ^{31}P MRSI. High-energetic adiabatic RF pulses are required to achieve flip angle homogeneity but lead to high SAR. Birdcage coils permit use of conventional amplitude modulated pulses, even over large FOV, potentially decreasing overall SAR massively. Here, we investigate the feasibility of 3D ^{31}P MRSI at 7T in lung carcinoma patients using an integrated ^{31}P birdcage body coil in combination with either a dual-coil or a 16-channel receiver.

Results: Simulations showed a maximum decrease in SNR per unit of time of 8% for flip angle deviations in short TR low flip-angle excitation 3D CSI. The minimal SNR loss allowed for fast 3D CSI without time-consuming calibration steps (>10:00 min.). ^{31}P spectra from four lung carcinoma patients were acquired within 29:00 minutes and with high SNR using both receivers. The latter allowed discrimination of individual phosphodiesters, inorganic phosphate, phosphocreatine and ATP. The receiver array allowed for an increased FOV compared to the dual-coil receiver.

Discussion: 3D ^{31}P-CSI were acquired successfully in four lung carcinoma patients using the integrated ^{31}P body coil at ultra-high field. The increased spectral resolution at 7T allowed differentiation of multiple ^{31}P metabolites related to phospholipid and energy metabolism. Simulations provide motivation to exclude ^{31}P B_1 calibrations, potentially decreasing total scan duration. Employing large receiver arrays improves the field of view allowing for full organ coverage. ^{31}P MRSI is feasible in lung carcinoma patients and has potential as a non-invasive method for monitoring personalized therapy response in lung tumors.

Abbreviations: Phosphorus **(^{31}P)**, Magnetic Resonance Spectroscopic Imaging **(MRSI)**, Adenosine triphosphate **(ATP)**, Chemical Shift Imaging **(CSI)**, Free induction decay **(FID)**, Glycerophosphoethanolamine **(GPE)** Glycerophosphocholine **(GPC)**, Nicotinamide adenine dinucleotide phosphate **(NADPH)**, Phosphocreatine **(PCr)**, Phosphocholine **(PC)**, Phosphodiesters **(PDE)**, Phosphoethanolamine **(PE)**, Inorganic Phosphate **(Pi)**, Phosphomonoesters **(PME)**, Receiver **(Rx),** specific absorption rate **(SAR)**, repetition time **(TR)**, uridine diphosphoglucose **(UDPG)**

Introduction

In recent years, many new molecular therapies, such as immunotherapy, have been introduced for the treatment of lung cancer [1]. Tumor cells generally use antigens to mask themselves from the immune system and immunotherapy exploits this mechanism by administering antibodies which specifically target tumor antigens. This labels the cell which allows it to be recognized by the own defense mechanisms of the body. The immune system responds by inhibiting or attacking the tumor cells, resulting in stalled tumor growth not necessarily accompanied by a decrease of tumor volume on imaging modalities [2].

Currently, it is difficult to predict which patients show an effective response to immunotherapy based on anatomical images like computed tomography only. Although a promising new treatment strategy for non-small cell lung carcinoma, immunotherapy is expensive and severe drug side effects are observed accompanied by an apparent decrease in quality of life. Therefore, there is an unmet need for a non-invasive method that can be used to predict tumor metabolic response which is crucial for early therapy effect evaluation. By adjusting the therapy strategy accordingly, such a tool would allow for more personalized curative care with less side effects, and reduced costs.

A recent study in breast cancer showed that changes in the phospholipid metabolism in responsive tumors can be detected after a single chemotherapy session using 31-phosphorous (^{31}P) magnetic resonance spectroscopic imaging (MRSI) [3,4]. ^{31}P MRSI can detect the phospholipid and energy metabolites, which provides possibilities to monitor tissue metabolism non-invasively during treatment. Inorganic phosphate (Pi), phosphocreatine (PCr) and ATP (with the α-, β- and γ- resonances) allow assessment of the energy metabolism and the phosphomonoesters (PME) and phosphodiesters (PDE) provide insight into the phospholipid metabolism [4–7]. Enhanced ratios of phosphocholine (PC) to glycerophosphocholine (GPC) and phosphoethanolamine (PE) to glycerophosphoethanolamine (GPE), are frequently observed in tumor tissue and correlated with proliferation [7–12]. Another study in breast cancer demonstrated the feasibility of the phospholipid metabolism as biomarker for therapy follow-up and additionally reported shortening of the transverse relaxation time of Pi as a biomarker [4,8,13]. As the physiological changes are present before any morphological changes have occurred, these metabolites, their ratios and individual MR properties are potential (bio-)markers for therapy response monitoring [14–16].

However, the individual detection of 31P metabolites is hampered at lower magnetic field strengths (3T and below) due to the restricted spectral bandwidth and the low detection sensitivity. By going to higher magnetic field strengths (e.g. 7T and higher), the SNR and spectral resolution are intrinsically enhanced [17,18]. These properties have a tremendous advantage for the low abundant ^{31}P metabolites and even allow

detection of the individual phosphomonoesters, (i.e. PE, PC) and diesters (i.e. GPE, GPC) [19].

Unfortunately, the imaging volume in conventional ^{31}P MRSI is limited as small birdcage or surface coils are used [5,20]. Surface coils generally require the use of high-energetic adiabatic RF pulses to achieve flip angle homogeneity as inhomogeneous excitations lead to signal variation in the acquired spectra over the large field of view. Adiabatic RF pulses usually result in high specific absorption rates (SAR), leading to longer repetition times (TR), clinically impractical scan times for a single protocol and a limiting number of consecutive scans. Full spectroscopic coverage of large organs such as the lungs is therefore challenging due to inhomogeneous $B_1^{+/-}$ fields and inhomogeneous excitation which increase with magnetic field strength.

In addition, MR imaging and spectroscopy are challenging near the lungs due to the presence of air, the relatively small amount of tissue and respiratory motion. Yet, previous studies claim that from a technical point of view MR imaging on clinical field strengths is a feasible method for screening lung cancer [21].

Recent studies from Loring et al. and van Houtum et al. have presented a ^{31}P whole-body birdcage coil designed for 7T [22,23]. Using the body coil in combination with the conventional adiabatic pulses for high and low flip angle excitations requires adiabatic half passage or BIR4 pulses respectively and would increase the cost effective B_1^+. This results in a narrow band width leading to multiple acquisition to capture the full spectra. By design this coil results in an improved homogeneous excitation, comparable to the ^{1}H whole-body birdcage coils of clinical 3T MR systems. This allows the use of rectangular pulses, which decreases global and local SAR, creating opportunities for fast spectroscopic imaging methods. In addition, they demonstrated that this ^{31}P-body coil even allowed quantification of transverse relaxation times and the feasibility of obtaining high flip angle chemical shift imaging (CSI), over a large field of view. However, the use of this coil was revealed with a 30% inter-subject variation of the flip angle using a single power setting for multiple volunteers. This raises questions for the need for individual ^{31}P calibration, especially at low flip angles, as only the effective flip angle and not B_1^+-field homogeneity is affected. Low flip angle excitations accompanied with short repetition times (TR) can be used for fast 3D CSI. The optimal SNR per unit of time at lower flip angles is acquired when the Ernst angle (α_E) is used and any deviation from this flip angle result in additional T_1 weighting and a lower SNR per unit of time [24]. The effects of a 30% flip angle deviation to the SNR per unit of time and consequently the acquired spectra can be evaluated by simulations. Excluding B_1 calibrations can decrease the total scan duration by 10 minutes or more, subsequently increasing patient comfort or allowing for additional scans or additional sampled averages to improve SNR. [25]

The primary aim of this study was to investigate the feasibility of 3D ^{31}P MR spectroscopic imaging at ultra-high field in combination with a ^{31}P whole-body birdcage coil in four lung carcinomas.

Materials & Methods

Simulations

The effect of an uncalibrated excitation that leads to a deviation from the Ernst angle (α_E) was assessed by simulating the SNR per unit of time for the α_E and for □□ with a ± 30% and ± 50% deviation over a TR/T_1-ratios range of 10^{-6} to 0.3. The latter is chosen with respect to a short TR of 60 ms and the longitudinal relaxation times (T_1) for ^{31}P metabolites of interest possibly ranging from 450 ms (α-ATP) to 7000 ms (GPE) [6]. The simulated spectroscopy signal shown in equation [1] was corrected for time differences by dividing with the square root of TR. The SNR per unit of time for all the calculated TR/T1-ratios were normalized to the maximum signal at α_E.

$$signal \propto \frac{\sin(\alpha)\left(1-e^{-\frac{TR}{T_1}}\right)}{1-\cos(\alpha)\,e^{-\frac{TR}{T_1}}} \qquad [1]$$

Materials

^{31}P MRSI was performed using an in-house designed ^{31}P whole body birdcage coil integrated in a 7T MR system (Philips Healthcare, Best, Netherlands) [22,23]. The body coil, tuned at 120.6 MHz, was powered by a 25kW amplifier (PID: 53-S26B-128, MKS Technologies, Shenzhen, Republic of China) resulting in a B_1^+ field-magnitude of 15μT at the isocentre. Two 1H-TxRx/31P-Rx arrays were constructed for the experiments. Array 1 (A1) contained a ^{31}P dual-coil receiver (10 x 16 cm^2, figure 1A) and two fractionated ^{1}H dipole antennas (30 cm) used as transceivers, both driven in quadrature mode. Array 2 (A2) contained a 16-channel ^{31}P body array with eight integrated ^{1}H dipole antennas, shown in figure 1B and C [26]. Spectroscopic imaging data and anatomical proton images for localization were acquired in four patients using one of the two different setups.

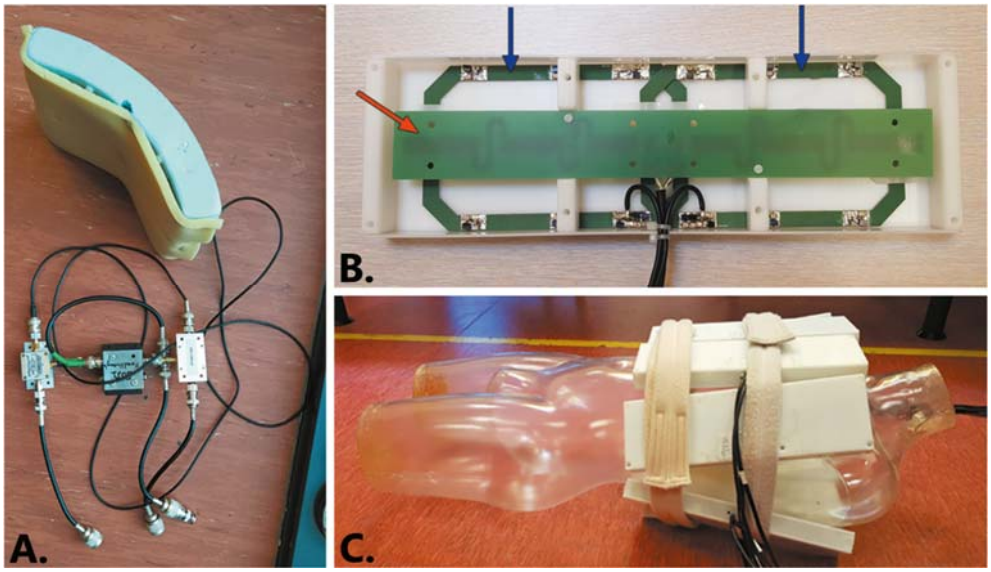

Figure 1. A.) Image of the ^{31}P dual- coil receiver from A1 with an apparent curvature to allow close contact with the body. **B.)** A view of one of the eight elements of the ^{31}P 16-channel receiver array from A2. Two ^{31}P receiver coils, overlapped to improve decoupling, are denoted by blue arrows and the ^{1}H meander dipole antenna for MR imaging is shown by the red arrow. **C.)** All eight elements of the ^{31}P 16-channel receiver array positioned around a plastic human mannequin representable for the *in vivo* setup for MR spectroscopic imaging of the upper torso targeting the lungs.

Patients & Setup

Four stage III-IV non-small cell lung carcinoma patients (ages: 53-63 years; BMI: 17.7-29.5 Kg/m^2) were included in this feasibility study and signed informed consent prior to scanning. Two patients participated after their palliative chemo- and/or radiotherapy sessions and two patients participated after the first immunotherapy cycle (see table 1 for details). Patients were scanned in supine position. Scans of two patients were acquired with the ^{31}P dual coil Rx (A1) placed on the location closest to the tumor based on previously acquired clinical CT images for tumor localization. The other two patients were scanned with the ^{31}P Rx array (A2), which was wrapped around the upper part of their torso. The two separate dipole antennas in A1 are positioned on the side and the top of the lung of interest. Maximum tumor dimension ranged from 25mm to 75mm and other clinical details per patient are shown in table 1.

Table 1. Clinical details of each patient including relevant remarks. The body-mass-index (BMI) is calculated as the weight (kg) divided by the length squared (m^2). Tumor sizes (cm^3) represent the maximum tumor length in each direction (RL x AP x FH) and corresponding maximum volumes (cc) determined from MR and/or CT images. Treatment of non-small cell lung carcinoma for these patients included systemic body radiation therapy (SBRT), chemoradiation and immunotherapy (Erlotinib, Pembrolizumab Abbreviations: superior vena cava (SVC).

Patient	Age (years)	BMI (kg/m^2)	Tumor size (cm^3|cc)	Therapy	Remarks
#1	59	20.4	7.25 x 1.75 x 1.00 | 12.69	Seq. chemoradiation	Stent in SVC close to tumor
#2	60	17.7	3.75 x 4.80 x 2.00 | 36.00	Thoracic SBRT	-
#3	63	24.2	3.60 x 3.20 x 3.60 | 41.47	Erlotinib	-
#4	53	29.5	3.60 x 3.00 x 2.50 | 27.00	Pembrolizumab	-

MR data acquisition

No B_0 shimming was performed nor was the ^{31}P B_1^+ calibration. Phosphorus (^{31}P) spectra were acquired using a 3D ^{31}P acquisition weighted CSI protocol including elliptical k-space sampling. Excitation was performed using rectangular RF pulses only and the carrier frequency was set to PCr. The isotropic resolution ranged from 20 to 30 mm and other parameters are summarized in table 2 [24].

Data processing

Spectroscopic data from the 3D CSI protocol were processed in Matlab 2018b (The Mathworks Inc., Natick, MA) using an open source in-house designed processing tool (CSIgui v1.1, http://www.csigui.tk, April 2019). ^{31}P spectroscopy data were averaged and spatially filtered using a 3D hamming window followed by an inverse Fourier transformation to the spatial domain. All free induction decays (FID) were apodized using a 24Hz gaussian filter and zero filled to 512 samples. Coil data was combined using the whitened singular value decomposition (WSVD) algorithm as reported by Rodgers et al [27]. Zeroth order phase correction was applied automatically, and first order phase correction was applied manually, thereafter.

No additional nor aesthetic baseline corrections were performed. Spectra from tumors exceeding the voxel resolution were aligned to the metabolite peak with the highest SNR followed by averaging, excluding voxels with a 50% or less partial tumor tissue volume on available MR images. The SNR of metabolites was calculated using equation [2] with S_{max}, the real part of the maximum signal intensity and the noise defined as the absolute standard deviation of the last 50 samples points of the spectrum.

$$SNR = \frac{real(S_{Max})}{|std(S_{noise})|} \qquad [2]$$

Table 2. 3D ^{31}P CSI protocol parameters for each patient including the resolution, matrix size (RL x AP x FH), repetition time (TR), echo time (TE), flip angle, bandwidth (BW), number of sampled averages (NSA), number of sample points, scan duration and number of ^{31}P receiver channels (#Rx). **α)** Nominal voxel volume corrected for weighted acquisition [24].

Patient	Resolution nominal (mm^3) | real $(cc)^{\alpha}$	Matrix (RL x AP x FH)	TR/TE (ms)	Flip Angle	BW (Hz)	NSA	Sample points	Scan duration (min:sec)	**#Rx (^{31}P)**
#1	26 x 26 x 26 | 31	7 x 5 x 6	60/0.54	20°	4800	320	256	23:00	2
#2	20 x 20 x 20 | 14	12 x 7 x 9	60/0.54	12°	4800	80	256	23:00	2
#3	30 x 30 x 30 | 48	12 x 6 x 6	60/0.51	9°	5000	60	256	25:55	16
#4	30 x 30 x 30 | 48	15 x 11 x 8	60/0.44	10°	4800	60	256	28:15	16

Results

Simulations resulted in a maximum decrease of 8% in SNR per unit of time within the used TR/T_1 range for + and -30% deviating flip angles, as can be seen in figure 2. In addition, the α_E + 30% variation showed a lower decrease in SNR per unit of time compared to the α_E - 30% variation. A similar trend is seen for a α_E ± 50% variation showing a maximum decrease of 23% in SNR per unit of time within the same TR/T1 range for the α - 50% variation. According to the B_1 maps available for the ^{31}P body coil, we could expect a maximum of 30% deviation in flip angle in the *in-vivo* measurements using equal power settings between subjects and, in addition, a maximum decrease in SNR per unit of time of less than 6% is seen for the TR/T_1-ratios range that corresponds to the ^{31}P metabolites of interest (0.009; 0.13) and the proposed protocol TR (60 ms) [23].

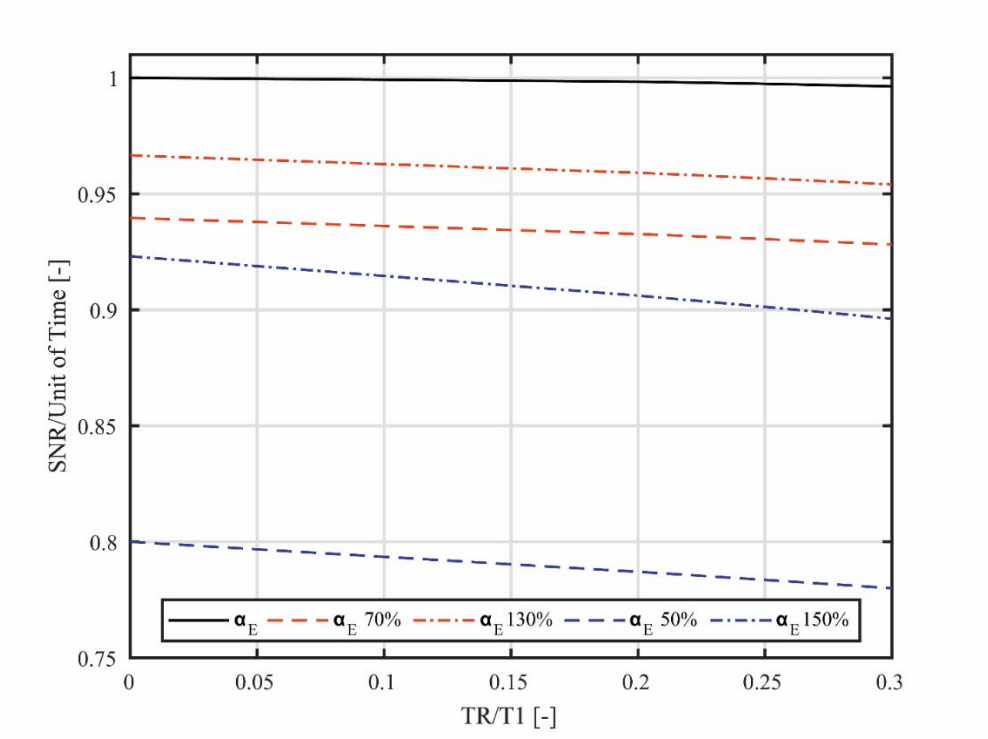

Figure 2. Simulation of the SNR per unit of time for the 3D ^{31}P spectroscopic imaging at Ernst angle (α_E) and with a 30% and 50% deviation for the TR/T_1 ratio ranging from 10-6 to 0.3. The SNR per unit of time at αE is marked by the solid black line, the increased and decreased angles for both the 30% (red) and 50% (blue) deviations are displayed as dashed and dash-dotted lines respectively.

All patients were imaged within an hour of scan time with one of the two setups. Positioning the ^{1}H transmit coils for patient #1 was limited due to a stent in the superior vena cava (SVC) located close to the tumor. No other patient related difficulties were experienced during the scan sessions. Images obtained with the dipole antenna in A1 were adequate for tumor localization and planning (Fig. 3A), when tumor location was known from previous CT images (Fig. 3B).

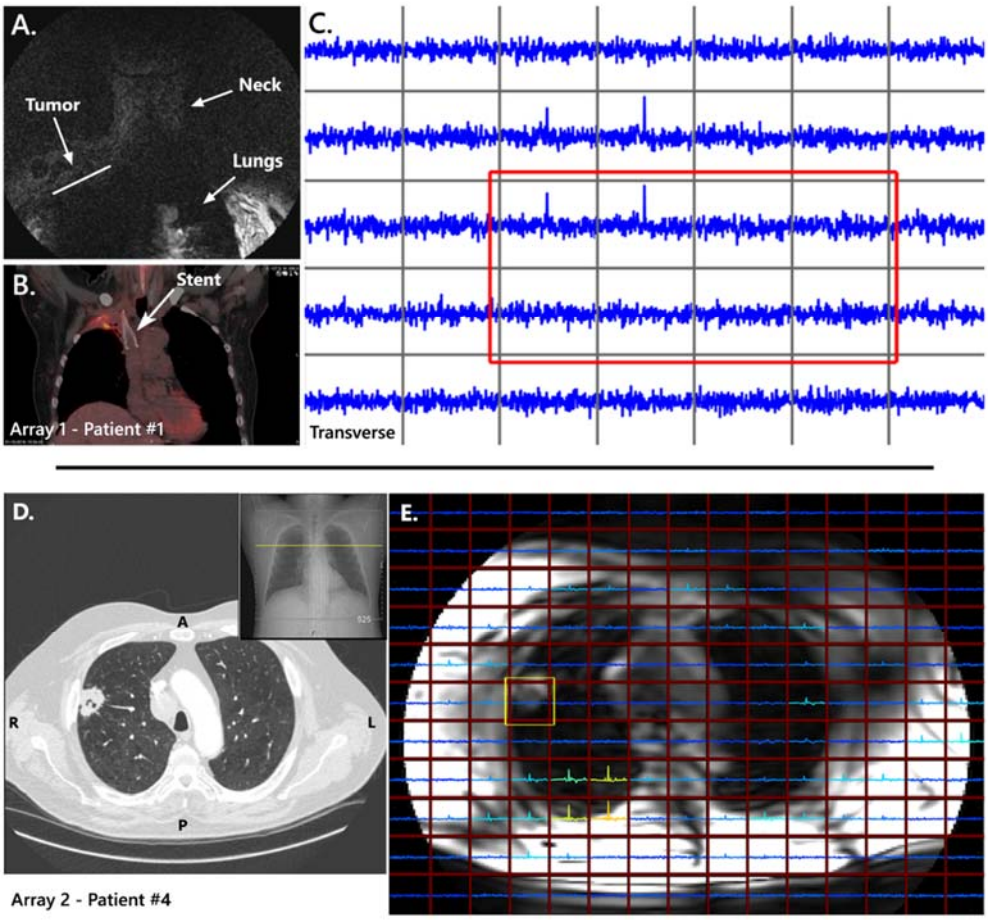

Figure 3. A) Coronal MR image including labels for the tumor, neck and lungs plus **B)** a coronal CT image with PET scan overlay, both from patient #1 and used for tumor localization. **C)** Single transverse slice of the 3D spectroscopic imaging data from patient #1 with the tumor voxels indicated by the red rectangle. **D)** Transverse and coronal CT images from patient #4 for tumor localization and planning. **E)** The MR image from patient #4 with an overlay of a single slice of the 3D spectroscopic imaging data. Tumor voxels are highlighted by the yellow rectangle.

Images and tumor localization using A2 were improved compared to A1 as is depicted in figure 3A and 3E. Spectroscopic imaging acquisitions could be obtained with both setups as shown in figures 3C & E, where a single spectroscopy slice from the 3D imaging set for patient #1 and #4 are shown respectively. Tumor voxels in the slice used for averaging are marked by the red and yellow rectangles, showing 8 out of 20 voxels for patient #1 and all tumor voxels for patient #4. In addition, the signal intensity of the voxels located at the posterior side of the patient in the spectroscopic imaging array in figure 3E have higher SNR compared to the anterior side.

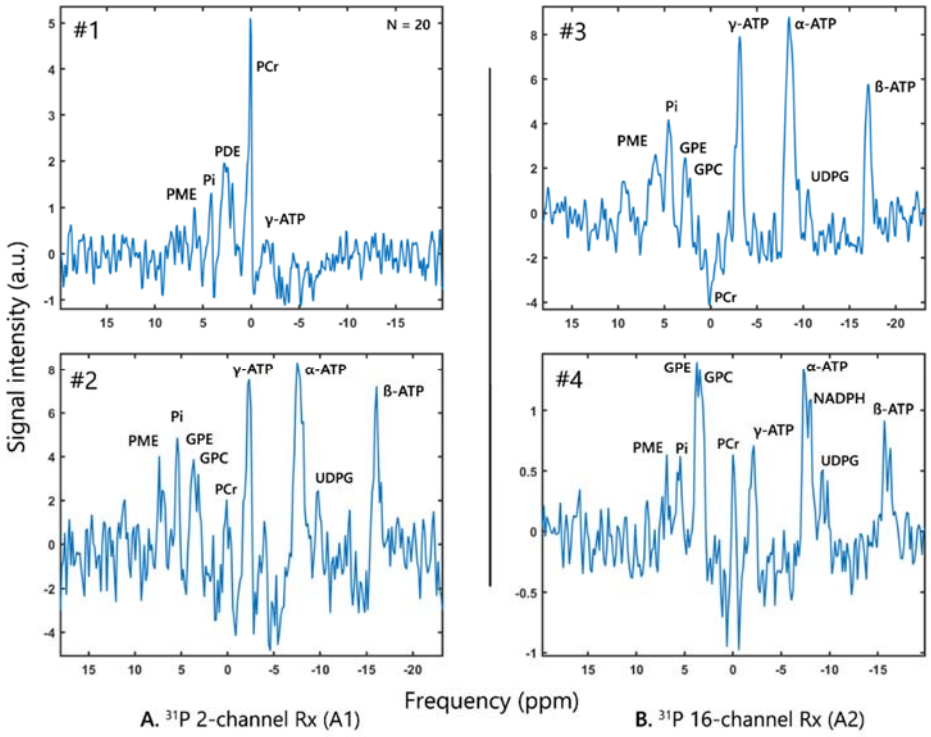

Figure 4. Spectra of lung tumor tissue for all four patients acquired with the ^{31}P chemical shift imaging protocol using **A)** A1, the ^{31}P dual coil Rx and **B)** A2, the ^{31}P 16-channel Rx array. Phosphomonoesters (PME), phosphodiesters (PDE), glycerophosphoethanolamine (GPE) plus glycerophosphocholine (GPC), inorganic phosphate (Pi), phosphocreatine (PCr) and the α-, β- and γ- ATP resonances are labelled where applicable. The number of tumor voxels used for averaging is denoted by N in the right top corner of the spectrum except for single voxel spectra. Notice the increase in PDE with respect to PME in patient #4 that might indicate tumor response to immunotherapy.

Obtained ^{31}P lung carcinoma spectra were acquired with high SNR for PCr (9.5) and the ATP resonances (>4.7) using A1, the ^{31}P dual-coil Rx (Fig. 4A) and with high SNR ranging from 3.9 (PME) to 13.2 (α-ATP) using A2, the ^{31}P 16-channel Rx array (Fig. 4B) . It allowed discrimination of PME, Pi, PDE, PCr in all patients, the three ATP resonances and UDPG in all subjects except for patient #1 and NADPH in

patient #4. Moreover, the SNR of the phospholipid- and energy- metabolites was found higher with A2 compared to A1. The lack of B_0 shimming and partial volume effects over the large field of view is visible in the spectra with measured linewidths ranging from 0.20 ppm to 1.1 ppm after apodization when using either coil setup.

Discussion

3D ^{31}P spectroscopic imaging was successfully obtained in four lung carcinoma patients with either the ^{31}P dual-coil receiver or the 16-channel receiver array in combination with the integrated ^{31}P body coil at 7 tesla. Both Rx setups allowed the acquisition of phosphorous metabolic information from the lung carcinoma via a non-invasive method, while targeting the full organ for evaluation. The increased spectral resolution at the ultra-high magnetic field strength of 7T allowed differentiation of multiple phosphorous metabolites related to cell membrane and energy metabolism. A minimal decrease in SNR per unit of time was apparent from the simulations performed to study the effect of a +/-30% deviation from the Ernst angle due to the lack of individual body coil power calibrations in this patient population. This minimal SNR loss of at maximum 8% allowed for 3D fast spectroscopic imaging with short TR and low flip angle excitation without time-consuming calibration steps during the scan session.

Increasing the number of receiver coils improved the field of view coverage of ^{31}P MRS images expanding the available metabolic information over a larger field of view. This agrees with previous demonstrations in literature [28]. In addition, the SNR increase gained with the 16-channel receiver array used in patient #3 and #4 not only allowed discrimination of PME, Pi, GPE, GPC, PCr, ATP (with α-, ß- & γ-resonances) and uridine-diphosphate glucose (UDPG) as with the dual-coil receiver but also nicotinamide-adenine dinucleotide phosphate (NADPH) in patient #4. UPDG is a known liver metabolite and indicates minor liver signal contamination, however SNR was insignificant (SNR<3) [5]. NADPH (SNR>3) however, though also found in the liver, is a cofactor involved with anabolic reactions, already linked to tumor tissue [29]. In addition, the highest SNR of the dual-coil receiver was measured for PCr (Fig. 4A, Patient #1) which is not directly associated with tumor tissue, but rather muscle tissue [5]. This can be explained by signal contamination from chest muscle signals contained in neighbouring voxels that bled in the tumor voxel location due to the small field of view of this patient, which excluded the full body circumference, in combination with the relatively large voxel size. Additional averaging of the 20 voxels also increased signal contamination in this patient but was required to regain the SNR of the spectrum. Spectra acquired with the 16ch Rx still show signal contamination, as can be seen by the remaining PCr peaks, though to a lesser extent than the first patient and even in opposite phase (fig 4B, patient #3). The lung and tumor morphology itself may already minimize signal contamination from

neighbouring voxels as tissue density in healthy lung tissue is, compared to other areas in the body, extremely low. Further protocol development could minimize signal contamination within a short time frame by increasing spatial voxel resolution or reducing point spread by more complex k-space weightings and filtering [24]. Another strategy could be the use of selective pulses to fully eliminate specific tissue signal such as the one coming from the muscles.

The top part of the torso, especially at the collar bones, limits proper positioning of the top elements of the receiver array. The eight rigid elements of the array lack the body-shaped curvature, disfavouring coil loading and resulting in a suboptimal receive fields for these coils. This can be seen by the increased SNR at the posterior side of the patient compared to the anterior voxels shown in figure 3C. Additional suboptimal coil combinations using the WSVD algorithm could also disfavour the SNR gradient over the spectroscopic image.

Moreover, in the presence of large susceptibility differences, such as the lung itself, implants and the moving heart, spectral quality is surprisingly adequate for the distinction of the metabolites, even without B_0 shimming. Resulting B_0 homogeneity was adequate with a spectral linewidth ranging between 0.2 and 1.1 ppm. This B_0 non-uniformity is much less critical than for ^{1}H MRS as the spectral separation between metabolites (i.e. PME versus PDE) is substantial (i.e. >3.5ppm) at 7T. However, it should still be noted that the B0 field uniformity can be highly variable both spatially as temporally. In our previous study we simulated spatiotemporal magnetic field uniformity, which at worst case conditions (i.e. at diaphragm comparing fully inhaled versus exhaled condition) could be up to 3ppm [30]. Either avoiding inclusion of subjects with tumors in locations of such severe non uniformities or using new means of local shim coils that can mitigate these distortions may be required [31]. In addition, shimming procedures could be performed within a breath-hold and when combined with gating it is expected to improve linewidth, possibly increasing sensitivity to allow detections of the individual PME and PDE [32].

In this study we have altered the flip angle between subjects. As prior knowledge about signal levels was unknown, we started by focusing on ATP, therefore setting the flip angle to 20°.After confirming observation of phospholipids, the angle was set to 9° (i.e. Ernst angle for PME and PDE). Finally, we completed the protocol by small over-tipping to also consider SNR of other metabolites that all have a shorter T_1. Note that the spectra are obtained with T_1 weighting, so altered peak ratios can be caused by concentration differences, but also by alterations in T_1. To extract the T_1 dependence, subject specific T_1 knowledge could be obtained by acquiring the same scan twice albeit with a different flip angle.

Conclusion

We conclude that ^{31}P MRSI in lung carcinoma is feasible at 7T. Employing large receiver arrays that can cover the whole torso, improves the field of view coverage allowing full organ ^{31}P-MRSI acquisition. With only minor signal contamination to overcome, ^{31}P MRSI shows great potential as tumor biomarker for treatment response monitoring in lung cancer.

References

1. Hirsch FR, Scagliotti GV, Mulshine JL, Kwon R, Curran WJ, Wu Y-L, Paz-Ares L. Lung cancer: current therapies and new targeted treatments. *Lancet*. 2017;389(10066):299-311. doi:10.1016/S0140-6736(16)30958-8
2. Ribas A, Wolchok JD. Cancer immunotherapy using checkpoint blockade. *Science*. 2018;359(6382):1350-1355. doi:10.1126/science.aar4060
3. Krikken E, van der Kemp WJM, van Diest PJ, van Dalen T, van Laarhoven HWM, Luijten PR, Klomp DWJ, et al. Early detection of changes in phospholipid metabolism during neoadjuvant chemotherapy in breast cancer patients using phosphorus magnetic resonance spectroscopy at 7T. *NMR Biomed*. 2019;32(6):e4086. doi:10.1002/nbm.4086
4. van der Kemp W, Stehouwer B, Luijten P, van den Bosch A, Klomp D. Detection of alterations in membrane metabolism during neoadjuvant chemotherapy in patients with breast cancer using phosphorus magnetic resonance spectroscopy at 7 Tesla. *Springerplus*. 2014;3. doi:10.1186/2193-1801-3-634
5. Valkovič L, Chmelík M, Kršňák M. In-vivo31P-MRS of skeletal muscle and liver: A way for non-invasive assessment of their metabolism. *Analytical Biochemistry*. 2017;529:193-215. doi:10.1016/j.ab.2017.01.018
6. Chmelik M, Považan M, Kršňák M, Gruber S, Tkačov M, Trattnig S, Bogner W. In vivo 31P magnetic resonance spectroscopy of the human liver at 7 T: an initial experience. *NMR in Biomedicine*. 2014;27(4):478-485. doi:10.1002/nbm.3084
7. Klomp DWJ, Bank BL van de, Raaijmakers A, Korteweg MA, Possanzini C, Boer VO, Berg CAT van de, et al. 31P MRSI and 1H MRS at 7 T: initial results in human breast cancer. *NMR in Biomedicine*. 2011;24(10):1337-1342. doi:10.1002/nbm.1696
8. van der Kemp WJM, Boer VO, Luijten PR, Stehouwer BL, Veldhuis WB, Klomp DWJ. Adiabatic multi-echo 31P spectroscopic imaging (AMESING) at 7 T for the measurement of transverse relaxation times and regaining of sensitivity in tissues with short T2* values. *NMR Biomed*. 2013;26(10):1299-1307. doi:10.1002/nbm.2952
9. Negendank W. Studies of human tumors by MRS: A review. *NMR in Biomedicine*. 1992;5(5):303-324. doi:10.1002/nbm.1940050518
10. Glunde K, Jie C, Bhujwalla ZM. Molecular Causes of the Aberrant Choline Phospholipid Metabolism in Breast Cancer. *Cancer Res*. 2004;64(12):4270-4276. doi:10.1158/0008-5472.CAN-03-3829
11. Park JM, Park JH. Human in-vivo 31P MR Spectroscopy of Benign and Malignant Breast Tumors. *Korean J Radiol*. 2001;2(2):80-86. doi:10.3348/kjr.2001.2.2.80
12. Runge JH, van der Kemp WJM, Klomp DWJ, Luijten PR, Nederveen AJ, Stoker J. 2D AMESING multi-echo 31P-MRSI of the liver at 7T allows transverse relaxation assessment and T2-weighted averaging for improved SNR. *Magnetic Resonance Imaging*. 2016;34(2):219-226. doi:10.1016/j.mri.2015.10.018
13. van der Kemp WJM, Velden TA van der, Schmitz AM, Gilhuijs KG, Luijten PR, Klomp DWJ, Wijnen JP. Shortening of apparent transverse relaxation time of inorganic phosphate as a breast cancer biomarker. *NMR in Biomedicine*. 2018. doi:10.1002/nbm.4011
14. Steen RG. Response of Solid Tumors to Chemotherapy Monitored by in Vivo 31P Nuclear Magnetic Resonance Spectroscopy: A Review. *Cancer Res*. Agust 1989:12.
15. Ng TC, Grundfest S, Vijayakumar S, Baldwin NJ, Majors AW, Karalis I, Meaney TF, et al. Therapeutic response of breast carcinoma monitored by 31P MRS in situ. *Magnetic Resonance in Medicine*. 1989;10(1):125-134. doi:10.1002/mrm.1910100112

16. Semmler W, Gademann G, Bachert-Baumann P, Zabel HJ, Lorenz WJ, van Kaick G. Monitoring human tumor response to therapy by means of P-31 MR spectroscopy. *Radiology*. 1988;166(2):533-539. doi:10.1148/radiology.166.2.3336731
17. Kraff O, Fischer A, Nagel AM, Mönninghoff C, Ladd ME. MRI at 7 tesla and above: Demonstrated and potential capabilities. *Journal of Magnetic Resonance Imaging*. 2015;41(1):13-33. doi:10.1002/jmri.24573
18. Redpath TW. Signal-to-noise ratio in MRI. *BJR*. 1998;71(847):704-707. doi:10.1259/bjr.71.847.9771379
19. Purvis LAB, Clarke WT, Valkovič L, Levick C, Pavlides M, Barnes E, Cobbold JF, et al. Phosphodiester content measured in human liver by in vivo 31P MR spectroscopy at 7 tesla. *Magnetic Resonance in Medicine*. 2017;78(6):2095-2105. doi:10.1002/mrm.26635
20. van der Kemp WJM, Klomp DWJ, Wijnen JP. 31P T2s of phosphomonoesters, phosphodiesters, and inorganic phosphate in the human brain at 7T. *Magnetic Resonance in Medicine*. 2018;80(1):29-35. doi:10.1002/mrm.27026
21. Biederer J, Ohno Y, Hatabu H, Schiebler ML, van Beek EJR, Vogel-Claussen J, Kauczor H-U. Screening for lung cancer: Does MRI have a role? *European Journal of Radiology*. 2017;86:353-360. doi:10.1016/j.ejrad.2016.09.016
22. Löring J, van der Kemp WJM, Almujayyaz S, van Oorschot JWM, Luijten PR, Klomp DWJ. Whole-body radiofrequency coil for (31) P MRSI at 7 T. *NMR Biomed*. 2016;29(6):709-720. doi:10.1002/nbm.3517
23. van Houtum Q, Arteaga de Castro CS, Klomp DWJ, van der Kemp WJM. Full coverage 31P MRSI of the liver with a body coil at 7T. *ISMRM 2019*. 2019;ISMRM 27th Annual Meeting. http://cds.ismrm.org/protected/19MPresentations/abstracts/0487.html.
24. Pohmann R, von Kienlin M, Haase A. Theoretical Evaluation and Comparison of Fast Chemical Shift Imaging Methods. *Journal of Magnetic Resonance*. 1997;129(2):145-160. doi:10.1006/jmre.1997.1245
25. Clarke WT, Robson MD, Rodgers CT. Bloch-Siegert B1+-mapping for human cardiac (31) P-MRS at 7 Tesla. *Magn Reson Med*. 2016;76(4):1047-1058. doi:10.1002/mrm.26005
26. Raaijmakers AJE, Italiaander M, Voogt IJ, Luijten PR, Hoogduin JM, Klomp DWJ, van den Berg CAT. The fractionated dipole antenna: A new antenna for body imaging at 7 Tesla. *Magn Reson Med*. 2016;75(3):1366-1374. doi:10.1002/mrm.25596
27. Rodgers CT, Robson MD. Receive array magnetic resonance spectroscopy: Whitened singular value decomposition (WSVD) gives optimal Bayesian solution. *Magn Reson Med*. 2010;63(4):881-891. doi:10.1002/mrm.22230
28. Valkovič L, Dragonu I, Almujayyaz S, Batzakis A, Young LAJ, Purvis LAB, Clarke WT, et al. Using a whole-body 31P birdcage transmit coil and 16-element receive array for human cardiac metabolic imaging at 7T. *PLoS ONE*. 2017;12(10):e0187153. doi:10.1371/journal.pone.0187153
29. Roy K, Wu Y, Meitzler JL, Juhasz A, Liu H, Jiang G, Lu J, et al. NADPH oxidases and cancer. *Clinical Science*. 2015;128(12):863-875. doi:10.1042/CS20140542
30. Andersen M, Hanson LG, Madsen KH, Wezel J, Boer V, van der Velden T, van Osch MJP, et al. Measuring motion-induced B0 -fluctuations in the brain using field probes. *Magn Reson Med*. 2016;75(5):2020-2030. doi:10.1002/mrm.25802
31. van den Wildenberg L, van Houtum Q, van der Kemp WJM, Arteaga de Castro CS, Nassirpour S, Chang P, Klomp DWJ. B0 Shimming of the liver using a local array of shim coils in the presence of respiratory motion at 7T. *ISMRM 2019*. 2019; #0221 (ISMRM 27th Annual Meeting). https://cds.ismrm.org/protected/19MPresentations/abstracts/0221.html.
32. Boer VO, Bank BL vd, Vliet G van, Luijten PR, Klomp DWJ. Direct B0 field monitoring and real-time B0 field updating in the human breast at 7 tesla. *Magnetic Resonance in Medicine*. 2012;67(2):586-591. doi:10.1002/mrm.23272

Chapter 7

Summary and general discussion

NMR in Biomedicine 2019

Keywords: ^{31}P MR spectroscopic imaging, response monitoring, lung carcinoma, X-nuclei MRS, *in vivo* application.

Summary

In recent years a paradigm shift in therapy evaluations for oncology is apparent. Solely focusing on the morphological changes with the variety of imaging modalities is not sufficient to assess tumor progression or drug non-response early during treatment. Monitoring earlier than the current minimum of several months of chemotherapy would allow changes in therapy before tumor progression or additional complications for the patient in non-responding treatments. A non-invasive method available with ultra-high field MR spectroscopic imaging may therefore become a necessity to pave the way for individualized medicine.

In the first part of this thesis the changes of relaxation times were quantified in *ex vivo* porcine recta during formaldehyde fixation and in human specimen. **Chapter 2** concludes that the T_1 relaxation time of the circular muscle, mucosa and submucosa, and the T_2 relaxation time of the circular muscle decreased. Consequently, fixation, prior to imaging, progressively decreases image contrast. The human specimens were therefore imaged during the first few hours of fixation, in search for a suitable diagnostic marker to evaluate tumor discrimination. However, no conclusive parameter from traditional MRI techniques, neither T_1 nor T_2, resulted as a significant diagnostic parameter for therapy evaluation.

When incorporating MR spectroscopic imaging as a tool to study metabolic alterations to treatments as potential biomarker, the tissue must be studied *in vivo*. First step towards bringing metabolic imaging to patients is to ensure good magnetic field (B_0) uniformity. The improvements of the B_0-field homogeneity in the body by simulating a local array of shim coils on liver MRI during different respiratory states are investigated in **chapter 3**. From simulations it is apparent that the increased degrees of freedom, available with the local array of shim coils improve homogeneity to a greater extent (10%) than solely using the standard shim hardware. Shimming B_0 dependent on the different respiratory states allows even further improvements of B_0 homogeneity, ranging from 21 to 44 %, reducing the effects of the respiratory motion. This holds great promise for both full body MR imaging and MR spectroscopy, especially at higher field strengths as achieving homogeneity becomes more complex with increasing field strengths.

The next step in bringing metabolic MRI to patients is to facilitate effective excitation of ^{31}P spins. **Chapter 4** presents the integration of a ^{31}P whole-body birdcage coil to 7 tesla, to enable ^{31}P MRS over large fields of views. The design of the coil allows use of rectangular RF pulses which decreases the overall SAR compared to adiabatic RF pulses while maintaining flip angle homogeneity without compromising bore diameter to accompany larger patients or receiver arrays. The coil permits exchange in SNR for an increase in spatial resolution and/or MR weighting in ^{31}P

MR spectroscopic imaging by altering flip angle or repetition time. Within SAR constraints, the number of RF pulses per unit of time can be increased as is demonstrated by fast 3D chemical shift imaging (CSI) of the full liver with a short TR and low flip-angle excitation to acquire optimal SNR per unit of time. Furthermore, the T_2 of PCr in the gluteal muscle was quantified, using a multi-echo spectroscopic imaging protocol, something previously not possible in such large volumes in the body as the energy deposition resulting from adiabatic refocusing pulses is too high. This creates opportunities for monitoring the physiology of tissue to aid further advances in therapy assessment in oncology.

Proper interpretation of accompanied data retrieved from these experiments required development of a processing and analysis tool, CSIgui as explained in **chapter 5**. The large data sets have a high number of dimensionalities and are therefore not handled well by current software solutions on default MR systems or available MRS analysis platforms. The developed tool is compatible with conventional MRS file types such as dicom and spar/sdat but can also load raw data formats. Data can be processed using a variety of MR algorithms and saved for further analysis using conventional software to allow easy integration with existing research studies.

The last part, **chapter 6**, focuses on the feasibility of acquiring 3D chemical shift images of tumor tissue in four lung carcinoma patients using the ^{31}P whole body birdcage coil in combination with a dual Rx coil or a Rx array setup. First, simulations proved the loss in SNR per unit of time with imperfect flip angles is minimal using a short TR low flip angle protocol, eliminating a time-consuming calibration process. The 3D ^{31}P-CSI were acquired successfully in four lung carcinoma patients using either receiver setup. However, the use of the receiver array favored SNR over a larger field of view compared to the dual coil setup. The increased spectral resolution at 7T allowed detection of energy related metabolites such as ATP and Pi, but also the phospholipid metabolites including the individual PME, PE and PC, and PDE, GPC and GPE which are not detectable at 3T, due to the lower spectral resolution. Therefore, it is concluded that ^{31}P MRSI of lung tumors at 7T is feasible and warrants further research to assess the potential as a non-invasive method for therapy evaluation.

General discussion & future perspective

The starting point of this thesis is the problem that current image-based assessment of tumor therapy efficacy is not sensitive enough to monitor effects early on during treatment. The result from chapter 2 where ex *vivo* human rectum specimens were imaged at very high resolutions did not provide a suitable MR parameter to even discriminate tumor from healthy tissue. However, the changes caused by formaldehyde fixation were monitored by quantifying the relaxation parameters,

including tissue dehydration by changes in proton density. It may well be that physiological assessment, if possible, is more suited to exclude patients from mesorectal excision. Though these fixative effects can be avoided by imaging immediately at start of fixation or retrospectively corrected using the quantified changes over time, the B_0 and B_1 inhomogeneities in these *ex-vivo* samples also complicated the aim of the study. Translation to the *in vivo* situation will worsen these inhomogeneities due to motion e.g. blood flow, respiration and peristaltic movements of the intestine and, in addition, the required larger field of views are difficult to shim using current shim hardware. Previous MR imaging studies on rectum, cervix and prostate used an endorectal coil to improve the sensitivity [1–4]. An endorectal balloon attached to the coil to allow filling with a saline solution can minimize the B_0 artefacts caused by susceptibility differences between air and tissue, more prevalent with the lumen in the rectum [5]. Although low discomfort of this type of coil is reported for cervical cancer patients, the rectal and prostate patients can suffer from inflammation and/or irritation to surrounding tissue due to treatment, increasing the burden[1]. Also the diagnostic performance is not superior, at least at 3T but can increase SNR up to 4-fold at 7T [2,6,7].

The B_0 field inhomogeneities increase in complexity with increasing field strengths and from chapter 3 it is apparent that a local array of shim coils can improve the standard scanner shim. The focus on the three respiratory states also shows an additional advantage of using these shim settings over a breathing cycle. Dynamically shimming the B_0 field could minimize frequency shifts and line broadening but also increase the temporal SNR and all favor time consuming MR protocols such as chemical shift imaging. Furthermore, larger volumes such as the liver or artefact prevalent areas such as the rectum potentially could also benefit from the local shim array. In addition to the local array of shim coils to improve B_0 homogeneity dynamically during the breathing cycle, triggered acquisition or retrospective correction methods are also available [8].

Changes to the image based assessment paradigm are evident as studies already incorporate dual-tuned coils e.g. coils tuned to two nuclei, to enable MR spectroscopy during MR imaging in rectal carcinoma [7]. To enable therapy assessment anywhere in the body, a new strategy is required, and this thesis presents tools to monitor tissue metabolism using ^{31}P MRS in muscles, liver and even the lungs. Chapter 4 demonstrates multiple acquisition methods of ^{31}P metabolites using a ^{31}P whole-body birdcage coil at 7T. In addition to MR imaging at ultra-high field, it is now possible to acquire metabolic information about phospholipid and energy metabolism non-invasively over a large field of view with reduced SAR constrains compared to surface coils. Covering the entire organ of interest generates additional spatial dependent physiological information to allow spatial evaluation. Furthermore, quantification of metabolite specific MR parameters using the MESING

protocol allows longitudinal and comparative studies. It has already been demonstrated that the transverse relaxation parameter of a specific metabolite is a potential diagnostic biomarker in breast cancer patients [9]. Though the dimensions of these residual tumors need to be relatively large as the spatial resolution is low compared to imaging. Consequently, a CSI voxel will usually contain tumor as well as healthy tissue resulting in a mixed spectrum.

Signal contamination from abundant tissue such as muscles requires investigation. Multiple techniques are demonstrated in this thesis such as Hamming filtering and weighted k-space acquisition reducing signal contamination. A fat saturating pre-pulse is common practice in ^{1}H MRS and MRI and such technique could minimize the signal contamination from muscles in ^{31}P MRS [10].

The ^{31}P body coil setup combined with a receive array necessitates the development of a software tool to process the altered data output as presented in chapter 5. In addition to analysis and processing, the software of the MR system also requires upgrading to handle the new hardware properly and enable displaying the altered data output, further investigation into new sequences and combining existing MR techniques such as triggered acquisition with spectroscopy.

The full potential of ^{31}P MRSI using the ^{31}P whole body birdcage coil to improve therapy evaluation is demonstrated in chapter 6. The ^{31}P spectra acquired in the four lung carcinoma patients show the ^{31}P metabolites in tumor tissue and it can be hypothesized therapy effects are visible in patients due to high signal of PDE compared to PME. As PDEs are cell degradation products this could be indicative of effective immunotherapy, which results in cell death through apoptosis or necrosis [11]. In addition, sensitivity was still significant even though the susceptibility differences with air and tissue in the lungs are abundant. Further improvements to ^{31}P of the body coil could allow active shimming of the B_1^+ field using a dual output amplifier. Additionally, more receivers will also increase SNR resulting in improved sensitivity. New strategies to map the B_1^+ field could also increase sensitivity as the subjects positioned in the MR bore still induce minor flip angle inhomogeneities [12]. This favors absolute quantification of metabolite concentrations as it requires a spatially homogenous flip angle distribution. In terms of patient comfort, advances can be made by shortening scan sessions. As the frequencies of ^{1}H and ^{31}P are well separated, interleaved or even simultaneous MR imaging and spectroscopy is possible.

Translation of the techniques described in this thesis to the clinic will require patient studies to explore and validate new MR biomarkers that show correlation with therapy efficacy. In addition to the phospholipid metabolism the energy metabolism can be monitored through the ATP resonances and used in other application besides

therapy evaluation [13,14]. It is known that efficacy of chemotherapeutics is hampered by a high acidity of the tumor environment compared to healthy tissue and ^{31}P MRS could also be used to assess pH and may even improve drug targeting and efficacy [15]. This could also increase the understanding of extracellular and intracellular tumor environment as differences between pH are reported though the underlying mechanism is not completely understood [16].

Not only ^{31}P MRSI can be investigated for therapy evaluation, other MR detectable nuclei can also be explored. For example, fluorine (^{19}F) can be detected and is present in chemotherapeutics as fluorouracil and capecitabine, allowing to monitor drug targeting *in vivo* [17]. Deuterium metabolic imaging (^{2}H, DMI) already is presented as a great tool for metabolic imaging [18]. However, DMI requires a contrast agent (e.g. deuterated glucose) which is relatively expensive. Sodium imaging (^{23}Na) can also help in therapy evaluation as sodium concentrations are increased in tumor tissue compared to healthy tissue [19,20].

Conclusion

This thesis presents new strategies to evaluate tumor therapy response and demonstrates multiple tools to improve *in vivo* ^{31}P metabolic imaging for use in therapy evaluation. ^{31}P MRS over large volumes to cover full organs such as the liver, lungs and muscles is feasible using a ^{31}P whole body birdcage coil at 7 tesla. This enables monitoring of tissue physiology during treatment to increase understanding of tumor physiology and therapy effects but also metabolic imaging in general.

References

1. Hoogendam JP, Kalleveen IML, de Castro CSA, Raaijmakers AJE, Verheijen RHM, van den Bosch MAAJ, Klomp DWJ, et al. High-resolution T2-weighted cervical cancer imaging: a feasibility study on ultra-high-field 7.0-T MRI with an endorectal monopole antenna. *Eur Radiol*. 2017;27(3):938-945. doi:10.1007/s00330-016-4419-y
2. Gawlitza J, Reiss-Zimmermann M, Thörmer G, Schaudinn A, Linder N, Garnov N, Horn L-C, et al. Impact of the use of an endorectal coil for 3 T prostate MRI on image quality and cancer detection rate. *Sci Rep*. 2017;7. doi:10.1038/srep40640
3. Ertürk MA, Tian J, Van de Moortele P-F, Adriany G, Metzger GJ. Development and evaluation of a multichannel endorectal RF coil for prostate MRI at 7T in combination with an external surface array. *J Magn Reson Imaging*. November 2015:n/a-n/a. doi:10.1002/jmri.25099
4. Luttje MP, Italiaander MGM, Arteaga de Castro CS, van der Kemp WJM, Luijten PR, van Vulpen M, van der Heide UA, et al. (31) P MR spectroscopic imaging combined with (1) H MR spectroscopic imaging in the human prostate using a double tuned endorectal coil at 7T. *Magn Reson Med*. 2014;72(6):1516-1521. doi:10.1002/mrm.25070
5. Martin GV, Kudchadker RJ, Bruno TL, Frank SJ, Wang J. Comparison of prostate distortion by inflatable and rigid endorectal MRI coils in permanent prostate brachytherapy imaging. *Brachytherapy*. 2018;17(2):298-305. doi:10.1016/j.brachy.2017.09.014
6. van Kalleveen IML, Boer VO, Luijten PR, Klomp DWJ. Tilt optimized flip uniformity (TOFU) RF pulse for uniform image contrast at low specific absorption rate levels in combination with a surface breast coil at 7 Tesla. *Magn Reson Med*. 2015;74(2):482-488. doi:10.1002/mrm.25415
7. Philips BWJ, van Uden MJ, Rietsch SHG, Orzada S, Scheenen TWJ. A multitransmit external body array combined with a 1 H and 31 P endorectal coil to enable a multiparametric and multimetabolic MRI examination of the prostate at 7T. *Med Phys*. 2019;46(9):3893-3905. doi:10.1002/mp.13696
8. Boer VO, Bank BL vd, Vliet G van, Luijten PR, Klomp DWJ. Direct B0 field monitoring and real-time B0 field updating in the human breast at 7 tesla. *Magn Reson Med*. 2012;67(2):586-591. doi:10.1002/mrm.23272
9. van der Kemp WJM, Velden TA van der, Schmitz AM, Gilhuijs KG, Luijten PR, Klomp DWJ, Wijnen JP. Shortening of apparent transverse relaxation time of inorganic phosphate as a breast cancer biomarker. *NMR Biomed*. 2018. doi:10.1002/nbm.4011
10. Del Grande F, Santini F, Herzka DA, Aro MR, Dean CW, Gold GE, Carrino JA. Fat-Suppression Techniques for 3-T MR Imaging of the Musculoskeletal System. *RadioGraphics*. 2014;34(1):217-233. doi:10.1148/rg.341135130
11. Melcher A, Gough M, Todryk S, Vile R. Apoptosis or necrosis for tumor immunotherapy: what's in a name? *J Mol Med*. 1999;77(12):824-833. doi:10.1007/s001099900066
12. Clarke WT, Robson MD, Rodgers CT. Bloch-Siegert B1+-mapping for human cardiac (31) P-MRS at 7 Tesla. *Magn Reson Med*. 2016;76(4):1047-1058. doi:10.1002/mrm.26005
13. Bakermans AJ, Bazil JN, Nederveen AJ, Strijkers GJ, Boekholdt SM, Beard DA, Jeneson JAL. Human Cardiac 31P-MR Spectroscopy at 3 Tesla Cannot Detect Failing Myocardial Energy Homeostasis during Exercise. *Front Physiol*. 2017;8. doi:10.3389/fphys.2017.00939
14. Niess F, Schmid AI, Bogner W, Wolzt M, Carlier P, Trattnig S, Moser E, et al. Interleaved 31 P MRS/1 H ASL for analysis of metabolic and functional heterogeneity along human lower leg muscles at 7T. *Magn Reson Med*. December 2019. doi:10.1002/mrm.28088
15. Huber V, Camisaschi C, Berzi A, Ferro S, Lugini L, Triulzi T, Tuccitto A, et al. Cancer acidity: An ultimate frontier of tumor immune escape and a novel target of immunomodulation. *Semin Cancer Biol*. 2017;43:74-89. doi:10.1016/j.semcancer.2017.03.001
16. Milito AD, Fais S. Tumor acidity, chemoresistance and proton pump inhibitors. http://dx.doi.org/10.2217/14796694.1.6.779. https://www.futuremedicine.com/doi/abs/10.2217/14796694.1.6.779. Published November 24, 2005. Accessed February 13, 2020.
17. Gorp JS van, Seevinck PR, Andreychenko A, Raaijmakers AJE, Luijten PR, Viergever MA, Koopman M, et al. 19 F MRSI of capecitabine in the liver at 7 T using broadband transmit–receive antennas and dual-band RF pulses. *NMR Biomed*. 2015;28(11):1433-1442. doi:10.1002/nbm.3390

18. Feyter HMD, Behar KL, Corbin ZA, Fulbright RK, Brown PB, McIntyre S, Nixon TW, et al. Deuterium metabolic imaging (DMI) for MRI-based 3D mapping of metabolism in vivo. *Sci Adv*. 2018;4(8):eaat7314. doi:10.1126/sciadv.aat7314
19. Bangerter NK, Kaggie JD, Taylor MD, Hadley JR. Sodium MRI radiofrequency coils for body imaging. *NMR Biomed*. 2016;29(2):107-118. doi:10.1002/nbm.3392
20. Ouwerkerk R, Bleich KB, Gillen JS, Pomper MG, Bottomley PA. Tissue Sodium Concentration in Human Brain Tumors as Measured with 23Na MR Imaging. *Radiology*. 2003;227(2):529-537. doi:10.1148/radiol.2272020483

Appendices

Dutch Summary

Introductie

Therapie evaluatie in oncologie

Vanuit de oncologie is er grote vraag naar een goede methode voor de evaluatie van de therapie. Patiënten krijgen vaak chemotherapie, radiotherapie of een combinatie van beide wat een last voor de patiënt is, zeker als de therapie ineffectief is. Er gaat veel tijd verloren voordat deze ineffectiviteit gemeten kan worden met behulp van huidige klinische standaarden en verminderd daardoor werkzaamheid en zelfs mogelijke inzet van een andere therapie strategie zoals resectie of gebruik van andere chemotherapeuticum.

De behoefte voor verbetering van het meten van tumor response is herkenbaar in huidige behandeling van rectaal carcinoma, lever metastases en long carcinoma, omdat het onderscheiden van patiënten waarbij de therapie wel of niet aanslaat moeilijk is. De standaardbehandeling voor lokaal vergevorderde rectaal carcinoma is neoadjuvante chemotherapie vaak gevolgd door een totale mesorectale excisie (TEM) vanwege een gebrek aan sensitiviteit met conventioneel klinische MRI (3 tesla en lager) om te bepalen of patiënten een volledige respons hebben op de therapie. Echter, histologische onderzoeken van het verwijderde specimen toont geen residuele tumorcellen in bijna 20% van alle rectaal carcinoom patiënten.

Dit roept de vraag op of de huidige strategie de beste keuze is. Nieuwe strategieën proberen al een zogenaamde afwachtende methode uit e.g. wait-and-see waarbij de patiënt zorgvuldig wordt gevolgd na chemotherapie zonder excisie van het rectum waardoor de kwaliteit van leven voor veel patiënten verbeterd. In alle drie genoemde tumor types worden CT- of MR-beelden geanalyseerd door een radioloog die zich richt op de morfologische veranderingen van de tumor, e.g. de vorm, homogeniteit en meer om de therapierespons te evalueren. Deze veranderingen zijn echter pas zichtbaar na enkele maanden of meer aan chemotherapie of immunotherapie. Vroegere detectie van non-respons zou de oncoloog in staat stellen over te schakelen naar een andere behandeling, waardoor de herstelkansen van de patiënt toenemen en de kosten van gebruikte dure geneesmiddelen dalen. Hoewel fysiologische veranderingen altijd voorafgaan aan morfologische veranderingen, hangt de focus van de huidige klinische standaard nog steeds sterk af van het laatste. Daarom is het meten van tumorfysiologie om de effectiviteit van de therapie te evalueren van het grootste belang om de individuele patiëntenzorg te verbeteren. Hoewel tumormorfologie kan worden gevolgd door middel van magnetic resonance imaging (kernspintomografie, MRI), kan tumorfysiologie worden gevolgd door magnetic resonance spectroscopy (MRS).

MRI en MRS

MR-beeldvorming en spectroscopie zijn niet-invasieve technieken die een krachtig magnetisch veld gebruiken om beelden of moleculaire details vanuit het menselijk lichaam te verkrijgen. Kernen met een non-zero spin zoals waterstof (^{1}H) en fosfor (^{31}P) werken als magnetische dipolen, ofwel kleine magneten en gaan in lijn staan met het hoofdmagneetveld (B_0) terwijl ze roteren rondom deze as in dezelfde richting i.e. in precessie. Inhomogeniteiten van het B_0-veld van het MR-systeem resulteren in meerdere beeld- en spectrale artefacten die de beeldkwaliteit verminderen en worden veroorzaakt door anatomische bewegingen zoals de ademhaling, de hartcyclus, systeeminstabiliteit en verschillen in magnetische gevoeligheid van de verschillende weefsels in het lichaam. “Shimming” of “shimmen” is een methode om de B_0-homogeniteit te verbeteren door een offset toe te passen op het standaard beeldvormingsgradiëntsysteem of door gebruik te maken van shim-spoelen die B_0-inhomogeniteiten verminderen. De magnetische uitlijning (i.e. de magnetisatie) is in evenwicht en kan worden beïnvloed door energie te deponeren via het uitzenden (Tx) van radiofrequente (RF) pulsen met de precessiefrequentie, i.e. de Larmor-frequentie van een specifieke kern, met behulp van RF-spoelen. Na de puls keert de precesserende magnetisatie van de kernen terug naar evenwicht, waardoor een in de tijd variërende magnetische flux door de ontvangst (Rx) spoel ontstaat die een stroom induceert, het MR-signaal. In combinatie met magnetische gradiëntsystemen kan het MR-signaal spatieel worden gecodeerd om de signaalintensiteiten in kaart te brengen en te converteren naar een beeld. Bovendien wordt een kern beïnvloed door de positie in een molecuul doordat omliggende atomen met in het specifiek de elektronen de lading van de nucleus beïnvloedt i.e. electron shielding. MR-spectroscopie maakt gebruik van dit verschil omdat het een kleine verandering van de resonantiefrequentie veroorzaakt, waardoor verschillende moleculen en zelfs de verschillende kernen in een molecuul afzonderlijk gedetecteerd kunnen worden. Daarnaast maakt het de kwantificatie van concentraties, zuurtegraad van het weefsel en meer mogelijk. Het verkregen MRS-signaal wordt niet weergegeven als een afbeelding, maar als een spectrale weergave van het signaal met signaalpieken op een bepaalde frequentie voor de verschillende soorten moleculen.

Het onderscheiden van deze atomen met MRS en het verkrijgen van weefselcontrast in MRI is mogelijk vanwege het verschil in de snelheid waarmee de verstoorde magnetisatie terug naar evenwicht gaat. De snelheid wordt beïnvloed door interacties van de kern met zijn omringende spins en atomaire omgeving en kan worden gekenmerkt door de longitudinale relaxatietijd of snelheid (T_1). Deze constante beschrijft de snelheid waarmee de magnetisatie terugkeert naar equilibrium ofwel in lijn met het magneetveld. Tezamen met T_1 is een mechanisme aanwezig dat wordt beschreven door de transversale relaxatietijdconstante (T_2). Op macroscopisch niveau wisselen de kernen energie uit, waardoor zowel de

longitudinale als ook de transversale relaxatie wordt veroorzaakt. Bovendien veroorzaken kleine verschillen van de veldsterktes die aanwezig zijn door magnetische overgangsverschillen in de macroscopische omgeving de-fasering (T2') van de voorheen coherente spins. Beide mechanismen worden beschreven door T_2^*, de waargenomen transversale relaxatietijd. Deze eigenschappen maken het mogelijk beelden te maken met contrasten op basis van verschillen in de longitudinale of transversale relaxatiesnelheden, maar ook op basis van de chemische verschuivingen (chemical shift) van de Larmor-frequenties en meer.

Therapie evaluatie met MRS

Het beoordelen van de therapierespons van tumoren vereist een geschikte biomarker die indicatief is voor tumorweefsel en de effectiviteit van de behandeling. Huidig inzicht toont aan dat een veranderd cholinemetabolisme, dat een belangrijke rol speelt in het lipide metabolisme, geschikt is voor therapie-evaluatie, omdat het kan worden gevolgd met behulp van $_1$H MRS bij klinische veldsterktes (≤3 tesla). Het totale cholinegehalte (tCho), dat meerdere cholinemetabolieten bevat, zoals vrije choline, glycerofosfocholine en fosfocholine, is verhoogd in vergelijking met gezond weefsel en een verlaging van deze concentratie impliceert effectieve therapie. Bovendien maakt fosfor (^{31}P) MRS de acquisitie mogelijk van specifieke energie- en fosfolipide-metabolieten *in vivo*. Het cel-energiemetabolisme kan worden bepaald door monitoring van anorganisch fosfaat (Pi), fosfocreatine (PCr) en adenosinetrifosfaat (ATP, met α -, ß- en γ-resonanties). De verhoudingen van deze metabolieten worden al gebruikt als diagnostische biomarkers, aangezien verandering indicatief is voor systemische ziekten zoals diabetes. ^{31}P MRS kan ook celmembraan bouwstenen, de fosfomonoester (PME) en celmembraanafbraakproducten, de fosfodiesters (PDE) detecteren. In overeenstemming met tCho als een biomarker in ^{1}H MRS, suggereert toename van de PME tot PDE-verhoudingen proliferatie en is gecorreleerd met tumorweefsel. Een afname van deze verhoudingen tijdens therapie is een maat voor de therapierespons en vindt plaats voordat morfologische veranderingen kunnen worden waargenomen.

Echter, ^{1}H/^{31}P MRS op klinische veldsterktes vereist grote volumes en veel signaalmiddelingen om een significante signaal-ruis-verhouding (SNR) te verkrijgen welke afdoende is voor evaluatie, vanwege het natuurlijk verminderd voorkomen van ^{31}P vergeleken met ^{1}H en de lage spectrale resolutie. Metabole ^{1}H-signalen kunnen ook worden gemaskeerd door zeer overvloedige lipiden- en watersignalen die overlappende pieken creëren wat het erg moeilijk maakt om metabolieten te identificeren en te kwantificeren. Naast de lange acquisitietijden die niet optimaal zijn voor de kliniek tonen studies al aan dat klinische MRS niet gevoelig is voor diagnostisch gebruik.

7T MRI en MRS

Magnetic resonance imaging bij ultrahoog veld, 7 tesla en hoger, heeft de potentie evaluatie van therapie effectiviteit in de oncologie verbeteren. De toegenomen sterkte van het magnetische veld verbetert de SNR en contrast-ruisverhouding (CNR) van de MR-signalen en beelden vergeleken met klinische MRI en MRS. Het maakt het mogelijk beelden te acquireren met een hogere resolutie in een kortere tijd in vergelijking met klinische high-field MRI (3T), waardoor de discriminatie van de verschillende weefselsoorten ruimtelijk en contrastmatig verbetert. Bovendien maakt de verhoogde SNR en spectrale resolutie bij 7T discriminatie van individuele PME-metabolieten namelijk fosfocholine (PC) en fosfoethanolamine (PE), maar ook individuele PDE-metabolieten glycerophosphocholine (GPC) en glycerofosfoethanolamine (GPE), mogelijk. De verhoudingen van de individuele fosfolipidenmetabolieten (PC tot GPC, PE tot GPE) zijn ook gecorreleerd met tumorweefsel en worden al *in vivo* gebruikt als biomarker voor therapie-evaluatie in onderzoek. Naast het onderscheiden van extracellulaire en mitochondriale anorganische fosfaat (Pi), is het ook mogelijk om de pH van het weefsel te meten omdat de resonantiefrequentie van Pi verandert met de zuurtegraad van de omgeving.

Helaas is de vertaling van 7T MR-beeldvorming naar de kliniek nog steeds lastig vanwege meerdere uitdagingen op ultrahoog veld (≥7 tesla). Net als bij klinische MRI veroorzaken weefsels overgangen en anatomische bewegingen artefacten met toenemende complexiteit bij hogere veldsterktes. Het kan resulteren in signaalverlies en dus afname van de SNR, frequentieverschuivingen, verminderde spectrale resolutie als gevolg van lijnverbreding en meer. Bovendien is het gebruik van een reeks ^{1}H-dipoolantennes vereist om homogene zendvelden (B_1^+) te maken, omdat de RF-golflengte korter (≤11cm) is dan de afmetingen in het menselijk lichaam, i.e. de overgangen van verschillende weefsels, waardoor destructieve RF-interferenties worden gecreëerd.

De Larmor-frequentie van ^{31}P op 7T is echter vrijwel identiek aan de frequentie van ^{1}H op 3T, waardoor kansen ontstaan om welbekende 3 tesla RF-engineering te gebruiken voor toepassing in 7T ^{31}P MR-spectroscopie. Oppervlaktespoelen gebruiken bijvoorbeeld hoge energetische adiabatische RF-pulsen om een ruimtelijk homogene fliphoek verdeling te creëren en zijn gelimiteerd tot oppervlaktetoepassingen vanwege de specifieke absorptiesnelheid (SAR), een veiligheidsmaatregel voor de totale RF-energiedepositie in het menselijk lichaam tijdens acquisitie. Vooruitgangen in ^{1}H MRI bij 3T tonen al aan dat een “birdcage” spoel een homogeen B_1^+ -veld produceert dat het gebruik van blokpulsen toe staat om ruimtelijk homogene flip-hoek te bereiken, de totale SAR te verminderen en meer RF-pulsen per tijdseenheid mogelijk te maken met een extra verhoogde

homogeniteit over een groter veld. Om de SNR over grotere volumes te verbeteren, neemt het aantal Rx-spoelen toe tezamen met de dimensionaliteit van de data. Bovendien nemen de datasets door grotere volumes van interesse ook toe en zijn ze moeilijk te analyseren met huidige software, zeker werkende met research-hardware. Deze toename in complexiteit en bestandsgrote van de datasets vereist de ontwikkeling van nieuwe verwerkingsprogrammatuur.

Doel proefschrift

Het doel van dit proefschrift is het demonstreren van een variërend aantal tools voor het verbeteren van therapie evaluatie in oncologie gebruikmakende van kwantitatieve MR-beeldvorming en spectroscopie op ultrahoog veld.

De laatste jaren is een paradigmaverschuiving in therapie evaluaties voor oncologie duidelijk. Enkel focussen op de morfologische veranderingen met de verscheidenheid aan beeldvormingsmodaliteiten is niet voldoende om tumorprogressie of non-respons van geneesmiddelen vroeg tijdens de behandeling te beoordelen. Eerder meten of de behandeling aan slaat dan het huidige minimum van enkele maanden chemotherapie zou verandering van de therapie toe staan voordat tumorprogressie inzet of complicaties voor de patiënten merkbaar zijn. Een niet-invasieve methode die beschikbaar is met MR spectroscopische beeldvorming met ultrahoog veld kan daarom een noodzaak worden om de weg vrij te maken voor geïndividualiseerde geneeskunde.

In het eerste deel van dit proefschrift werden de veranderingen in relaxatietijden gekwantificeerd in *ex vivo* varkens recta tijdens fixatie van formaldehyde en in menselijke preparaten. Hoofdstuk 2 concludeert dat de T_1 relaxatietijd van de circulaire spier, mucosa en submucosa en de T_2 relaxatietijd van de circulaire spier afnemen. Als bijgevolg vermindert fixatie voorafgaand aan beeldvorming geleidelijk het beeldcontrast. Het menselijke preparaat werd daarom afgebeeld tijdens de eerste paar uren van fixatie, op zoek naar een geschikte diagnostische marker om tumordiscriminatie te evalueren. Echter, er is geen eenduidige parameter gevonden via traditionele MRI-technieken, noch T_1 noch T_2, die als een significante diagnostische parameter voor therapie-evaluatie gebruikt kan worden.

Wanneer MR spectroscopische beeldvorming wordt gebruikt als hulpmiddel om metabole veranderingen in behandelingen als potentiële biomarker te evalueren, moet het weefsel *in vivo* worden bestudeerd. De eerste stap om metabole beeldvorming bij patiënten te brengen, is zorgen voor een goede uniformiteit van het magneetveld (B_0). In hoofdstuk 3 wordt de verbetering van de B_0 veldhomogeniteit

in het lichaam onderzocht door het simuleren van een lokale reeks shim-spoelen op lever MR-beelden tijdens verschillende respiratoire toestanden. Vanuit simulaties is het duidelijk dat het verhoogd aantal vrijheidsgraden, beschikbaar met de lokale array van shim-spoelen de homogeniteit in grotere mate (10%) verbeteren dan enkel de standaard shim hardware. Het shimmen van B_0, afhankelijk van de verschillende ademtoestanden maakt een nog verdere verbeteringen van de B_0 homogeniteit mogelijk, variërend van 21 tot 44%, waardoor effecten van de ademhalingsbeweging worden gereduceerd. Dit belooft veel voor zowel MR-beeldvorming als MR-spectroscopie over het hele lichaam, vooral bij hogere veldsterktes, omdat het verkrijgen van homogeniteit complexer wordt met toenemende veldsterktes.

De volgende stap om metabole MRI te implementeren voor patiënten is het faciliteren van effectieve excitatie van ^{31}P-spins. Hoofdstuk 4 presenteert de integratie van een ^{31}P whole-body birdcage op 7 tesla, om ^{31}P MRS over grote “fields of view” (FOV) mogelijk te maken. Het ontwerp van de spoel maakt het gebruik van rechthoekige RF-pulsen mogelijk waardoor de algehele SAR verlaagt in vergelijking met adiabatische RF-pulsen, terwijl de homogeniteit van de flip-hoek behouden blijft zonder een verkleining van de MR bore diameter, de buis van het MR-systeem, en dus grotere patiënten of ontvangstspoelen toestaat. De spoel maakt uitwisseling mogelijk tussen de SNR voor een toename van de ruimtelijke resolutie en/ of MR-weging in ^{31}P MR spectroscopische beeldvorming door de flip-hoek of repetitietijd te wijzigen. Binnen de SAR-beperkingen kan het aantal RF-pulsen per tijdseenheid worden verhoogd, zoals wordt aangetoond door middel van snelle 3D chemische shift imaging (CSI) van de volledige lever met een korte TR en lage flip-hoek excitatie om optimale SNR per tijdseenheid te verkrijgen. Bovendien werd de T_2 van PCr in de gluteus maximus gekwantificeerd, met behulp van een multi-echo spectroscopisch beeldvormingsprotocol (MESING), iets dat voorheen niet mogelijk was in grote volumes in het lichaam omdat de energie depositie als gevolg van adiabatische refocusing pulsen te hoog is. Het meten van de fysiologie van weefsel biedt mogelijkheden om therapie evaluatie verder te verbeteren.

Correcte interpretatie van de bij deze experimenten verkregen data vereiste de ontwikkeling van een verwerkings- en analysetool, CSIgui zoals uitgelegd in hoofdstuk 5. De grote datasets hebben een hoge dimensionaliteit en worden daarom niet goed verwerkt door huidige softwareoplossingen op standaard MR-systemen of beschikbare MRS-analyseplatforms. De ontwikkelde tool is te gebruiken met standaard MRS bestandstypen zoals dicom en spar/sdat, maar kan ook ruwe databestanden inladen. Gegevens kunnen worden verwerkt met behulp van verschillende MR-algoritmen en worden opgeslagen voor verdere analyse met conventionele software om eenvoudige integratie met bestaande onderzoeken mogelijk te maken.

Het laatste deel, hoofdstuk 6, richt zich op de haalbaarheid van het verkrijgen van 3D CSI van tumorweefsel bij vier longcarcinoom patiënten met behulp van de ^{31}P whole-body birdcage spoel lichaam in combinatie met een dubbele Rx spoel of een Rx array bestaande uit 16 spoelen. Ten eerste bewezen simulaties dat het verlies in SNR per tijdseenheid met imperfecte fliphoeken minimaal is bij een korte TR lage flip-hoek excitatie, waardoor een tijdrovend kalibratieproces wordt geëlimineerd. De 3D ^{31}P-CSI werd met succes verkregen bij vier longcarcinoom patiënten met behulp van een van beide Rx opstellingen. Het gebruik van de Rx array verbeterde de SNR over een grotere FOV in vergelijking met de opstelling met een dubbele spoel. De verhoogde spectrale resolutie bij 7T maakte detectie van energie gerelateerde metabolieten zoals ATP en Pi mogelijk, maar ook de fosfolipide metabolieten inclusief de individuele PME, PE en PC, en PDE, GPC en GPE die niet detecteerbaar zijn bij 3T, vanwege de lagere spectrale resolutie. Daarom wordt geconcludeerd dat ^{31}P MRSI van longtumoren bij 7T haalbaar is en verder onderzoek rechtvaardigt om het potentieel als een niet-invasieve methode voor therapie evaluatie te beoordelen.

Conclusie

Dit proefschrift presenteert nieuwe strategieën om de respons van tumortherapie te evalueren en demonstreert meerdere hulpmiddelen om *in vivo* ^{31}P metabolische beeldvorming te verbeteren voor gebruik bij therapie evaluatie. ^{31}P MRS over grote volumes welke volledige organen zoals de lever, longen en spieren omvatten, is mogelijk met behulp van een ^{31}P whole-body birdcage spoel op 7 tesla. Dit maakt monitoren van weefselfysiologie tijdens de behandeling mogelijk om het begrip van tumorfysiologie en therapie-effecten te vergroten, maar ook metabole beeldvorming in het algemeen.

List of publications

Full papers

Feasibility of 31P spectroscopic imaging at 7 T in lung carcinoma patients

van Houtum Q, Mohamed Hoesein FAA, Verhoeff JJC, van Rossum PSN, van Lindert ASR, van der Velden TA, van der Kemp WJM, Klomp DWJ;
NMR Biomed. 2019; (November): e4204. doi:10.1002/nbm.4204

Low SAR 31P (multi-echo) spectroscopic imaging using an integrated whole-body transmit coil at 7T

van Houtum Q, Welting D, Gosselink WJM, Klomp DWJ, Arteaga de Castro CS, van der Kemp WJM;
NMR Biomed. 2019; (October):e4178. doi:10.1002/nbm.4178

Quantification of relaxation time changes during tissue-fixation and tumor biomarkers in *ex vivo* recta at 7T

van Houtum Q, Arteaga de Castro CS, Intven M, Hoendervangers S, Couwenberg AM, Verkooijen HM, Klomp DWJ, Philippens MEP;
PloS One, 2020 - submitted

B0 shimming simulations of the liver using a local array of shim coils in the presence of respiratory motion at 7 T

van den Wildenberg L, **van Houtum Q**, van der Kemp WJM, Arteaga de Castro CS, Bhogal A, Chang P, Nassirpour S, Klomp DWJ;
MRM, 2020 - submitted

Software Repository

CSIgui: an open-source view and processing tool for multi-dimensional MRSI data in MATLAB

Q. van Houtum. (2020, February 17). Sugocy/CSIgui: CSIgui v2.0 (Version vThesis). Zenodo. http://doi.org/10.5281/zenodo.3669640

Conference proceedings

Full coverage 31P MRSI of the liver with a body coil at 7T

van Houtum Q, Arteaga de Castro CS, Klomp DWJ, van der Kemp WJM

- Power pitch, digital poster at ISMRM 27th Annual Meeting, Canada, Montreal, May 2019 (**MAGNA CUM LAUDE** award)
- Oral presentation at the ISMRM Benelux Chapter, Netherlands, Leiden, January 2020

Feasibility of 7T 31P MRSI in lung tumors

Van Houtum Q, Arteaga de castro CS, van der Kemp WJM, Verhoeff JJC, van der Voort van Zyp JRN, Klomp DJW

- Digital poster at ISMRM 27th annual meeting, Canada, Montreal, May 2019

B0 shimming of the liver using a local array of shim coils in the presence of respiratory motion at 7T

van der Wildenberg L, **van Houtum Q**, van der Kemp WJM, Arteaga de Castro CS, Nassirpour S, Chang P, Klomp DWJ

- Oral presentation at ISMRM 27th annual meeting, Canada, Montreal, May 2019

B1 performance when excluding RF shields from transmit head coils to simplify multi nuclei and gradient insert setups

Welting D, Chavarria Marques I, Fantasia M, **van Houtum Q**, Steensma BR, Versteeg E, Wijnen JP, Klomp DWJ

- Digital poster at ISMRM 27th Annual Meeting, Canada, Montreal, May 2019

Necessity for detuning large volume coils?

Forner, R, Lunenburg M, **van Houtum Q**, Valkovič L, Ellis J, Rodgers CT, Klomp DWJ

- Digital poster at the ISMRM 27th annual meeting, Canada, Montreal, May 2019

Towards uncompromised merging of 1H and 31P receive arrays for multi nuclear metabolic imaging in the brain at 7T

Chavarria I, Welting D, Fantasia M, **van Houtum Q**, Wijnen JP, Klomp DWJ, Steensma BR

- Digital poster at the ISMRM 27th annual meeting, Canada, Montreal, May 2019

B1 performance when excluding RF shields from transmit head coils to simplify multi nuclei and gradient insert setups

Welting D, Chavarria Marques I, Fantasia M, **van Houtum Q**, Steensma BR, Versteeg E, Wijnen JP, Klomp DWJ

- Digital poster at the ISMRM 27th annual meeting, Canada, Montreal, May 2019

Large FOV phosphor MR spectroscopic imaging with multi-transmit proton MR imaging in the liver at 7 tesla

van Houtum Q, Welting D, Gosselink WJM, Rodgers CT, van der Kemp WJM, Klomp DWJ

- Oral presentation at the ISMRM 26th annual meeting, France, Paris, 2018
- Poster at the ISMRM Benelux Chapter, Belgium, Antwerp, January 2018

Low SAR body transmit facilitates 31P multi-echo spectroscopic imaging in the human body

van Houtum Q, van der Kemp WJM, Arteaga de Castro CS, Klomp DWJ,

- Poster at the MRS Workshop, Netherlands, Utrecht, October 2018

Concurrent use of 4 gradient axis enables eddy current compensation of an unshielded gradient insert coil

van der Velden TA, **van Houtum Q**, Boer VO, Luijten PR, Siero JCW, Klomp DWJ

- Digital poster at the ISMRM 25th annual meeting, USA, Honolulu, April 2017

Quantitative T1 and T2 measurements of pancreas at 7 tesla using a multi-transmit system

Damen M, **van Houtum Q**, van Leeuwen MS, Luijten PR, Webb AG, Klomp DWJ, Arteaga de Castro CS

- Poster at the ISMRM 25th annual meeting, USA, Honolulu, April 2017

Quantification of transverse relaxation time changes in rectal tissue during fixation at ultra-high field MRI

van Houtum Q, Klomp DWJ, Philippens MEP, Luijten PR

- Poster at the ISMRM 24th annual meeting, Singapore, May 2016
- Oral presentation at the ISMRM Benelux Chapter, Netherlands, Eindhoven, January 2016

High resolution imaging of ex vivo human pancreas specimen at high field MRI

van Houtum Q, Philippens MEP, van Leeuwen MS, Wessels F, Klomp DWJ

- Poster at the ISMRM 24th annual meeting, Singapore, May 2016

Quantification of transverse relaxation time changes in rectal tissue during fixation at ultra-high field MRI

van Houtum Q, Klomp DWJ, Philippens MEP, Luijten PR,

- Oral presentation at the ISMRM Benelux Chapter, Netherlands, Eindhoven, January 2016

Characterization of a breast gradient insert coil at 7 tesla with field cameras

van der Velden TA, **van Houtum Q**, Gosselink WJM, Luijten PR, Boer VO, Klomp, DWJ

- Digital poster at the ISMRM 24th annual meeting, Singapore, May 2016

Acknowledgements (Dankwoord)

Na al het schrijfwerk en heb ik nu eindelijk een kans om iedereen die me heeft geholpen in mijn promotie tijd, en met dit proefschrift, te bedanken. Ik heb een prachtige groep leergierige en lieve mensen leren kennen en mogen genieten van de bijzondere samenwerking. Zonder jullie inzichten, kennis en positivisme was dit een onmogelijke opgave geweest en heb ik daardoor met veel nieuwsgierigheid mijn promotie traject afgerond, daarvoor ben ik iedereen ontzettend dankbaar. Dan rest mij nog het bedanken van enkele mensen die me altijd bij zullen blijven.

Allereerst wil ik mijn co-promotor **Wybe** bedanken. Ik heb ontzettend veel van je geleerd tijdens onze late en lange scansessies waarbij we weer opzoek waren naar een hardware oplossing, of überhaupt signaal wilde zien, maar het was altijd gezellig en lachen. Je inzichten en kritische blik hebben me vaak de juiste richting in gestuurd en gemotiveerd, klinische ^{31}P MRSI komt eraan!

Dennis, begonnen als mijn co-promotor, ben ik nu toch trots dat je ook mijn promotor bent! Dankjewel voor de kansen de je me gegeven hebt. Je kennis, energie en kracht om het onderste uit de kan te halen zodat ik gemotiveerd bleef, ondanks de tegenslagen, hebben me ontzettend veel geleerd, wat ben je een unieke onderzoeker! Hobbyen op de woensdagvonden tot diep in de nacht ga ik dan ook zeker missen. Nu tijd voor ons om het werk in dit proefschrift naar de kliniek te brengen, ik ga je positivisme meenemen naar Amsterdam.

Dank ook aan mijn promotor **Peter**, wijze woorden dan onderzoek niet zonder vallen en opstaan gaat zullen me altijd bij blijven. U heeft een ontzettend gave onderzoek omgeving neergezet waar ik al die jaren van heb mogen leren en genieten.

Bij deze ook dank aan alle leden van de beoordelingscommissie**, prof. dr. ir. C.A.T. van den Berg, prof. dr. B. Oldenburg, prof. dr. ir. B.M.T. Burgering, prof. dr. A. Heerschap** en **dr. J.J. Prompers,** voor de tijd en moeite welke in het beoordelen van mijn proefschrift heeft gezeten.

Ik kan natuurlijk niet mijn ex-co-promotor vergeten, dankjewel **Catalina**. Jouw steun en motivatie maakte mijn pormotietraject veel gezelliger en ik kon altijd bij je terecht, voor hulp bij het scannen, knutselen van een RF coil, een goed gesprek en het nodige biertje. Veel succes met je nieuwe avontuur, zie je sowieso bij de volgende barbecue of karaoke!

Alle RF superhelden, **Dimitri**, **Mark**, **Ingmar**, **Aiden**, **Erik**, **Luca**, jullie zorgden ervoor dat ik zelf heerlijk kon klussen (lees recta snijden en epoxy knoeien) of maakten de gave hardware operationeel zodra ik ermee gespeeld had! Dank voor alle lange avonden van troubleshooting, borecoil swaps en reparaties.

Van diepzinnige Matlab discussies, bespreken van series of films, inbreken in eigen woning en het oprichten van een band die niet optreedt, **Deji**, dankjewel voor vier hele leuke jaren op het kantoor (en daarbuiten)! Ik kon al niet meer roddelen over je in het Nederlands, dus stiekem begrijp je dit ondertussen volledig. **Lennart**, **Anita**, **Kees** en **Edwin**, mijn promotietraject heeft altijd wat meer kleur gehad door jullie, de kantoormaatjes. Super bedankt voor gesprekken over elk nerdy onderwerp tot aan filosofisch geklets, research tips & tricks en natuurlijk de mooie zang momentjes in canon.

Hans en **Fredy**, dank, ook door jullie kon het scannen tenminste doorgaan en die spikes zijn verleden tijd! **Mariëlle**, ondanks dat je niet mijn co-promotor meer bent dankjewel de vele MR discussies, steun en het leren schrijven van artikelen. Dank aan alle coauteurs voor jullie klinische inzichten, mooie discussies en schrijfwerk. Het maakte het vormen van het grote plaatje een stuk leuker door ook op andere afdelingen rond te mogen kijken en onderzoeken.

Werken op het UMCU werd alleen maar leuker door de mensen die ik heb leren kennen. **Lieke**, dankjewel voor de gezellige manier van samenwerken, zoeken naar scan en programeer oplossingen en natuurlijk even stoom afblazen en gamen! Dat laatste zal zeker niet stoppen. **Carel**, naast de regelde game praat en momentjes konden we elkaar altijd even buiten vinden! **Tijl**, altijd in voor de ene laatste biertje om het af te leren. **Anja**, mede Whovian en ISMRM maatje, **Alex**, jij begrijpt het tenminste; there can only be one Q! **Sylvia,** dankjewel voor al je wijsheden rondom de administratie, je houd de groep scherp! Maar ook de rest van de Q2 gang, andere onderzoeksgroepen in zowel binnen en buiteland; **Martijn**, **Jeroen**, **Lara**, **Lisa**, **Jannie**, **Bart**, **Jaco**, **Marc**, **Alexander**, **Mariska**, **Vincent**, **Sophie**, **Jolanda**, **Erwin**, **Peter**, **Anneloes Arjan**, **Arjen**, **Ronald**, **Anna**, **Stefano**, **Janot**, **Oscar**, **Vitaly**, **Tine**, **Flavio**, **Alessandro**, **Natalia**, **Alberto**, **Wouter**, **Tim**, **Nikki**, **Jacob-Jan**, **Seb**, **Zhara**, **Ria** en **Frans**, dank jullie wel!

Bedankt ook aan alle vrijwilligers, patiënt of niet. Zonder jullie had ik geen scan kunnen maken, dank voor de tijd, energie en soms het afzien.

Mijn vrienden, o.a. de '"Pink Fluffy Unicorns" inclusief mijn opvangouders **Vera** en **Patrick** (jullie twee ontzettend bedankt voor de steun en hulp tijdens de laatste loodjes), **Laszlo**, **Wouter**, **Maaike**, **Ramon**, **Evelien**, **Linda**, **Quirine**, dank jullie wel voor alle fantastische tijden, blij dat ik jullie naast me stonden in dit avontuur. **Shibby** (Jorrit is het toch?), "steen, Fristi, hammer-time", de drie eenheid die ik altijd vast zal houden, dankjewel! Een verre vriend is meer waard dan een nabije buur, **Rudo**, **Anton** dank jullie beide voor de momentjes online of toch weer eens in real life! Als ik even wat perspectief nodig had (bier of wijn) en heerlijke klets staan jullie klaar voor me.

Britt, jij hebt altijd een luisterend oor voor me of even wat extra kaas om meer van het leven te genieten, dankjewel. Niets meer dan logisch dat jij mijn paranimf bent!

Tim, paranimf! UMCU collega van de andere afdeling, vanuit de Utrechtse Groenestraat (gele deur), het is altijd lachen met je tijdens het gamen of een gek filmpje.

Dankjewel papa (**Kees**) en mama (**Erna**), Ik ben jullie ontzettend dankbaar voor de onvoorwaardelijke steun en liefde, en niet te vergeten de bourgondische levensstijl in Berkel-Enschot. Ben blij dat er altijd een thuis voor me is in het zuiden, zonder jullie was het niet gelukt. **Nigel**, broertje, dankjewel voor je nuchtere humor van 5 euro. Je bezoekjes in Utrecht waren altijd gezellig en serieus wanneer nodig! Als laatste Oma (**Nelly**), ondanks de afwezigheid, altijd mijn inspiratie om door te gaan.

Curriculum Vitae

Quincy van Houtum was born on December 13th, 1988 in Tilburg, the Netherlands and grew up in the nearby village Berkel-Enschot with his parents Kees and Erna and younger brother Nigel. At the Odulphus lyceum in Tilburg his interest in physics, electric engineering, chemistry, and biology grew and after graduation he started the Biomedical Engineering bachelor at the Technical University Eindhoven. During this time, he explored his interest in biochemistry by working as a protein engineer at the faculty of Technical Chemistry for 2 years. After receiving his bachelor, he continued by enjoying the medical engineering master, also at the TU/e. During his master's degree he completed internships in Maastricht UMC focusing on simulation design for heart patients and fingerprint analysis for clinical evaluation. He then moved to Utrecht and designed, simulated, plus manufactured an MR insert gradient at the UMCU and wrote his master thesis at the same hospital on the integration of fluorescence confocal microscopy with MRI for real time imaging of targeted drug delivery. The latter involved animal experiments for which he passed his laboratory animal science exam. In 2015 he began his PhD research at the department of Radiology of the UMC Utrecht focusing mostly on body applications in MR imaging and spectroscopy for improvement of therapy assessment in oncology.

With the completion of this thesis in sight he started as a post-doctoral researcher at the Amsterdam University Medical Centre continuing his interest to bring MR spectroscopy at high field to the clinic.